Alma Mater Studiorum
Università degli studi di Bologna

Department of Electronics,
Computer Science, and Systems

Scuola di Dottorato in Bioingegneria - Ciclo XXIII
Settore scientifico disciplinare di afferenza: ING-INF/06

Methodological improvement of 3D fluoroscopic analysis for the robust quantification of 3D kinematics of human joints

presented by
Luca Tersi

Supervisor
Prof. Angelo Cappello

Co-supervisors
Rita Stagni, Ph.D.
Silvia Fantozzi, Ph.D.

Reviewers
Prof. Mario Cesarelli
Prof. Vasilios Baltzopoulos

Ph.D. Coordinator
Prof. Angelo Cappello

Year 2011, Final Exam

ABSTRACT

3D video-fluoroscopy is an accurate but cumbersome technique to estimate natural or prosthetic human joint kinematics. This dissertation proposes innovative methodologies to improve the 3D fluoroscopic analysis reliability and usability.

Being based on direct radiographic imaging of the joint, and avoiding soft tissue artefact that limits the accuracy of skin marker based techniques, the fluoroscopic analysis has a potential accuracy of the order of mm/deg or better. It can provide fundamental informations for clinical and methodological applications, but, notwithstanding the number of methodological protocols proposed in the literature, time consuming user interaction is exploited to obtain consistent results. The user-dependency prevented a reliable quantification of the actual accuracy and precision of the methods, and, consequently, slowed down the translation to the clinical practice. The objective of the present work was to speed up this process introducing methodological improvements in the analysis.

In the thesis, the fluoroscopic analysis was characterized in depth, in order to evaluate its pros and cons, and to provide reliable solutions to overcome its limitations. To this aim, an analytical approach was followed. The major sources of error were isolated with *in-silico* preliminary studies as: (*a*) geometric distortion and calibration errors, (*b*) 2D images and 3D models resolutions, (*c*) incorrect contour extraction, (*d*) bone model symmetries, (*e*) optimization algorithm limitations, (*f*) user errors. The effect of each criticality was quantified, and verified with an *in-vivo* preliminary study on the elbow joint. The dominant source of error was identified in the limited extent of the convergence domain for the local optimization algorithms, which forced the user to manually specify the starting pose for the estimating process. To solve this problem, two different approaches

were followed: to increase the optimal pose convergence basin, the local approach used sequential alignments of the 6 degrees of freedom in order of sensitivity, or a geometrical feature-based estimation of the initial conditions for the optimization; the global approach used an unsupervised memetic algorithm to optimally explore the search domain.

The performances of the technique were evaluated with a series of *in-silico* studies and validated *in-vitro* with a phantom based comparison with a radiostereometric gold-standard. The accuracy of the method is joint-dependent, and for the intact knee joint, the new unsupervised algorithm guaranteed a maximum error lower than 0.5 *mm* for in-plane translations, 10 *mm* for out-of-plane translation, and of 3 *deg* for rotations in a mono-planar setup; and lower than 0.5 *mm* for translations and 1 *deg* for rotations in a bi-planar setups. The bi-planar setup is best suited when accurate results are needed, such as for methodological research studies. The mono-planar analysis may be enough for clinical application when the analysis time and cost may be an issue.

A further reduction of the user interaction was obtained for prosthetic joints kinematics. A mixed region-growing and level-set segmentation method was proposed and halved the analysis time, delegating the computational burden to the machine. *In-silico* and *in-vivo* studies demonstrated that the reliability of the new semiautomatic method was comparable to a user defined manual gold-standard.

The improved fluoroscopic analysis was finally applied to a first *in-vivo* methodological study on the foot kinematics. Preliminary evaluations showed that the presented methodology represents a feasible gold-standard for the validation of skin marker based foot kinematics protocols.

KEYWORDS

Joint Kinematics
3D video-Fluoroscopy
2D-3D Registration
Robust Optimization
User Independence
Validation

ACRONYMS

3DF	3D video-fluoroscopy
ADM	Adaptive Distance Map
CT	Computer Tomography
DMR	Distance Map Resolution
DOF	Degree Of Freedom
DRR	Digitally Reconstructed Radiography
FOV	Field Of View
GA	Genetic Algorithm
ISB	International Society of Biomechanics
LMA	Levenberg-Marquardt minimization Algorithm
MA	Memetic Algorithm
MAD	Mean Absolute Deviation
MB-RSA	Model Based Roentgen Stereo-photogrammetric Analysis (RSA)
MRI	Magnetic Resonance Imaging
NURBS	Non Uniform Rational B-Splines
STA	Soft Tissue Artefact
RMSD	Root Mean Square Distance
RSA	Roentgen Stereo-photogrammetric Analysis
TKR	Total Knee Replacement
XRII	X-Ray Image Intensifier

CONTENTS

GENERAL INTRODUCTION

The reliable quantification of *in-vivo* physiological human joint kinematics is fundamental for essential orthopaedic clinical applications such as (*a*) the development of quantitative diagnostic tools [1], (*b*) the evaluation of surgery outcomes [2], or (*c*) the characterization of innovative prosthesis designs [3]. Moreover, from a biomechanical and methodological point of view, (*d*) the validation of non-invasive skin-marker based techniques [4] and (*e*) the soft-tissue artefact modeling [5] cannot be accomplished without a direct measurement of the bones or prosthesis components motion.

The discovery of X-ray production and detection technology, made by W.C. Roentgen in 1895 [6], opened the door to the development of innovative investigation techniques capable of visualizing the internal structures of the human body. The development of the X-ray image intensifier and of the television camera in the 1950s allowed the light produced by a fluorescent screen sensitive to the X-ray to be amplified, recorded and monitored. Being based on low X-ray dose, the new technique, known as *fluoroscopy*, was capable of the real time visualization not only of the internal body structures, but also of their motion. Fluoroscopy is currently applied in various clinical fields such as (*a*) in orthopaedic surgery, to guide fracture reduction and the placement of metalwork [7]; (*b*) in the angiography of leg, heart and cerebral vessels [8]; or (*c*) during the implantation of cardiac rhythm management devices [9].

The qualitative visualization provided by fluoroscopy, however, is not enough for the quantification of the motion. The step from a 2D qualitative imaging analysis to a 3D quantitative methodology needs a great interdisciplinary work which encompasses together knowledges proper of biomechanical, computer vi-

sion, mathematical and medical sciences. The first achievements arrived with the landmark-based radiostereometric analysis [10], and model-based methods have been proposed since the middle of the 1990s: the knowledge of the 3D shape of a non symmetric object and of one or two radiographic projections were claimed to be enough to estimate the position and the orientation of the object in the space, and thus to reconstruct the object kinematics [11]. In the following years different versions of the technique were developed and generically called *3D video-fluoroscopy (3DF)* [12]. A part from differences in the implementation of the alignment algorithm, The fluoroscopic methods are mainly divided into two categories: the mono-planar methods [12, 13], which investigate a big volume with a low X-ray dose, and the bi-planar methods [14], more accurate but invasive and expensive. Both mono-planar and bi-planar methods were initially applied to quantify the total knee replacement kinematics [15], but recent innovations led also to the study of intact joints [16].

The advantages of 3DF are manifold. The direct analysis of bones and prosthesis motion avoids the soft tissue artefact which limits the reliability of skin-marker based methods [4]. 3DF can theoretically achieve a millimeter/degree accuracy level [17] in joint motion analysis and modern fluoroscopes can work at a frame rate of $10 - 50$ fps. The dynamic performances are then sufficient to analyze the motion during activities of daily living, and simple joint-specific tasks that can be performed inside the fluoroscopic volume. The performance of 3DF were frequently exploited for research purposes, but several limitations prevented its use in the common clinical practice.

The alignment algorithms, in fact, is based on a cost function optimization. The optimization is negatively affected by local optima that are caused by the morphological symmetries of the investigated model, by cluttering of the contralateral limb, or by image blurring, which often interfere with the correct pose estimation [18]. Being prone to errors caused by the detection of false poses, a long time consuming user interaction is required to align the 3D model of the segment to the relevant fluoroscopic projections and to get as close as possible to the real pose. The manual alignment is followed by a 2D-3D registration algorithm aimed at the refinement of the results, but the outcome of the procedure remains strongly operator dependent [19].

Besides the technical limitations, it must be pointed out that the fluoroscopic examination implies an ionizing radiation dose for the patient [20]. Its invasiveness was reduced with the recent researches, but the dose may exceed the

normative limits when a bi-planar setup is used in combination with computer tomography (to get the 3D model of the joint). The risks correlated to any clinical investigation, must be justified by the outcome of the procedure. Physicians may be reluctant to adopt these radiologic methods even if 3DF can provide exclusive indications about the physiological and pathological behavior of the joints.

All together, the long user interaction, the computational burden, and the invasiveness, slowed down the translation of 3DF from the research to the clinic.

The goal of the current Ph.D. project is then to introduce methodological improvements in the 3D fluoroscopic analysis to make it more robust and reliable. To this aim, an analytical identification of the various sources of error was carried out, investigating solutions to improve the reliability of the results and to automate and speed up the data analysis.

The achievement of these objectives will lead to a more mature and user friendly technique, in which the user interaction is reduced and the cumbersome data analysis is delegated to the machine. A reliable mono-planar method will also halve the radiation dose for the patient fostering the use of the technique in the clinical practice. Moreover, finding out the limits and the possibilities of 3DF is a fundamental step necessary to define appropriate joint and pathology specific acquisition and elaboration protocols.

The Ph.D. activities were structured as follow: after an analysis of the state of the art for the quantification of human joint kinematics, preliminary analyses were carried out in order to find out the major limitations of 3DF; solutions were proposed to improve the analysis in term of accuracy and robustness and *in-silico* and *in-vitro* validation were carried out to quantify their performance; the technique was then applied as a gold-standard for a preliminary methodological validation study of stereophotogrammetric protocols for the quantification of foot kinematics. Finally, as a further automation improvement, a semi-automated prosthesis segmentation protocol was proposed and evaluated.

Thesis outline

Chapter 1 resumes the basic information of the state of the art about the methods for quantification of *in-vivo* joint kinematics, clarifying their pros and cons. Two radiographic methods are discussed: Roentgen Stereo-photogrammetric Analysis (RSA), which excels in accuracy, and 3D video-fluoroscopy which emerges as an

optimal compromise between accuracy and invasiveness. The technical issues correlated to the use of the techniques and details about the implementation of the 3D alignment algorithm are presented.

Three preliminary works are discussed in Chapter 2, and were meant to identify the points of strength and the potentially improvable limitations of the 3D fluoroscopic analysis. Two of these were *in-silico* evaluations carried out to investigate whether the image distortion correction and the calibration procedures were effective, and to evaluate the performances of the mono-planar analysis as compared to the bi-planar. The third study aimed at the evaluation of 3DF when dealing with *in-vivo* datasets. It was found out that the errors related to the bone morphology and symmetries cannot be avoided because intrinsic to the analyzed segment, but it must be quantified to characterize the joint-dependent performances of 3DF. It is possible, on the other hand, to improve quality and robustness of the optimization algorithm which is used to estimate the pose.

The 3DF versions proposed in the literature before the current Ph.D. activity used a local optimization algorithm. In Chapter 3, a sensitivity analysis was carried out to describe the convergence properties of the algorithm, and two solutions were proposed to enlarge the global optimum basin of attraction: the first consisted in the sequential alignment of the degrees of freedom in order of sensitivity, and the second consisted in estimating the pose optimization initial guess using simple geometrical features extracted from the fluoroscopic images.

A further improvement of the pose estimation algorithm robustness was introduced in Chapter 4. A hybrid memetic algorithm was designed merging together the improved local search developed in Chapter 3 and a global genetic algorithm. An *in-silico* evaluation was carried out in order to evaluate accuracy and precision of the new robust method, and it was demonstrated that the memetic algorithm can provide excellent results even without the supervision of the user.

The new algorithm was finally evaluated with the phantom based validation study described in Chapter 5. Due to the absence of non-invasive gold-standards, the *in-vivo* validation of 3DF is not feasible. On the other hand, the accurate marker based RSA could be used as an *in-vitro* gold-standard for the quantification of the kinematic of a knee phantom joint. Differently from the analysis of Chapter 2, the performance of the mono-planar and bi-planar 3DF were compared considering a real setup and thus including all the sources of error of the analysis. The study was carried out in collaboration with the Laboratory of Movement Analysis and Measurement (LMAM) of the Ecole Polytechnique Fédérale

de Lausanne, Switzerland (EPFL, Lausanne, Switzerland) and the acquisitions were made at the Centre Hospitalier Universitaire Vaudois (CHUV).

A further improvement towards the automation of 3DF was illustrated in Chapter 6. Many fluoroscopic methods rely on the contours extraction of the segment of interest in the fluoroscopic images. The procedure is typically carried out with a time consuming manual elaboration. If little can be done for the segmentation of intact joint bones, on the other hand the segmentation process can be automated for prosthesis analysis. In fact, even if 3DF was widely applied to prosthesis kinematics, it is still necessary to characterize the *in-vivo* behavior of new prosthesis design. A new semi-automated method for prosthesis segmentation in 3DF was proposed. The method was developed and validated in collaboration with the DEIS Bioimaging group of the University of Bologna.

Once validated, the improved method was finally applied to the *in-vivo* foot and ankle kinematics as described in Chapter 7. The great clinical interest of this joint is demonstrated by the number of stereophotogrammetric protocols recently proposed, which, like any marker-based protocol, are prone to accuracy limitations due to soft tissue artefact and to the deformability of the foot throughout the gait cycle. 3DF can accurately quantify the foot kinematics in physiological conditions, without limitations to range of motion and skin sliding, and could serve as a gold-standard for the validation of the stereophotogrammetric protocols. On the other hand, due to the small size and the symmetries of the involved bones, the hind-, mid- and fore-foot must be analyzed as compound segments. These segments, however, are intrinsically deformable, and the quantification of their accurate relative kinematics needs function-related models. A fluoroscopic gold-standard based on a functional-anatomical model for the assessment of marker-based foot protocols was proposed. Synchronous stereophotogrammetric and fluoroscopic acquisitions of foot kinematics were carried out, and the model was applied to quantify the gold-standard kinematics to validate the stereophotogrammetric foot protocol. This preliminary study was carried out in collaboration with the University of Padua (Italy).

All the analysis were carried out with the newly developed software called FluoroTrack described in appendix A. The software was designed to be a comprehensive framework for the complete 3DF analysis. The software included toolboxes for (*a*) 3D visualization, (*b*) image processing, (*c*) model and marker based mono- and bi-planar 2D-3D registration algorithms, (*d*) anatomical reference frame definition, (*e*) structured simulations and data analysis.

CHAPTER

ONE

OVERVIEW: 3D FLUOROSCOPY BASICS

1.1 Joint kinematics

Reliable knowledge of *in-vivo* joint kinematics, in physiological conditions, is fundamental for various clinical applications: (*a*) the study of prosthesis design must aim at the replication of intact joint biomechanical function [3, 21], (*b*) the development of quantitative diagnostic tools can help the detection of pathological alterations in motion [1], and (*c*) the outcomes of orthopaedic surgery must be quantified to find correlation with the recovery of physiological joint motor activities [2, 22]. Moreover, from a methodological point of view, accurate methods are necessary to validate and to evaluate errors associated with non-invasive techniques for the quantification of motion (i.e. inertial sensors, stereo-photogrammetry [5]).

For validation purposes, a gold-standard technique is needed to obtain accurate bone motion data directly avoiding Soft Tissue Artefact (STA). As testified by validation studies to test the protocols repeatability [23, 24, 25], and accuracy [26, 27, 28], STA is the major source of error for marker based protocols. STA leads to errors in joint translations and rotations of some centimeters and several degrees, respectively [4, 29, 30]. Moreover, segments such as the foot, the forearm, or the hand are composed by intrinsically deformable sub-segments. Skin marker based protocols treat these segments as rigid, introducing further errors in the kinematics estimation.

Cadaver studies can lead to accurate kinematics quantification [27, 31] but these kind of evaluation can hardly represent the clinically operative *in-vivo* conditions: furthermore, it is difficult to expand the approach for the evaluation of new protocols. When bone kinematics reconstructed using markers applied on the skin and on rigid plates were compared *in-vivo* with the one obtained from intra-cortical pins [26], it was not possible to acquire all the measurements simultaneously due to the limited dimension of the Field Of View (FOV). Thus, the results can be considered valid under a strict hypothesis of motor task repeatability, and even a simultaneous acquisition would underestimate STA, because pins limit skin motion. Moreover, although the use of intra-cortical pins allows one of the best accuracy, it cannot be adopted for human tests [26, 32, 33] for obvious ethical reasons, skin movement limitation and possible kinematics alteration. Less recently, using radiologic techniques that do not limit skin motion, STA was evaluated *in-vivo* in the foot, but the performed analysis was only 2D [28].

Radiostereometry or Roentgen Stereo-photogrammetric Analysis (RSA), designed for the quantification of prostheses components fixation [34, 35], was also used for *in-vivo* joint kinematics [36], but it is highly invasive as it is based on traditional X-rays and requires surgical intervention for radiopaque markers implantation. Finally, techniques based on computer axial tomography or magnetic resonance [37, 38, 39] have a small field of view, and a frame rate not sufficient for dynamic tests without combining data from a sequence of cyclic repetitions.

The best compromise among low invasiveness, high accuracy of dynamic analyses and flexibility was found by Banks et al. using a mono-planar fluoroscopic technique [12]. This technique was initially applied to prosthetic joints, exploiting the prosthetic implant radiopacity, that is highly contrasted even in fluoroscopy. Limiting X-rays exposure, it is possible to tune a trade-off between spatial and temporal resolutions of the analysis. This technique, denominated 3D videofluoroscopy (3DF), was extended later to intact joint, requiring Computer Tomography (CT) [40] or Magnetic Resonance Imaging (MRI) [41] scan of the bony segments for the estimation of bone surface geometry.

In the following sessions, the principal fluoroscopic methodologies for the quantification of human joint kinematics will be described and compared.

1.2 3D Fluoroscopy

To overcome the marker-based RSA practical limitations such as the surgical implantation of tantalum beads on the bone surface, or the use of double high X-ray dose radiologic projections (see Chapter 5), model based methods were proposed. The knowledge of 3D geometry of joint segments, and mono- or bi-planar projection views in fluoroscopic images, were claimed to be sufficient to reconstruct the absolute and relative 6 Degrees Of Freedom (DOFs) pose of bones or prostheses in the 3D space.

3D video-fluoroscopy (3DF) is a technique for the evaluation of joint kinematics based on the alignment of 3D models of bones or prostheses and series of 2D radiographic images representing the relevant mono-planar or bi-planar projections [42]. The joint kinematics is reconstructed estimating, independently for each video-frame, the 6 DOFs absolute pose (3 translations and 3 rotations) of each body segment, and then calculating the 6 DOFs of their relative pose.

3DF could provide reliable knowledge about joint kinematics, because it theoretically permits to achieve a millimeter/degree accuracy level in joint motion analysis [12, 43], with relatively high dynamic performances (up to more than 50 fps with modern fluoroscopes). These performances are sufficient to analyze the motion during activities of daily living, and simple joint-specific tasks that can be performed inside the fluoroscopic volume (1.1).

In-vivo knee tasks, such as squat, stair climbing, chair raising and sitting or step up-down, were widely analysed with 3DF in replaced [13, 15, 44, 45] and intact knee [40]. 3DF was also applied to quantify the *in-vivo* kinematics of ankle [46] and hip [47, 48] joints.

For the accuracy level and the possibility to acquire relatively fast dynamics, 3DF was used as a gold-standard in methodological studies for the validation and the evaluation of error associated with non invasive techniques for the quantification of motion. For the first time, acquiring simultaneously fluoroscopic and stereo-photogrammetric data, Stagni et al. [4] quantified soft tissue artefact at the thigh and shank without constraint to skin motion, and evaluated the error propagation to the resulting knee kinematics. Successively, these data allowed to analyze another source of error in stereo-photogrammetry such as anatomical landmarks mislocation [49] and to compare the performance of different STA compensation methods [50].

To estimate the 6 DOFs of a bone segment in a frame acquired by video-

fluoroscopy, a 3D model of the bone is virtually moved until it is best aligned to the relevant 2D image. This automatic procedure is typically carried out by means of an iterative optimization algorithms. Different metrics have been used to quantify a cost or a fitness function for the optimization such as: (*a*) the euclidean distance between the contour of the virtual projection of the model and the contour extracted from the fluoroscopic image [12, 51], (*b*) the root mean square distance between the projection lines and the model surface [3], (*c*) similarity measures between the fluoroscopic image and digitally reconstructed radiographies [52, 53, 54, 55, 56].

Promising accuracy levels have been reported for the intact knee joint: 0.23 *mm* for translation, 1.2 *deg* for rotation with bi-planar fluoroscopy [55]; and 0.42 *mm* for in-plane and 5.6 *mm* for out-of-plane translations, 1.3 *deg* for rotation for mono-planar fluoroscopy [17]. However, these accuracies cannot a-priori be considered valid and generalized for the other joints due to differences in the bone morphology and anatomy.

1.2.1 Technical and methodological issues

The performance of 3DF were frequently exploited for research purposes, but several limitations prevented its use in the common clinical practice.

The performance of 3DF, in fact, is affected by the geometry of the bone segments analyzed, and its accuracy could vary considerably because local minima, caused by symmetries of the models surfaces, or by occlusions, could severely interfere with a correct estimation of the pose. The alignment algorithms, in fact, is based on a cost function optimization. The optimization is negatively affected by the local optima that characterize the multivariate objective function. The local optima are caused by several factors:

- the investigated bones and prosthesis are often characterized by morphological cylindrical and spherical symmetries, and their projections may not be biunivocally related to their 3D poses;
- when analyzing cyclic tasks such as walking, it is common that the contralateral limb clutters the flurorescopic projection of the investigated limb;
- the moderate sensitivity of the phosphors to the X-rays imposes lower limits to the shutter speed of the acquisition system, which in turn often introduce image blurring (and contours smoothing) when acquiring limbs in motion.

Cluttering and blurring contribute in perturbing the informations needed to properly quantify the objective function for the optimization. Moreover, fluoroscopic images are geometrically distorted. If not properly compensated, the distortion may introduce errors in the calibration process and may deform the objective function. Methods for the image distortion correction are discussed in the next section.

Being prone to errors caused by the detection of false poses, a long time consuming user interaction is required to align the 3D model of the segment to the relevant fluoroscopic projections and to get as close as possible to the real pose. The 2D-3D registration algorithm become then a mere refinement of the results, but the outcome of the procedure remains strongly operator dependent.

To significantly improve the quality and the robustness of 3DF, it is then necessary to understand how the various sources of errors on affects the alignment algorithms and the final accuracy of the pose estimations. For this purpose, an analytic approach was adopted in order to find appropriate solutions to each single defect of the method.

Calibration and distortion correction

X-Ray Image Intensifier (XRII) systems are commonly used for digital planar image acquisition in radiology. However, even the best XRII system hardware cannot deliver images free of artefact. Lag, vignetting, veiling glare, geometrical distortions are introduced. A recent change in the fluoroscopic technology from XRII to flat panels, improved the quality of the acquired images, reducing the artefacts and increasing the sensitive to the X-rays, allowing thus the reduction of the intensity of the emitting radiations [20]. Due to the low cost, XRII is however still common in the clinics, and the artefacts must be taken in consideration to develop quantitative fluoroscopic techniques.

Lag Lag is the persistence of luminescence after X-ray stimulation has been terminated. Lag degrades the temporal resolution of the dynamic image. Traditional XRII tubes have lag times of approximately 1 *msec*. Therefore, lag in modern fluoroscopic systems is more likely caused by the closed-circuit television system than by the XRII.

Vignetting A fall-off in brightness at the periphery of an image is call vignetting. Vignetting is caused by the unequal collection of light at the center of

the XRII compared with light at its periphery. As a result, the centre of a XRII has better resolution, increased brightness, and less distortion.

Veiling glare Scattering of light and the defocusing of photoelectrons within the XRII are called veiling glare. Veiling glare degrades object contrast at the output phosphor of the XRII. As mentioned, the contrast ratio is a good measure of determining the veiling glare of an XRII. X-ray, electron, and light scatter all contribute to veiling glare.

Geometric distortion With ordinary sizes of the XRII, the images are affected by geometric distortion which causes a variation in magnification up to 5%-10% [57]. The geometric distortion has two main sources: the projection of the X-ray beam onto the curved input surface of the XRII and the deflection of the electrons inside the XRII caused by any external magnetic field. The former produces the typical "pincushion" distortion. The latter source may produce a sigmoidal distortion if the orientation of the XRII is parallel to the external magnetic field [58]. Larger XRII are more sensitive to the electromagnetic fields, causing a larger sigmoidal distortion.

Fluoroscope systems allow for the observation and analysis of biological structures, which could not be seen from outside in other ways. The images obtained with this instrument are geometrically distorted and unsuitable for a quantitative analysis, unless a careful correction procedure is performed. To characterize the geometric distortion of the specific XRII used, an image of a rectilinear calibration grid placed on the input screen of the XRII is commonly used. Analytical function are used to map distorted positions to undistorted positions. This is performed either locally for each quadrilateral or triangular patch [59] identified by four or three grid points respectively, or globally [60, 61]. Local techniques produce discontinuities from one patch to the other [62]. The global technique based on polynomials [60] avoids discontinuities and are more accurate than the local techniques, and were used in the present study.

The pixel spacing is also determined with this procedure, and through the acquisition of a second calibration device typically a 3D cage of Plexiglas with tantalum balls in known positions, the position of the X-ray source [63], and the eventual relative position of the second fluoroscope could be estimated minimizing the Euclidean distance between the projection of a model of the cage and the positions of the markers center in the distortion corrected fluoroscopic image.

Vignetting compensation A simple approach can be used to compensate for vignetting in fluoroscopic session. According to the Lambert-Beer law, in fact, at a first approximation, each pixel gray level is proportional to

$$I_{i,j} = I^0_{i,j} e^{-\int_\Omega \alpha_{i,j}(x)dx} \quad \text{with } i,j = 1,\ldots,1024 \tag{1.1}$$

Where I^0 is the intensity of the emitted X-ray, $\alpha(x)$ is an absorption coefficient, and the integral is along the extent Ω of the absorbing tissue the ray passed through. A gradient in I^0 is a disturbing factor, origin of the vignetting effect. On the other hand, in a fluoroscopic session, the fluoroscope parameters usually are not modified throughout the acquisition. It is then possible to acquire an empty image representing the intensity of the light field I^0. The light gradient can than be compensated computing the intensity of each pixel $G_{i,j}$ as:

$$G_{i,j} = \int_\Omega \alpha_{i,j}(x)dx = \ln\left(\frac{I^0_{i,j}}{I_{i,j}}\right) \quad \text{with } i,j = 1,\ldots,1024 \tag{1.2}$$

which is a quantity proportional to the density and to the thickness of tissue the emitted ray passed through.

Ionizing radiation dose

Besides the technical limitations, it must be pointed out that the fluoroscopic examination implies an ionizing radiation dose for the patient [64].

As for any radiological investigation technique, the risk correlated to radiation exposure must be taken into account to properly evaluate the trade off between the significance of the outcome of the procedure and its invasiveness. In Italy, the radiation exposure is regulated by the decree D.Lgs. 230/95 [65].

The biological effects of radiation is reflected by the dose equivalent, which is measured in sievert (Sv) by the SI. It is equivalent to the absorbed dose (measured in gray Gy) multiplied by a conversion factor which depends on the kind of radiation. The X-ray conversion factor is equal to 1. Another non SI unit of measurement to describe the dose is the roentgen (R) for which the following relation is valid: $1\ R = 0.12\ Sv$.

The annual dose was classified [66] as: low ($\leq 3\ mSv$), moderate (> 3 to $20\ mSv$), high (> 20 to $50\ mSv$), or very high ($> 50\ mSv$). For the health-care professionals the following limits have been fixed: maximum total dose of

100 mSv in five consecutive years, with a further limitation of a maximum of 50 mSv in one year. For the common people the limit was fixed at 1 mSv per year.

For the *in-vivo* acquisition described in Chapter 7, the fluoroscopic system Sirecon 40hd (Siemens) declared a dose of 4.8 μR per image. A total number 600 frames were acquired at 6 fps, corresponding to 3000 μR which are equivalent to 0.36 mSv, approximately one third of the annual limit. Moreover, this value correspond to the emitted dose while the skin absorbed dose would certainly be lower. On the other hand, increasing the acquisition frame rate and using a bi-planar setup, the ionizing dose for the patient will certainly increase, eventually reaching harmful limits if combined to other radiological based examination such as a CT to acquire the 3D model of the bones. To be on the side of safety for a possible clinical application, it is advisable to use MRI instead of CT and mono-planar fluoroscopic setup, but an interslice spacing of less than 1 mm is needed to assure a good resolution of the model.

1.3 Pose estimation algorithms

All the fluoroscopic methods for the quantification of joints kinematics estimate the pose of the investigated object for each of the acquired frames. The methods are mainly divided into two categories: the mono-planar methods, which investigate a big volume with a low X-ray dose, and the bi-planar methods, more accurate but invasive and expensive (Figure 1.1). Both mono-planar and bi-planar methods were initially applied to quantify the total knee replacement kinematics, but recent innovations led also to the study of intact joints.

In 3D joint kinematics with 3DF, the accurate knowledge of the geometry of the bony or prosthetic segments is necessary together with the relevant projection on the image plane. When a non-symmetric object is imaged by a nonorthogonal camera, a unique projection is produces for each 3D pose of the object. The pose estimation of the bone from a single view can be obtained by aligning the 3D object model in order to obtain a corresponding projection as observed in the X-ray image. A perspective projection model can represent the fluoroscope. In perspective projection model, a pinhole camera forms the image. X rays are considered straight lines emitted by a point source of uniform radiation in all directions (Figure 1.2). X-rays pass through the object damping their intensity according to the Lambert-Beer law (equation 1.1), and this process can be vir-

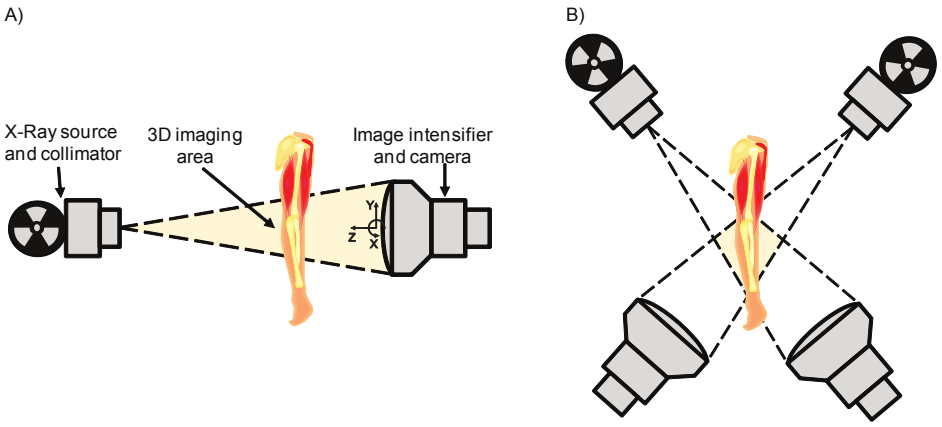

Figure 1.1: Configuration of a mono-planar (A) and bi-planar (B) fluoroscopic system. The bi-planar is more reliable but can investigate smaller volumes (in light red) with a higher X-ray dose for the subject.

tually simplified and replicated in order to estimate the pose that generated the real fluoroscopic image.

Mono-planar methods The first model based method in the literature was proposed by Banks and Hodge in 1996 [12]. An object recognition technique presented by Wallace and Wintz [67] formed the basis for the shape representation and matching components of the pose estimation process. Contour silhouettes were represented by normalized Fourier descriptors, where each contour was normalized for in-plane translation, in-plane rotation, and scale. The results indicated that knee rotations could be measured with an accuracy of approximately one degree and that sagittal plane translations could be measured with an accuracy of approximately 0.5 mm, but the technique was not reliable for the out-of-plane pose parameters. However this method could be applied only to prostheses, relied on the creation of a contour library of the object in different sampled poses, and had to interpolate the results for the inter-sample cases.

A similar approach was used by Hoff and Stiehl [43, 51] with different representations of silhouettes and alignment algorithm. Being based on the comparison of the areas of the prosthesis, these techniques had to extract closed curve contours, and this is not always possible in fluoroscopic images mainly due to cluttering.

Zuffi et al. [3] proposed a method to overcome the discussed limitations. The

technique, described in depth in Section 1.3.1 exploit the algorithm proposed by Lavallée and Szelinsky [11]. This algorithm is based on tangency condition between the model 3D surface and the projection rays that generated the external contours of the object in the image. Differently from the previous methods, this algorithm could work also with incomplete contours.

To reduce the user interaction, Mahfouz et al. [13] proposed a contour matching method that does not need manual identification of the external contours but exploit also the information of the internal part of the images. Informations related to spurious contours, however, interfere with a proper alignment reducing the convergence domain of the real pose.

Bi-planar methods To improve the accuracy of 3DF in the estimation of the out-of-plane pose parameters, different bi-planar methods were proposed.

Tashman and Anderst [68] used for the first time a bi-planar setup, but due to the high radiation dose, the method was test on a canine intact knee. The matching was carried out optimizing a similarity metric between a Digitally Reconstructed Radiography (DRR) and the relevant real projection. For the 3D model generation a CT acquisition was needed. The method was applied to the human knee in 2007 [2], and validate versus a RSA gold-standard with an invasive study during a running task. The declared accuracy was of $0.15 - 0.52$ mm and $0.34 - 1.27$ deg depending on the DOF.

Bingham and Li [69] proposed a new alignment algorithm called *connectivity method* which is a contour matching methods between the extracted contour in the image and the iteratively created virtual contour of the prosthesis. The declared accuracy is in the order of 0.2 mm/deg.

Another solution was proposed by Kaptein in 2003 [14]. Using reverse engineering 3D models of prostheses and contour matching methods in a phantom based validation study, a maximum standard deviation of the error in the migration calculation of 0.14 mm for translations 0.05 deg for rotation.

Even if bi-planar fluoroscopy is more robust and accurate, the present work focused on mono-planar fluoroscopy because it can investigate bigger volume with smaller X-ray dose for the patient. Moreover, mono-planar fluoroscopy represents the worst case scenario, more suitable to highlight and identify the pitfalls of the method and to optimize the pose estimation in terms of accuracy and precision.

In the present work, a modified version of the pose estimation algorithm

proposed by Lavallée and Szelinsky [11] and based on Adaptive Distance Maps (ADMs) was implemented. This algorithm was chosen because of its light computational weight and because it permits to achieve good accuracies even with incomplete contours [3], which can arise from occlusions or image blurring due to the bone motion.

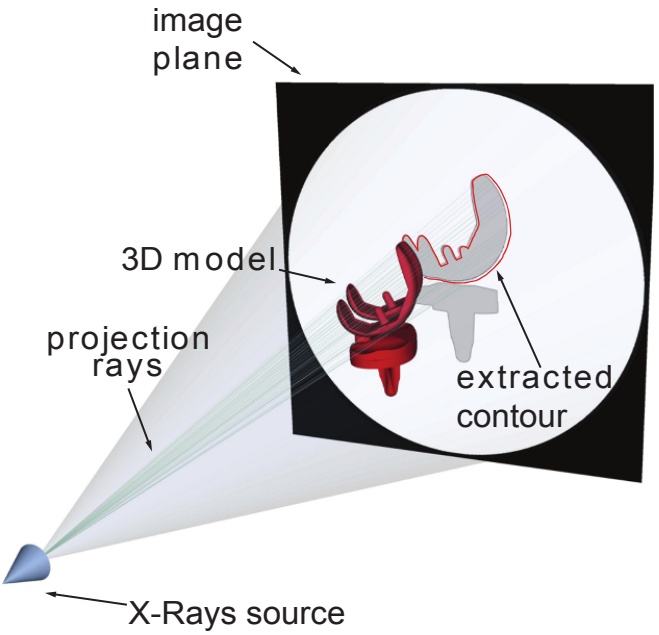

Figure 1.2: Virtual representation of a fluoroscopic system for the pose estimation with tangency condition

1.3.1 Implementation

An established technique was implemented to estimate the 3D pose of an object of known 3D geometry given its mono-planar fluoroscopic projection [3]. The algorithm was originally proposed by Lavallée and Szeliski [11] for bi-planar projection, and it is based on 3D ADM. In brief, (*a*) the fluoroscope is virtually modeled with a perspective projection model; (*b*) the 3D pose estimation is obtained with an iterative procedure that finds the best alignment between a bone surface model and its 2D fluoroscopic projection (typically a 1024x1024

DICOM[1] image). In the present study, the bone surface was modeled with triangles meshes, however different representation can be used (i.e. cloud of points, Non Uniform Rational B-Splines (NURBS)).

The quality of the alignment is represented by a cost function defined as:

$$RMSD(p) = \sqrt{\frac{1}{n}\sum_{i=1}^{n}[d(S_m(p), l_i)]^2} \tag{1.3}$$

RMSD is the root mean square distance between the surface $S_m(p)$ of the model m positioned in the pose $p = (T_x, T_y, T_z, \Theta_x, \Theta_y, \Theta_z)$ and n projection lines l. The projection lines l represent the X-rays that generated the edge points of the bone segment projection extracted by a Canny edge detector [70] in the fluoroscopic image and is expressed in parametric form:

$$l_i : C_i + \lambda \cdot \left(\frac{F - C_i}{L_i}\right), \quad \lambda \in [0, L_i] \tag{1.4}$$

Where $F = (Fx, Fy, Fz)$ is a point representing the X-ray source position (*focus*), $Ci = (Cix,\ Ciy,\ Ciz)$ is the $i-th$ of the n points of the contour, both expressed in the fluoroscopic system of reference, and L_i is their distance:

$$L_i = \|F - C_i\| \tag{1.5}$$

To quantify the Root Mean Square Distance (RMSD), l_i is sampled and, for each sampling point $P_k^i = l_i(\lambda_k)$, the distance from $S_m(p)$ is computed. The distance of the projection line from the surface is then defined as the minimum distance among those of the line sampling points.

$$d(S_m(p), l_i) = \min_k \left[d(S_m(p), P_k^i)\right] \tag{1.6}$$

The best alignment condition is finally identified finding the values of the pose p that minimize the $RMSD$ with an optimization algorithm.

$$RMSD_{min} = \min_p [RMSD(p)] \tag{1.7}$$

For a faster quantification of the distance $d(S_m(p), l_i)$ between the line and the

[1] DICOM: Digital Imaging and Communications in Medicine

model surface, and to define the sampling step of l_i, ADMs of the model surface is pre-computed and stored.

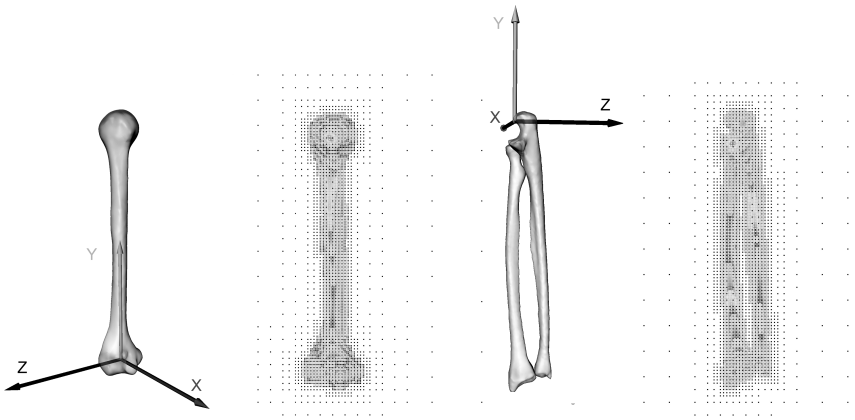

Figure 1.3: Adaptive Distance Maps (ADMs) of the elbow bones.

Briefly, the ADM is an octree-based representation of an object [71]. In this representation, the volume outside and inside the surface of the object is non-uniformly discretized. The map assigns to each point of the discretization the corresponding signed distance from the surface of the model: positive if outside, negative if inside the object.

The distance is computed as the minimum distance between the discretization point and the surface of model of the bone. The structure of the ADM is an octree which is built with an iterative procedure which subdivides a cube (also called octant) iteratively in other 8 half-side octants only if it contains at least one point of the mesh. The octree is then refined to avoid discontinuities between the levels of subdivision of two adjacent octants. The vertices of the octants are the volume discretization points. The distance of a generic point from the surface is then computed with a tri-linear interpolation of the distances of the 8 vertices of the smallest octant containing the point. The octant side dimension gets smaller closer to the surface, thus the interpolation error becomes negligible. In the present work, the resolution of the octree (smallest octant side) will be referred as Distance Map Resolution (DMR). For a further improvement of the algorithm speed, also the sampling step of the projection lines is adaptive. The sampling step varies accordingly to the local resolution of the ADM and gets

smaller closer to the surface. If s_k^i is the side of the smallest octant containing the sampled point P_k^i then the next point to evaluate the distance will be:

$$P_{k+1}^i = l_i(\lambda_{k+1}); \qquad \lambda_{k+1} = \lambda_k + \frac{s_k^i}{2} \tag{1.8}$$

Finally, l_i is resampled around the closest point to the surface with a uniform step length ten times smaller than DMR.

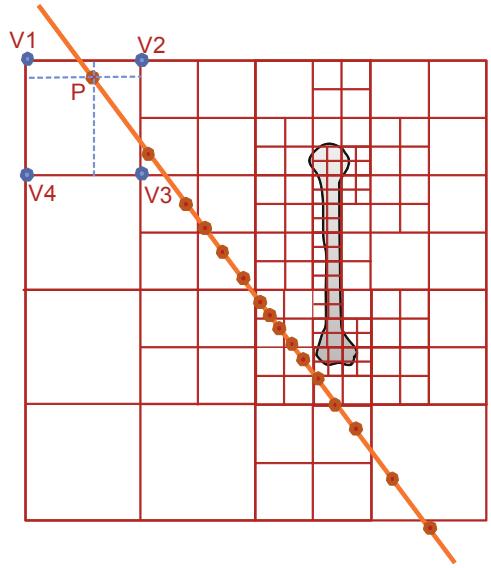

Figure 1.4: Scheme of the projection ray sub-sampling procedure. The octree is iteratively subdivided only if it contains at least one point of the model surface. The distance of a generic point P is the trilinear interpolation of the vertices (V) of the smallest octant containing that point. Information of the octant side is used for the adaptive sampling of the projection rays.

1.4 Conclusions

X-rays imaging methods proved to be valuable tools for the quantification of human joints kinematics, but, in order to find a good compromise among reliability, costs and invasiveness, much work can be done.

Even if bi-planar fluoroscopy is more robust and accurate, the present work focused on mono-planar fluoroscopy because, being less robust, it can better highlight the limitation of the fluoroscopic methods. A modified version of the pose estimation algorithm proposed by Lavallée and Szelinsky [11] was implemented. This algorithm was chosen because of its light computational weight and because it permits to achieve good accuracies even with incomplete contours [3]. Due to this characteristics, even if developed for prosthetic components, the algorithm can be applied also to natural joints.

The described 2D-3D registration algorithm will be investigated in depth in the following chapters. In particular different *in-silico* studies will characterize its performances under controlled conditions, in order to isolate and evaluate the effects of the various sources of error. Considerations will stem indicating the path to follow to improve the robustness and the quality of the measurements, and novel methods will be proposed to overcome the limitations of the current technique. The work will focus on the common aspects of the different 3DF methods such as the distortion correction, the optimization, and the segmentation. The worst case scenarios will be investigated, in order to highlight the limitations. The results will be generalizable to other alignment algorithms.

CHAPTER

TWO

PRELIMINARY ANALYSIS OF THE METHODOLOGICAL LIMITATIONS OF 3D FLUOROSCOPIC ANALYSIS

2.1 Introduction

In this chapter the preliminary analysis meant at the investigation of the main limitations related to the use of mono-planar 3D video-fluoroscopy (3DF) for the quantification of human intact and prosthetic joint kinematics will be discussed.

Part of the material described in this chapter was submitted to:

- **L. Tersi**, S. Fantozzi, R. Stagni, A. Cappello: In-vivo elbow kinematics using fluoroscopy: a feasibility study: Under review to *Computer Methods and Programs in Biomedicine*.
- **L. Tersi**, R. Stagni, P. Masini, S. Fantozzi, A. Cappello: 3D fluoroscopy to analyse elbow kinematics. Proceeding of *ESBME 2008*, Crete.
- **L.Tersi**, R. Stagni, S. Fantozzi, A. Cappello: Mono-planar vs Bi-planar 3D Fluoroscopy: in-silico Simulation of the Estimation of Total Knee Replacement kinematics. In: Proceedings *VPH 2010*, Brussels, Belgium, September 30 - October 1, 2010
- **L. Tersi**, R. Stagni, S. Fantozzi, A. Cappello: Total Knee Replacement kinematics: an in-silico reliability comparison between mono-planar and bi-planar 3D Fluoroscopy. In: Proceedings *XVII ESB Conference 2010*. Edinburgh, Scotland UK, 5-8 July 2010.
  This work was awarded with the *ESB Travel Award 2010*.

The accuracy of the measure depends on instrumental and environmental factors, such as (*a*) the number of projections considered, (*b*) the methodology to correct the geometrical distortions of the fluoroscopic images and (*c*) the calibration to establish the operating dimensions of the virtual fluoroscope, or (*d*) the geometry of the bony segments to be reconstructed. Moreover, the lack of a non-invasive gold-standard that can be applied *in-vivo* prevents the analysis of the influence of the various sources of error in optimal condition. Thus, in order to obtain a reliable estimation of the intact or prosthetic joint kinematics, computer simulations might help to isolate the various sources of error and to find proper specific solutions.

In order to find out to which extent the algorithm proposed by Lavallée [11] is suitable for mono-planar projection, an *in-silico* comparison between the mono-planar and bi-planar 3DF applied to knee prosthesis is proposed. Then the effect of the correction distortion and calibration were investigated with another *in-silico* study: using Digitally Reconstructed Radiographies (DRRs) obtained from upper limb CT models, we focused on how the geometric deformation of the fluoroscopic images modifies the estimate of the elbow kinematic. Finally, an *in-vivo* preliminary study on the elbow joint is proposed to test the performance of the method on real data.

2.2 Quantification of the performance reduction from bi-planar to mono-planar 3D Fluoroscopy

2.2.1 Introduction

A better knowledge of the kinematics behavior of Total Knee Replacement (TKR) during physiological activity still remains a crucial issue to validate innovative prosthesis designs and different surgical strategies. X-ray imaging tools for the accurate measurement of *in-vivo* kinematics of TKR components have been used to improve the clinical outcome of knee replacement [47]. The Roentgen Stereophotogrammetric Analysis (RSA) is currently considered as a gold-standard but invasive technique. It is based on bi-planar X-ray projections and on tantalum beads implants on prosthesis and bone surfaces. To avoid marker implantation, mono-planar fluoroscopic techniques [12] were proposed. Recently, Model Based RSA (MB-RSA) [72, 68, 69] were introduced to increase the technique reliability but with higher costs and invasiveness. The knowledge of the 3D geometry of the components and a mono-planar projection view in a fluoroscopic image were claimed to be sufficient to reconstruct the absolute and relative 6 Degrees Of Freedom (DOFs) pose of the components with a mm/deg accuracy level. However, it is still not clear how the reduction of information introduced by the mono-planar fluoroscopy can affect the accuracy and reliability of the technique. In this *in-silico* study we compared the mono- and bi- planar fluoroscopy, investigating the convergence properties and the sensitivity of the two methods.

2.2.2 Methods

The implemented alignment algorithm was based on 3D surface models and Adaptive Distance Maps (ADMs). Two orthogonal fluoroscopes were represented by perspective projection models (Figure 2.1). A global system of reference was defined with the x and y axis in the image plane of the frontal projection, and the z axis perpendicular to the image pointing towards the X-ray source, forming a right-hand reference frame. For the lateral projection, the out-of-plane axis was y. The pose was then estimated minimizing, with a Levenberg-Marquardt minimization Algorithm (LMA) [73], the Euclidean Root Mean Square Distance (RMSD) between a surface model and a beam of lines connecting the X-ray sources and the edge of the bone extracted in the projected images. A surface model of a

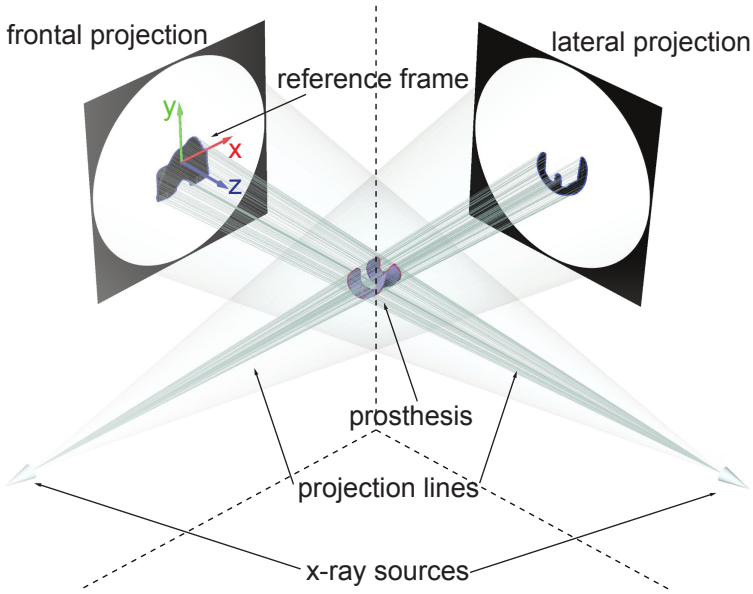

Figure 2.1: Outline of a bi-planar orthogonal setup.

femoral component of a TKR cruciate retaining prosthesis was placed in 4 reference poses and flat shaded projections were generated. The complete contours were extracted and then used for the alignment. The ADM had a resolution of 0.5 mm.

The RMSD with respect to each fluoroscope can be represented as a cusp. Its sensitivity to the variation of the DOFs was then quantified by the slope of the tangents around its minimum varying each DOF at a time with a step of 0.1 mm or deg (see Section 3.2.2 for details). Different minimizations were carried out varying the initial conditions in the domain around the projection pose. The initial deviation for translations (T) and rotations (Θ) were equal to -4 or 4 mm or deg, resulting in 256 permutations. Three conditions were analyzed: (a) double projection, (b) frontal projection, (c) lateral projections. The pose estimation errors were quantified and reported in terms of means and standard deviations.

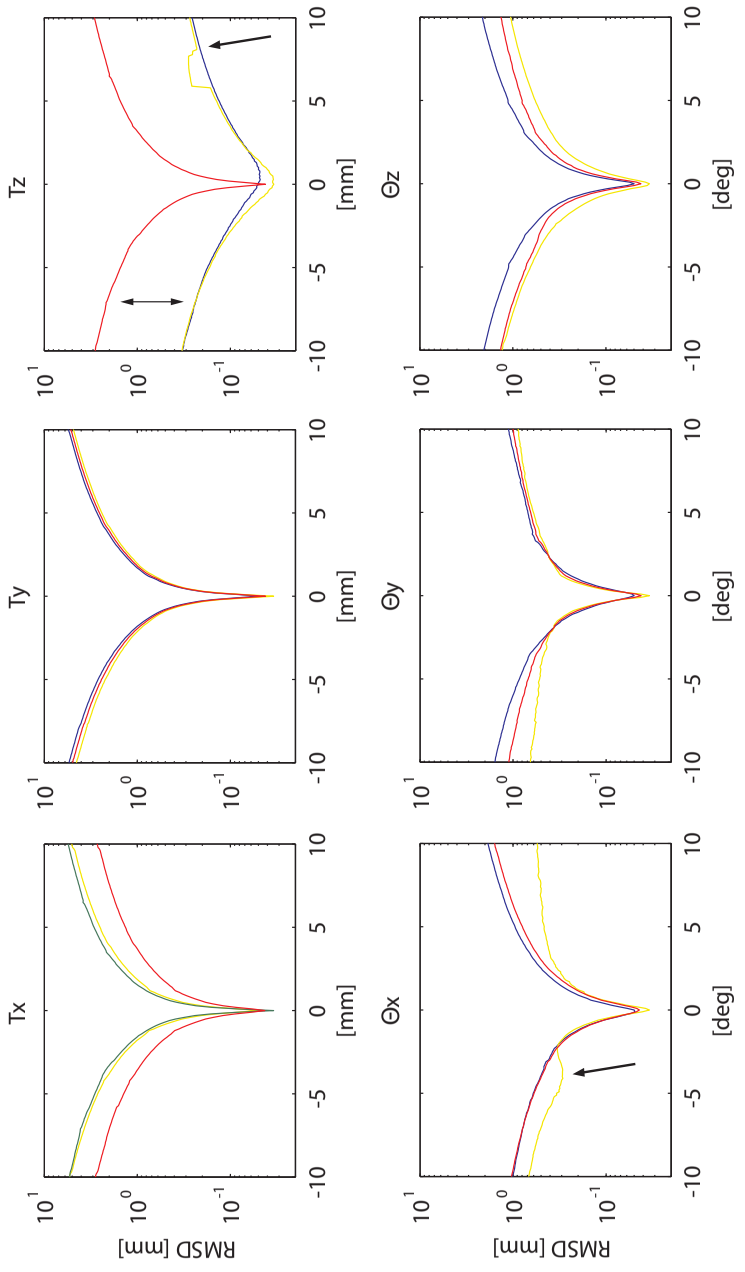

Figure 2.2: Comparison of the sensitivity curves for mono- and bi-planar alignments.

2.2.3 Results and discussion

The RMSD sensitivity (RMSD/DOF) was quantified as the slope of the sensitivity curves around their minima, see Figure 2.2. With the double projection the sensitivity was approximately of the same magnitude for all the translations (medium value $\simeq 0.34\ mm/mm$), and for all the rotations (medium value $\simeq 0.09\ mm/deg$). In the frontal and lateral projections, similar results were obtained for rotations, but the sensitivity is larger for the in-plane translations ($\simeq 0.54\ mm/mm$), and smaller for the out-of-plane translation ($\simeq 0.01\ mm/mm$). Local minima (highlighted by the arrow in figure 2.2) are evident for the lateral projection due to the convexities and the symmetries of the model in this projection (see also figure 2.3).

Table 2.1 reports the means and standard deviations of the pose estimations.

Table 2.1: Median and interquartile range of the estimation error.

DOF	bi-planar		frontal		lateral	
	m	iqr	m	iqr	m	iqr
$T_x[mm]$	0.07	$\simeq 0$	0.09	$\simeq 0$	0.10	$\simeq 0$
$T_y[mm]$	0.14	$\simeq 0$	0.07	$\simeq 0$	0.10	0.01
$T_z[mm]$	0.07	0.01	−1.19	$\simeq 0$	−2.42	0.14
$\Theta_x[deg]$	−0.01	0.02	−0.14	0.01	0.22	0.02
$\Theta_y[deg]$	−0.04	0.01	−0.03	0.01	−0.01	0.02
$\Theta_z[deg]$	0.04	0.01	−0.07	$\simeq 0$	−0.17	0.03

2.2.4 Conclusions

The bi-planar method could always provide errors at least one order of magnitude lower than the mono-planar methods. As confirmed by the sensitivity analysis, the bi-planar method can avoid the low out-of plane sensitivity of one projection relying only on the good information provided by the orthogonal one. As compared to the frontal projection, the larger dispersions of the errors obtained in the lateral can be explained by the larger number of convexity (Figure 2.3) in the extracted contours that can cause local minima in the cost function. A ro-

bust minimization algorithm could eventually avoid the minimization problems. The results confirmed the out-of-plane translation is a critical issue in 3DF, however error in the order of $1-2$ mm could still be acceptable depending on the application.

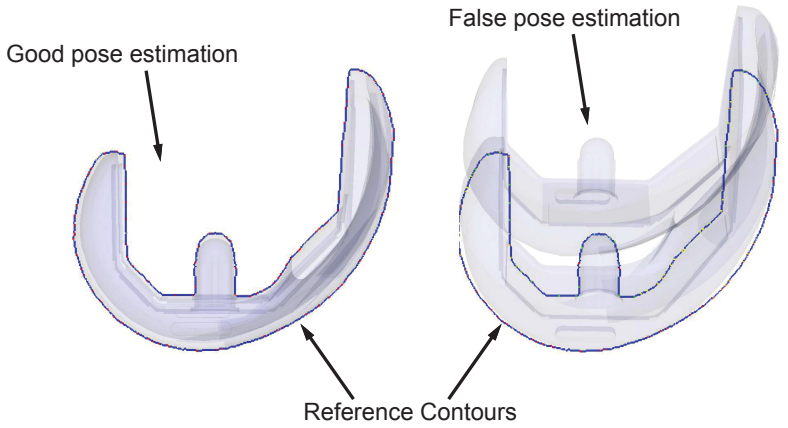

Figure 2.3: False pose estimation due to convexities: the alignment of only one condyle create a local minimum in the cost function.

2.3 *In-silico* evaluation of the distortion correction in 3DF

2.3.1 Introduction

One of the most evident source of error, that makes the step from qualitative to quantitative analysis complicated, is the presence of geometric distortion in the fluoroscopic images. Particular attention must be paid to the calibration of the system and to the correction of any geometric distortions introduced by the image formation chain (Section 2.3). Solutions were proposed to deal with the distortion correction and calibration issues [60], and computer aided simulations may help in investigating whether this technique is effective for our particular registration method.

The upper limb is particularly interesting for validation purposes. Recently 3DF has been applied to the shoulder [74, 75], and the elbow kinematics has been recently investigated with stereophotogrammetric protocols [30, 76]. The elbow plays a fundamental role in activities of daily living such as eating, drinking, cooking, personal hygiene, etc. Any alteration of its anatomical structures can compromise its function. An accurate knowledge of the *in-vivo* kinematics is necessary for the development of effective methods for joint surgical reconstruction and rehabilitation.

However, the 2D to 3D mono-planar fluoroscopy registration methods for the estimate of the 6 DOFs pose (3 translations and 3 angles) rely on surface model of the bone to be aligned and are particularly dependent on its spatial symmetries. Moreover, the elbow joint is composed by highly overlapping long cylindrical bones such as radius and humerus, and their alignment can suffer lack of accuracy and reproducibility. The effects of all the sources of error must be related to the final kinematic estimate, and the elbow is a joint that best highlight the problems for the *in-vivo* application of 3DF. Thus, a thorough validation study is needed to understand whether the proposed method can deal with the difficult alignment of the elbow.

The lack of a non-invasive gold-standard, with an accuracy lower than 1 *mm* for translations and 1 *deg* for rotations, on the other hand, can complicate *in-vivo* validation tests on humans. *In-silico* analysis are then needed for validation purposes. This study represents the first step towards the characterization of 3DF kinematic analysis of long bones such as the ones of the elbow joint with

computer assisted simulations. Using Computer Tomography (CT) models of the upper limb bones and constructing DRRs simulating flexion-extension kinematic we investigated (*a*) whether the algorithm proposed is suitable for the elbow kinematics in absence of significant sources of error, and (*b*) whether the geometric deformations introduced by X-Ray Image Intensifier (XRII) [60] compromise the final kinematics data.

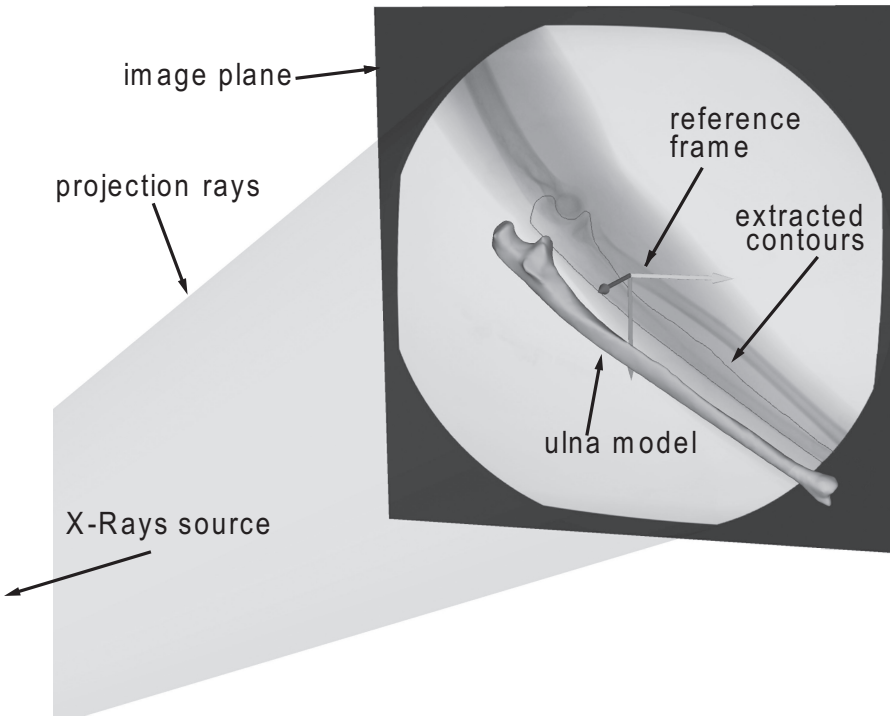

Figure 2.4: Image generation process: the X-Rays source generates the projection rays attenuated through the interaction with the bone, determining the image grey level. The tangency condition between the model and the projection rays generating the contours is used to estimate the bone pose.

2.3.2 Methods

High resolution bone models of ulna and radius (in the following analyzed together and referred as forearm) and humerus were downloaded from the official site of the European project VAKHUM (contract #IST-1999-10954, [77]). The anatomical reference frames were associated to the bone models according to International Society of Biomechanics (ISB) recommendations [78] but placed in the medium point between the humerus epicondile for both the segments. Distance maps with smallest octant side equal to 0.5 *mm* were computed. The same models were used for the construction of the DRRs

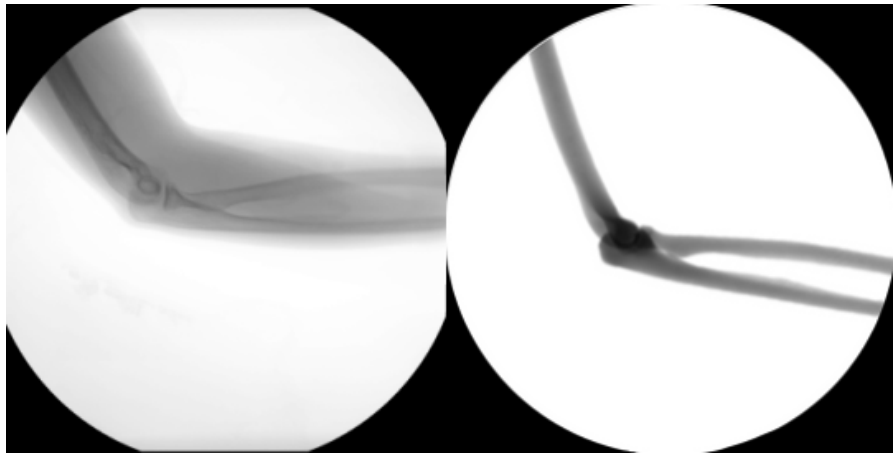

Figure 2.5: Comparison between real elbow fluoroscopic image (left panel) and the relevant Digitally Reconstructed Radiography (DRR) (right panel).

Other uniform maps with a resolution of 0.5 *mm* were computed in order to code the space inside and outside the model with boolean values. DRRs were represented by 1024x1024 pixel wide DICOM image with pixel spacing equal to 0.37 *mm*. The X-rays sources was virtually placed in the middle of the image at a distance of 1300 *mm*. Initially all the pixels were set to white. Then, the models were placed in known positions and orientations in the space. For each point inside the models, a projection ray from the camera was traced and the nearest 9 pixels to point of intersection in the image were attenuated according to the Lambert-Beer law 1.1. A low pass Gaussian filter was applied to smoothen the edges. Models of the calibration grid and cage were also created and the relative

DRRs created. A forearm flexion movement was simulated and 6 different images generated. The same images were then reprocessed to generate a second dataset considering also the simulation of geometric pincushion and sigmoidal distortion according to Fantozzi [61]. The images were then analyzed for the reconstruction of the two kinematics and the results were compared. Given the fact that the pixel spacing was estimated together with the correction of the distortion, analyzing the undistorted dataset, which do not need the correction, the pixel spacing was manually imposed to 0.37 mm.

Distortion Correction and Calibration

In order to obtain a reliable representation of the fluoroscope with a perspective projection model, geometric image distortion must be taken in consideration [61] and the position in the space of the camera must be identified with high accuracy. The geometric distortion has two main sources: (a) the "pincushion effect" caused by the projection of the x-ray beam onto the curved input surface of the XRII and (b) the deflection of the electrons inside the XRII caused by any external magnetic field producing the typical sigmoidal distortion. For image distortion correction a global warping techniques proposed by Gronenshild [60] based on a 5th degree polynomial function was used. A 2D model of a rectangular grid of tin-leaded alloy balls 5 mm apart was developed and the relevant distorted DRR was generated in order to calculate the parameters necessary for the correction. Positions of markers on the distorted image were detected. Transformations between detected and known positions of markers were then used to correct every generated DRR image. This automatic procedure leaded also to the estimation of the pixel spacing. Another DRR was generated projecting a model of the 3D calibration cage of plexiglas containing 18 tin-leaded alloy in known position typically used for the calibration. The position of the camera was then estimated minimizing the Euclidean distance between the projection of a model of the cage and the positions of the markers center in the distortion corrected fluoroscopic image with a Nelder-Mead minimization algorithm [79].

Pose estimation

After the geometric distortion correction, a Canny's edge detector [70] was applied to extract the bone contours. However, bones overlapping and pixel-wise noise caused the extraction of spurious contours which had to be detected and manually

erased by the operator. The method described in Section 1.3.1 was applied to the distorted and to the un-distorted datasets. The minimization was carried out by applying the LMA [73].

2.3.3 Results

Undistorted dataset The DRR of the calibration cage was generated and analyzed. The principal point position of the camera (projection of the pinhole camera to the image plane) was estimated with an error minor than 0.1 μm while the camera distance was estimated as 1299.15 mm. The poses of the forearm and of the humerus were estimated and the absolute residual deviations from the imposed kinematic were quantified. In Table 2.2 the mean (m), the standard deviation (std), the median (med) and the maximum (max) values over the six frames analyzed are reported.

Distorted dataset The pixel spacing estimated during the correction of the distortion was equal to 0.3708 mm. Analyzing the cage the camera principal point was estimated with an error minor than 0.1 μm while the camera distance was estimated at 1302.62 mm. Results are reported in Table 2.2.

2.3.4 Discussion and conclusions

Even if the number of alignments was limited, results showed that the error was normally distributed: the information of the mean and the median values were similar. Both the alignments of the forearm and of the humerus showed the same errors. Considering the resolution of the distance maps and the error related to the contour extraction as the only sources of error, an error of about 1 mm is made for the forearm translation in x and y direction. As showed in previous works [3] the more critical pose component in mono-planar 3DF is the translation along the projection axis z, because the contour extracted from the image is not so sensitive to displacement in this direction due to the high distance of the camera. Probably better results will be achieved placing the X-ray source closer to image plane, but further investigations are needed. Regarding the rotation angles, high accuracy was achieved for the flexion-extension angle due to high sensitivity associated to lateral view, while it is possible to observe an higher variability for the other two angles that seems to be coupled with the error made for the translation along the z-axis. Comparing the data of the

Table 2.2: Forearm and humerus residual pose deviation in terms of translation and rotation after the alignment for undistorted dataset, and after the correction of distorted images.

Forearm	**No Distortion**				**Geometric Distortion**			
	m	*std*	*med*	*max*	*m*	*std*	*med*	*max*
T_x $[mm]$	0.34	0.25	0.31	0.68	0.44	0.39	0.39	1.11
T_y $[mm]$	1.12	0.30	1.03	1.57	1.47	0.30	1.36	1.97
T_z $[mm]$	2.17	0.68	2.44	2.89	4.05	1.90	3.42	7.31
Θ_x $[deg]$	0.97	0.50	0.99	1.45	2.54	0.27	2.56	2.97
Θ_y $[deg]$	2.80	0.79	2.64	3.94	0.82	0.63	0.83	1.74
Θ_z $[deg]$	0.07	0.06	0.06	0.17	0.12	0.05	0.12	0.16

Humerus	**No Distortion**				**Geometric Distortion**			
	m	*std*	*med*	*max*	*m*	*std*	*med*	*max*
T_x $[mm]$	0.20	0.23	0.16	0.48	0.76	0.65	0.67	1.89
T_y $[mm]$	0.32	0.14	0.33	0.48	0.26	0.14	0.24	0.49
T_z $[mm]$	1.38	1.31	1.42	2.53	2.06	0.66	2.19	2.99
Θ_x $[deg]$	1.60	0.95	1.91	2.32	2.01	2.50	1.31	6.94
Θ_y $[deg]$	1.74	0.96	1.69	2.92	1.79	1.03	2.06	2.96
Θ_z $[deg]$	0.14	0.06	0.16	0.21	0.18	0.23	0.12	0.65

alignments with or without the distortion correction, the Gronenshild algorithm [60] resulted effective: there was no significant difference between the errors in the two groups of data. However, the maximum error related to the Θ_x angle for the humerus is about 7 degrees. This suggest that relative minima can compromise the non-linear minimization algorithm. Before characterizing the technique in *in-vitro* conditions, further study are needed to investigate how to reduce the error associated to z-axis translation and to analyze how the proposed method behave in the analysis of other motor tasks such as intra-extra rotation and at different degrees of abduction.

2.4 *In-vivo* elbow kinematics using fluoroscopy: a feasibility study

2.4.1 Introduction

Important clinical applications rely on the definition of joint physiological ranges of motion and on the detection of pathological alterations in motion. A reliable - accurate and precise - knowledge of the *in-vivo* kinematics is then necessary to analyse trauma outcomes, to develop effective methods for joint surgical reconstruction and to evaluate rehabilitation procedures. The elbow represents a joint of particular interest, because it plays a fundamental role in activities of daily living, and because, especially in athletes, it can be easily injured.

An accurate description of the elbow mobility was carried out in cadaver studies [31]. Veeger et al. [31] pointed out that the elbow can be modelled with two hinge joints: the humero-ulnar joint acts around the Flexion-extension (FL-EX) axis, while the proximal and distal radio-ulnar joints contribute together to a complex Prono-supination (PR-SU) movement. The consistency of this hypothesis was verified through *in-vivo* tests: Goto et al. [80] analysed sequences of static elbow positions and relevant contact areas by means of Magnetic Resonance Imaging (MRI). Nevertheless, a reliable knowledge of the *in-vivo* kinematics should refer to physiological conditions with muscles actively contributing to the motion. Attempts have been made using external marker/video based stereophotogrammetry [76], but the accuracy of this non-invasive technique is critically limited by soft tissue artefacts particularly for the upper limbs, with a loss of rotational motion of $20 - 48\%$ for the upper arm [4, 30]. Schmidt et al. [76] used a-priori knowledge about the elbow and wrist motion to compensate for soft tissue artefact and cross-talks. The a-priori knowledge implies the use of models and hypothesis on the motion to be estimated, but these assumptions might be inapplicable to pathological joints.

To overcome the accuracy limitations in the quantification of the kinematics of the knee joint, 3D video-fluoroscopy (3DF) was proposed [12, 43]. This technique was successfully applied to evaluate the motion in total knee replacements [15, 44, 45]. The assumed reliability [17, 81] of this technique led to its use also for the analysis of the kinematics of the intact knee joint [16, 40], and of other human joints, such as the hip [47], the ankle [46] and, more recently, the shoulder [75]. A recent study applied fluoroscopy to quantify how the elbow position

affects the distal radio-ulnar joint kinematics [82]. An accuracy of the order of 0.1 *mm* and 0.1 *deg* was declared, but quantified in a previous study on the knee [83]. The reliability of 3DF, however, is severely affected by (*a*) the geometric characteristics of the bony segments to be analysed, (*b*) the accuracy of the geometric model used for the alignment of each bony segment [84], (*c*) the accuracy and completeness of the contours segmented on the fluoroscopic image [85]. In particular, as demonstrated in preliminary *in-silico* evaluation studies [18, 86], the different morphology of the bones of the elbow, as compared to the knee, makes the alignment particularly complicated. Thus, due to the characteristics of the 3DF method, the reliability of the technique quantified for the knee joint [17] cannot be assumed as valid in general for the other joints. A new assessment of the fluoroscopic analysis performance must be carried out when investigating the kinematics of different bones and joints, which can differ from the knee for the dimensions, for the degree of overlapping areas and, especially, for geometrical peculiarities and symmetries.

To obtain reliable measurements of joint kinematics, standardized coordinate systems are necessary. Therefore, the ISB has recently proposed a set of joint coordinate systems to describe elbow kinematics [78]. Stereophotogrammetry, due to the interposition of soft tissue and to lack of palpable bony landmarks, is constrained to analyze the forearm as one segment, and then to decouple the motion using the double hinge model. 3DF, on the other hand, could allow to analyze the ulna and radius kinematics separately, although the partial longitudinal symmetry of these two bony segments could interfere with the correct alignment of the bone models with the projections. The use of one single anatomical reference frame for ulna and radius, considering thus the forearm as one single segment, may cause errors, when a motor task with a relative movement between the two bones (like PR-SU) is performed. Nevertheless, the geometry of radius and ulna makes the definition of two different anatomical reference frames difficult. As proposed by the ISB [78], this limitation could be overcome using, for the ulna and radius kinematics, technical reference frames defined using palpable landmarks of both the forearm bones (radial and ulnar styloids) and of the humerus (epicondyles). This procedure requires the elbow to be placed in a reference position, causing the reference frame to become position dependent.

The aims of this study were (*a*) to verify the applicability of 3DF for the reconstruction of *in-vivo* elbow kinematics, (*b*) to better support the ISB recommendations about the elbow motion description through the investigation of the

use of a single model for the forearm or of two different models for the ulna and radius while analysing *in-vivo* active motor tasks.

2.4.2 Material and methods

An established technique for 3D kinematic analysis of an object of known 3D geometry from a single view, described in Section 1.3.1, was implemented [11]. A perspective projection model represents the fluoroscope (Figure 2.4). 3D pose estimation is obtained with an iterative procedure that finds the best alignment between the bone model and its contour points extracted from 2D fluoroscopic image. The entity of the alignment is represented by a cost function defined as the RMSD between projection rays and the object. The best alignment condition is computed finding the minimum RMSD applying the LMA [73].

For a faster distance quantification between the rays and the model, a distance map was pre-computed and stored for each bony segment model. To increase the accuracy, differently from Zuffi et al. [3], the distance map was adaptive [11]. According to the finding of previous *in-silico* validation studies [86], and given the image pixel spacing of 0.34 $mm/pixel$, the resolution of the octree (smallest octant side) was chosen equal to 0.5 mm (Figure 1.3), which was found to be a good compromise between accuracy and computational weight.

The known problems of the convergence domain of the minimization algorithm [3] are enhanced by the symmetry of the bone models and the less contrasted contours, compared to total knee replacement analysis. Thus, the minimization process was guided towards the global minimum, trying to avoid local minima, performing 5 automatic kinematics estimations varying the initial poses for each frame as follows. Only for the first frame of the sequence, the initial pose was manually defined, in order to be as close as possible to the convergence point. For the other frames, the initial guess pose was taken as the final estimated pose of the previous frame, propagating the minimization forward from the first to the last frame. In the other four alignments, the starting rotation around the axis orthogonal to the image plane was acquired from the pose estimated in the previous alignment for the corresponding frame. The initial conditions of the other 5 DOFs, were alternately obtained propagating the pose forward (from the first to the last frame) or backward (from the last to the first frame). The final pose for each frame was considered the one, among the five estimated, with the lowest value of RMSD.

Table 2.3: Performed motor tasks.

Acronym	Tasks	
	FL-EX	*PR-SP*
FEzero	moving	neutral
FEpr	moving	pronated
FEsu	moving	supinated
PS90	90 deg	moving

A young Caucasian male living subject (180 cm, 72 kg, and age 30 years) signed an informed consent and participated to the study. A subject-specific model of his right elbow was developed from MRI data set (1.5T Gemsow scanner, GE Medical Systems, Milwaukee, Wisconsin). High resolution models were downloaded from the official site of the European project VAKHUM (contract #IST-1999-10954, [77]) and scaled to the measurements performed on the subject specific MRI dataset. The anatomical reference frames were associated to humerus, ulna, radius, and ulna/radius bone models according to ISB recommendations [78] (Figure 1.3). For the ulna/radius bone model, the radius and the ulna were considered fixed together in the acquisition pose.

Series of lateral images (1024x1024) were acquired at the frequency of 6 samples per second with a standard fluoroscope (Sirecon 40hd, Siemens) with the subject performing specific motor-tasks keeping the elbow within the fluoroscopic field of view. The subject performed 1 repetition of 4 motor tasks: (*a*) a pure active FL-EX at 0 deg PR-SU (FEzero), (*b*) a pure active FL-EX with pronated forearm (FEpr), (*c*) a pure active FL-EX with supinated forearm (FEsu), and (*d*) a pure active PR-SU with 90 deg of FL-EX (PS90).

For each frame, the four bone models were aligned with the corresponding contour: humerus, radius, ulna, and ulna/radius. Images of a 3D cage (Tilly Medical Products AB, Sweden) of Plexiglas with 18 tantalum balls in known positions and of a rectangular grid of tin-leaded alloy balls 5 *mm* apart were also acquired, in order to calculate, respectively, the position of the camera focus and the parameters for image distortion correction [63]. Distortion correction was performed using a global spatial warping technique [60]. A Canny edge detector [70] was applied to each fluoroscopic image to extract the outer contours of the bony segments. Spurious contours were manually erased by the operator. The

pose of the bony segments was estimated using the previously described model alignment method, using, for the forearm, ulna, radius and ulna/radius models.

Finally, relative motion of the aligned bony segment models was computed using the Grood and Suntay [87] convention.

Differences in the elbow kinematics, estimated using ulna/radius, ulna, and radius models, were quantified in terms of RMSD between the beam of projections rays and the surface of the bone models, being the minimization cost function. Maximum, median and minimum values of the RMSD were calculated for each motor task.

2.4.3 Results

Considerable differences were found in the alignments of the different bony segments. The humerus resulted to be the model with the smallest final RMSD. In all situations its residual RMSD was lower than 1.0 mm. Both the radius and the ulna, analysed separately, showed a median RMSD lower than 1.0 mm, the ulna showing larger maximum, up to 2.2 mm during FL-EX task at 0 deg of PR-SU (FEzero). Using the ulna/radius model the median RMSD increased up to 2.1 mm, with maximum up to 3.7 mm.

The RMSD of the humerus, ulna and radius models did not change significantly in the 4 motor tasks, while the ulna/radius model exhibited relevant changes in the RMSD depending on the motor task analysed, with the smallest values during FEzero and PR-SU task with 90 deg of FL-EX (PS90). For each model and task, the RMSD of the model from the projection rays is reported in Figure 2.6.

During all the motor tasks the ulna kept a physiological supination (as acquired in the reference position) of 80 deg (74 deg – 86 deg) (Figure 2.7), while the radius showed physiological PR-SU. The ulna-radius, instead, leaned towards following alternatively or the pose estimated for the ulna or that of the radius.

The RMSD is high when the ulna/radius bone should be supinated or pronated but decreased to a minimum comparable to other models when approaching the model acquisition pose. This effect is particularly evident while analyzing RMSD vs. PR-SU (Figure 2.8).

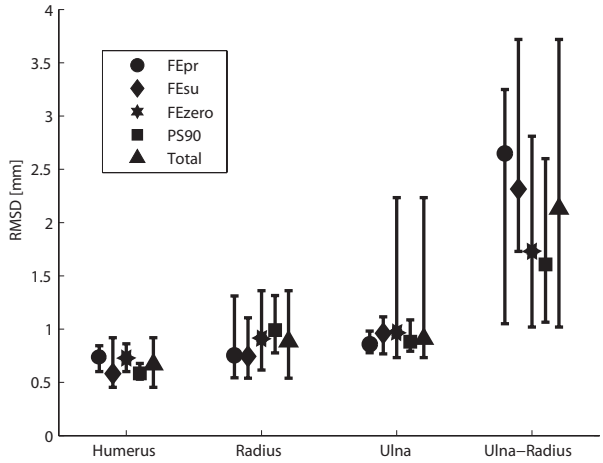

Figure 2.6: Median, maximum and minimum values of the RMSD for the humerus, radius, ulna, and ulna/radius models, in FEpr, FEsu, FEzero, PS90, and total motor tasks.

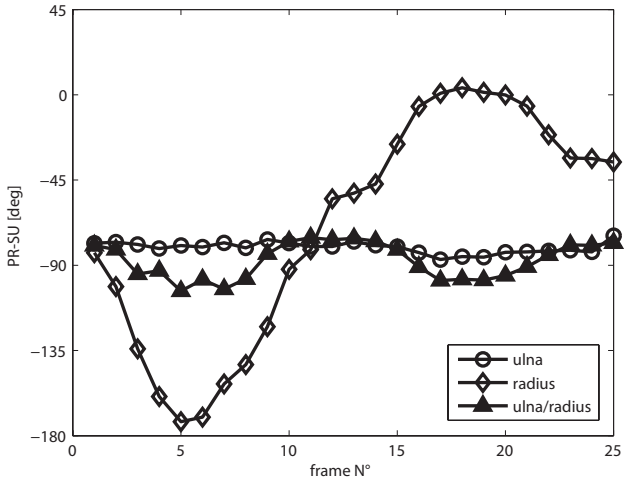

Figure 2.7: PR-SU estimated for the ulna (circle), radius (diamond) and ulna/radius (triangle) models during PS90.

2.4.4 Discussion

3DF was proposed to accurately quantify 3D kinematics of human joints [3, 12, 43]. Initially adopted and evaluated for the analysis of knee prosthetic devices [15, 44, 45], it could be an accurate method to quantify the 3D kinematics of intact joints [40, 75]. Nevertheless, due the dependence of the performance of 3DF on the specific geometric and experimental characteristics of the analysis, the applicability of the method to different joints must be verified. The aim of the present study was to investigate the use of 3DF for the analysis of elbow kinematics, evaluating the influence of different bone models.

The quantification of the RMSD of the model surface from the projection rays (Figure 2.6), pointed out the worse performance of the ulna-radius model with respect to single ulna and radius models, that showed results comparable to the humerus. The single bone models showed similar median RMSD values. Only the maximum RMSD of the ulna during FEzero differed, but this was attributed to a lower quality of the acquired fluoroscopic images which resulted in a worse segmentation of the bones. The image low quality was due to the extremely low X-Ray dose (0.48 μR) used during the acquisition which caused the sleeve to be visible on the arm projections. The RMSD of the ulna/radius model resulted much larger than single bone models. The FEzero and PS90 motor tasks showed the smallest RMSD for the ulna/radius models. This can be explained considering that during these motor tasks the forearm is in PR-SU condition closer to the model acquisition pose, while, during FEpr and FEsu, the forearm is pronated or supinated, respectively, with respect to the ulna/radius definition pose.

The better performance of single bone models was also highlighted by the more physiological PR-SU quantified for the ulna and radius models, compared to the ulna/radius model. The PR-SU of the ulna resulted fixed at about 80 *deg* supination (model reference condition), with a variability of about 10 *deg*, probably due to the non-perfect alignment of the ulna longitudinal axis with the PR-SU axis. On the other hand, the radius model resulted in an actual PR-SU of the radius during PS90, a pronated pose of the radius during FEpr, and a supinated pose of the radius during FEsu. In contrast, the ulna/radius model resulted in a severe underestimation of the PR-SU motion (Figure 2.7).

Finally, the inadequacy of the ulna/radius model to describe the kinematics of the forearm resulted particularly evident from the parabolic trend of its RMSD with respect to the PR-SU angle. This representation pointed out how important

the correspondence of the model to the actual relative pose of the ulna and radius is, in order to obtain a proper alignment.

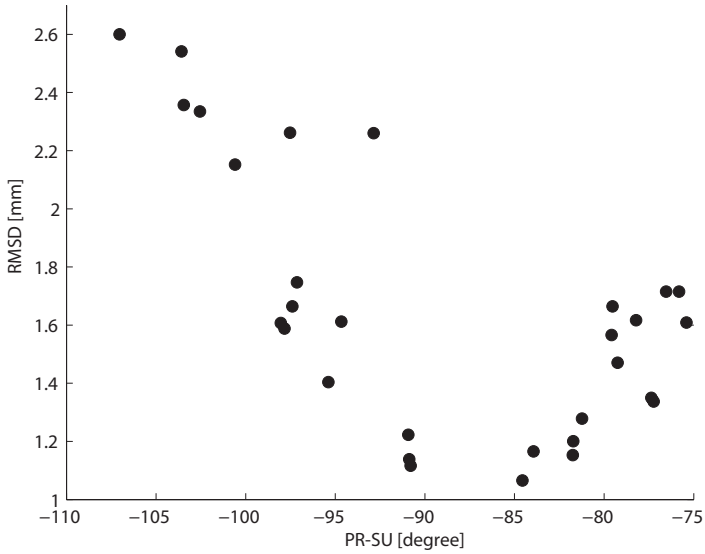

Figure 2.8: RMSD vs. PR-SU angle of the ulna/radius model during PS90.

2.4.5 Conclusions

In conclusion, 3DF resulted applicable to the analysis of the kinematics of the elbow due to the physiological results obtained for the analysed motor tasks, confirming the findings of Fu et al. [82]. The applicability is conditioned by the use of single bone models for the ulna and radius, rather than an ulna/radius model for the forearm, particularly when PR-SU movements are analysed. Future developments require a more precise quantification of the performance of the method, necessarily involving the comparison with a gold-standard kinematics computed with the RSA which involve double orthogonal projections and the implant of tantalum beads. RSA was reported to have an accuracy lower than 0.1 mm [88, 89, 90]. This analysis will investigate in particular the convergence domain in PR-SU, because the partial longitudinal symmetry of the radius, in particular, could result in a critical quantification of this DOF.

2.5 Preliminary conclusions

The preliminary analyses were a valuable tool to identify the problems and the potentiality of 3DF.

In-silico simulations of the alignment of knee prosthesis components highlighted that the mono-planar setup might be enough for the clinical and methodological application where no important information is related to the quantification of the translation along the projection axis. Moreover, it was pointed out that the presence of convexities in the investigated model (such as for the lateral view of the femoral component of a TKR, see figure 2.3) is a critical factor for the analysis. This result goes in favor of the methods that consider only the outer contours for the alignments [3, 12]. Adding informations using the internal contours [13] does not increase the convergence rate but rather introduces local optima in the objective function.

In-silico tests on long bones confirmed that the distortion correction and the calibration process are effective. The test allowed the definition of an operative advice regarding the distance of the X-ray source from the image plane. Keeping the source far from the image plane makes the projection rays more parallel to each other, contributing in reducing the sensitivity of the algorithm to translations along the projection axis. In a real acquisition session, it is then important to keep the X-ray source as close as possible to the image plane, compatibly with the dimension of the necessary volume.

Finally, the *in-vivo* evaluation demonstrated that the correspondence between the model and the real segment morphology is essential to get reliable kinematics quantification. Moreover, the attempt to automatically align the models with the local LMA, starting from the pose estimated on the previous or following frame, was not completely successful. This meant that the basin of attraction of the optimal pose was not sufficiently large to include the previous or following frame pose. This appeared to be the dominant source of error for 3DF, and if the error related to the symmetries of the investigated models must be quantified for validation purposes but cannot be eliminated because intrinsic of the method, on the other hand it is possible to improve the robustness of the optimization algorithm. Chapters 3 and 4 delved deeply into the optimization problem, proposing improving solutions both from a local and a global points of view.

CHAPTER

THREE

IN-SILICO CHARACTERIZATION OF THE ALIGNMENT METHODOLOGY

3.1 Introduction

As highlighted in Chapter 2, the performance of 3D video-fluoroscopy (3DF) is affected by the geometry of the bone segments analyzed, and its accuracy could vary considerably because local minima, caused by symmetries of the models surfaces, or by occlusions, could severely interfere with a correct estimation of the pose. Therefore, the technique is highly dependent on the initial guess of the pose for the optimization which is typically specified manually. However, the extent to which the intervention of the operator can affect the final reliability of the pose estimation has not been clarified yet. 3DF might currently still be operator-dependent [51] and the application of 3DF is still too cumbersome to be suitable for routine clinical practice. The high potential of the method cannot be exploited without a concrete automation of the procedure, involving

The content of this chapter was published to:

- **L. Tersi**, S. Fantozzi, R. Stagni: 3D elbow kinematics with mono-planar fluoroscopy: in-silico evaluation: *EURASIP Journal on Advances in Signal Processing.* 2010. (10.1155/2010/142989).

an automatic estimation of the initial guess of the pose. Therefore, the convergence domain of the optimization must be characterized in detail, exploring how different algorithms behave around reference poses.

A part from the preliminary study described in section 2.4, no fluoroscopic methods have been currently applied to the *in-vivo* kinematics of the elbow joint. This joint has, however, been characterized ex-vivo [31], with Roentgen Stereo-photogrammetric Analysis (RSA) [91, 92], and electromagnetic tracking systems [93], as well as *in-vivo* with non-invasive technique such as infrared stereo-photogrammetry [76], or Magnetic Resonance Imaging (MRI) [80]. Infrared stereo-photogrammetry, however, suffers accuracy limits due to soft tissue artifacts ($20 - 48\%$ of loss of rotational motion of the upper arm [4, 30]), while MRI fails to detect the effect of the active contribution of muscles to the motion. Even though fluoroscopy has not yet been applied to the elbow, this joint is of particular interest for its validation because it is characterized by (a) a high degree of bone superimposition, (b) being composed by thin long bones (in contrast with the typical morphology of knee prosthesis), and (c) marked longitudinal cylindrical symmetries (especially for the radius) . These aspects make the fluoroscopic analysis of the intact elbow considerably difficult, thus particularly suitable for a validation study.

The present study continues the analytical approach begun in Chapter 2. We hereby analyzed, by means of computer simulation, the convergence properties of a modified version of the pose estimation algorithm proposed by Lavallée and Szelinsky [11] and based on Adaptive Distance Maps (ADMs), in order to better understand the influence of local minima and to optimize the pose estimation in terms of accuracy and precision.

In this evaluation study we considered (a) the geometric characteristic of the bone models, (b) the resolution of the fluoroscopic projections, and (c) the resolution of ADM as the only sources of errors. Confounding effects caused by the geometric distortions, by errors in the calibration of the fluoroscopic models, or by the incompleteness of the bone contours were disregarded in the present study. The aim of the present study was to investigate the suitability of 3DF for the analysis of long bones kinematics, through a detailed exploration of the convergence domain of the minimization algorithm, in order to quantify and optimize measurement accuracy in terms of bias and precision.

3.2 Methods

3.2.1 Pose estimation algorithm

An established technique was implemented to estimate the 3D pose of an object of known 3D geometry given its mono-planar fluoroscopic projection [3]. The algorithm was originally proposed by Lavallée and Szeliski [11] for bi-planar projection, and is based on 3D ADMs. The modified version is described in 1.3.1. In brief, the (a) fluoroscope is virtually modeled with a perspective projection model; (b) the 3D pose estimation is obtained with an iterative procedure that finds the best alignment between a bone surface model and its 2D fluoroscopic projection (typically a $1024x1024$ DICOM image).

In the present study, the bone surface was modeled with triangles meshes, however different representation can be used (i.e. cloud of points, Non Uniform Rational B-Splines (NURBS)). The resolution of the meshes was not relevant, because the images for the alignment were generated *in-silico* projecting exactly the same models. There was, thus, a perfect correspondence between the 3D model and the projection independently from the meshes properties. The quality of the alignment is represented by a cost function defined in 1.3.

The best alignment condition is identified finding the values of the pose p that minimize the Root Mean Square Distance (RMSD) with the Levenberg-Marquardt minimization Algorithm (LMA) [73]. The VXL [94] implementation of LMA was used in the present work.

A global reference frame was defined with the x and y axis parallel and z-axis perpendicular to the image plane, with the origin in the center of the image plane. The Euler zxy convention was used for rotations. The Field Of View (FOV) was represented with a diameter of 400 mm. The X-ray source was virtually placed in $F = (0, 0, 1000)$ mm, representing a typical distance of a standard fluoroscope, and pixel spacing was fixed at 0.34 mm. The effects on the final accuracy of the errors associated to the identification of the principal point (xy-coordinates of the X-ray source) and principal distance (z-coordinate of the X-ray source) were disregarded in the present study as already quantified elsewhere [63]. The X-rays were represented by a beam of straight lines and the effect of the geometrical image distortions, caused by the electronics of the image formation chain of real fluoroscopes [62], was not considered in the present study because, dealing with real images, the geometrical distortion can be efficiently corrected using a global spatial warping techniques [60, 61] (see Section 2.3). In the implementation of

the LMA, 3 parameters must be specified: (a) the convergence tolerance on the RMSD ($ftol$), (b) the convergence tolerance on the 6 Degree Of Freedom (DOF) of the pose p ($xtol$), and (c) the step length for forward Jacobian computation (eps).

3.2.2 Algorithm convergence properties

High resolution models of humerus, ulna, and radius were downloaded from the official site of the European project VAKHUM (contract #IST-1999-10954 [77]) and used in the performed simulations. For each model two ADMs were calculated and stored with Distance Map Resolution (DMR) equal to 0.5 and 1 mm. An anatomical reference frame was associated to each bone model according to the International Society of Biomechanics (ISB) recommendations [78]. Each model was then placed in a reference pose (parallel to xy-plane, lateral view, out of plane translation $T_z = 200\ mm$) simulating a typical fluoroscopic frame. Flat shaded projections were generated and the complete contour was extracted and then used for the alignment (Figure 3.1).

The sensitivity (S) of the cost function to each DOF of p was analysed. The RMSD function was evaluated keeping 5 DOFs constant and varying a single DOF at a time, with a step of 0.1 mm/deg, around the reference pose, from -30 to 30 mm/deg for translations and rotations, respectively. The analysis was repeated for humerus, ulna and radius. This permitted to evaluate how the shape and the symmetry of the different bone models influence the minimization. The RMSD with respect to each DOF analysed, can be represented as a cusp. The S of RMSD to the variation of the pose parameters, was defined as the average absolute slope between the left and the right tangents of the curve around its minimum (Figure 3.2).

$$S_p = \frac{1}{2}\left(\left|\frac{RMSD(p_m) - RMSD(p_m + \Delta p)}{\Delta p}\right| + \left|\frac{RMSD(p_m) - RMSD(p_m - \Delta p)}{\Delta p}\right|\right) \tag{3.1}$$

Where p_m is the value of the generic pose parameter p correspondent to the minimum of RMSD. A detailed convergence domain analysis was carried out for different sets of simulation parameters. The minimization was started from 1000

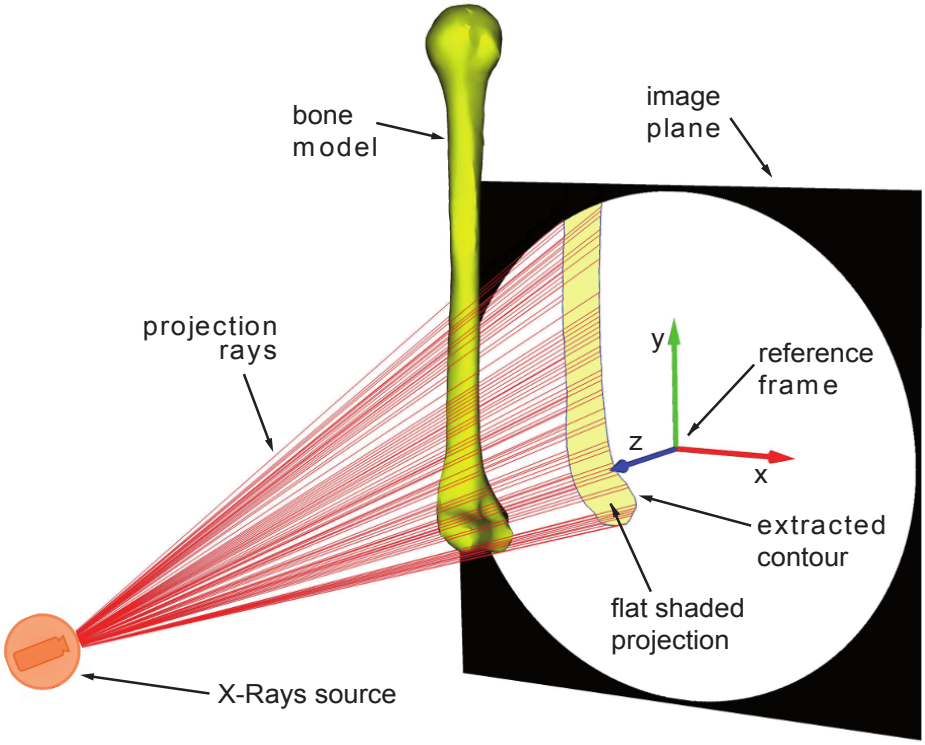

Figure 3.1: Perspective projection model. The bone model is placed in a reference position and a flat shaded projection is generated. The contour points are extracted and the projection lines are back projected towards the X-rays source.

randomly-chosen initial-condition poses among 117649 permutations obtained varying the translations ($\Delta T_x, \Delta T_y, \Delta T_z$) and rotations ($\Delta\Theta_x, \Delta\Theta_y, \Delta\Theta_z$) among the values $-10,\ -7,\ -3,\ 0,\ 3,\ 7,\ 10\ mm/deg$, respectively, around the reference pose. The simulations parameters were initially varied using different values for DMR ($0.5 - 1\ mm$), and *eps* ($10^{-1} - 10^{-4}\ mm/deg$) while *xtol* and *ftol* were both kept fixed at $10^{-3}\ mm/deg$.

3.2.3 Algorithm conditioning

Different authors stressed that the minimization of RMSD is affected by local minima and by the large differences in the sensitivity to the various DOFs [13, 17]. If the minimization starts from initial conditions inside a local minima basin, the pose estimation will be incorrect. Two different solutions were implemented and compared in order to better deal with the problem of local minima. The first, proposed by Fregly et al. [17], involved the sequential (*seq*) minimization of the DOF in order of sensitivity. For this purpose, three groups of DOFs were formed: (*a*) in-plane pose parameters (T_x, T_y, Θ_z); (*b*) out-of-plane rotations (Θ_x, Θ_y); (*c*) out-of-plane translation (T_z). After this three sequential minimization, the RMSD was finally further minimized with respect to the 6 DOFs simultaneously. The second solution ($feat$) involved the use of features extracted from the image to get closer to the real pose before starting the minimization. Two features were calculated on the bone-contour points: (*a*) the direction of maximum variance of the distribution, and (*b*) the farthest point from the field of view border among the projections of the bone-contour point along the maximum variance axis. The first feature was used to evaluate a first guess for the bone model orientation around the projection axis (Θ_z) , while the in-plane translation components (T_x, T_y) were estimated using the second feature. The three DOFs were modified iteratively until convergence, and then the minimization was started as previously described. The analysis was repeated for each bone model, using *seq*, $feat$ and $seq - feat$ together, with 2 values of *eps* ($10^{-1} - 10^{-4}\ mm/deg$) and DMR $= 0.5\ mm$.

3.2.4 Data analysis

For each set of parameters, the final deviations between estimated and reference poses, and the relevant residual RMSD were quantified. Bias and precision of the final estimates of the pose were quantified calculating for each DOF the

median (m) and the interquartile range (iqr). For bias results, a Student's t-test ($P < 0.05$) was performed to determine if the values were statistically different from zero, indicating the presence of a systematic error. Moreover, to measure how outlier-prone the distributions were, the kurtosis (k) was also calculated. To investigate the effects of the different minimization parameters (DMR, eps, seq, $feat$, bone models and initial deviations) on the final estimates and RMSD, an n-way analysis of variance (ANOVA) was performed considering a significance level $\alpha = 0.05$ (with Bonferroni adjustment for multiple comparisons).

3.3 Results

3.3.1 Sensitivity analysis

The cusp shape of RMSD with respect to each DOF, except T_z, was verified, while with respect to T_z, RMSD showed a rounder trend. In particular the trend of the cost function for the humerus is shown in Figure 3.2. Similar trends were obtained also for the ulna and the radius models.

For all the bone models analysed, the sensitivity analysis highlighted the presence of an evident global minimum in correspondence of the reference pose ($\Delta T_i = 0$ and $\Delta \Theta_i = 0$, $i = x, y, z$). This was true for all the 6 DOF but with higher sensitivity for the in-plane DOF, see Table 3.1. In particular, the highest sensitivity was obtained for Θ_z (mean value $8.5 \times 10^{-1} mm \cdot deg^{-1}$) while the smallest was obtained for T_z (mean value $1.2 \times 10^{-3}\ mm \cdot mm^{-1}$). A clear local minimum, however, is shown for the humerus at approximately $\Delta \Theta_x = 15\ deg$ (Figure 3.2), but was not found for the other bone models. All the sensitivity values of the radius, excepted S_{T_x} and S_{Θ_z}, were approximately one order of magnitude smaller than those of ulna and humerus. The RMSD versus ΔT_y was asymmetric: since the analysed bone models were defined with the epicondyles in the middle of the imaging field, the RMSD grew faster when the model is moved further out of the imaging field ($\Delta T_y > 0\ mm$), slower in the opposite direction. The same behaviour was found also for ulna and radius, but, since the bone models were defined in the opposite part of the imaging field, the RMSD grew faster in the opposite direction, thus for $\Delta T_y < 0\ mm$.

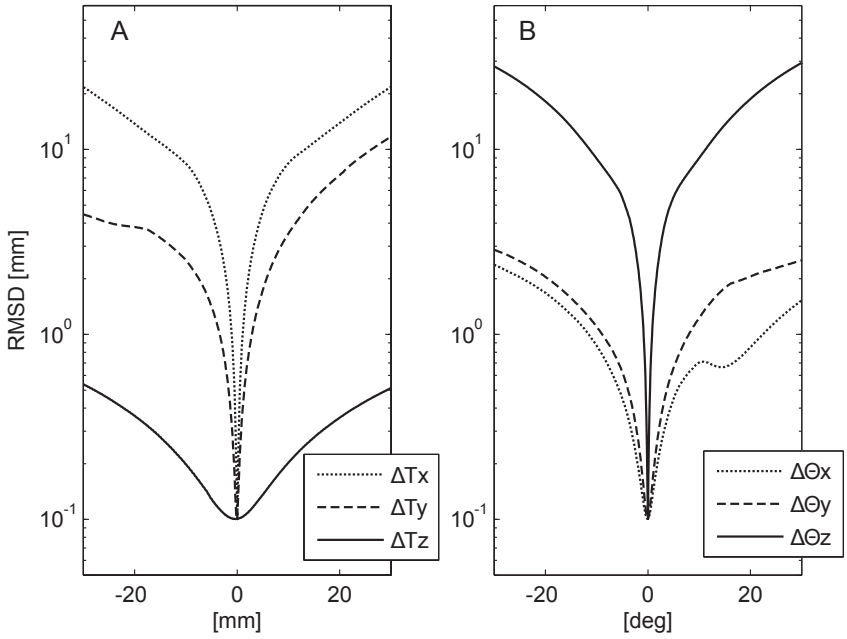

Figure 3.2: The Root Mean Square Distance (RMSD) plotted against the perturbation on the translations (A) and rotations (B) for the humerus bone. The RMSD forms a cusp around its minimum.

Table 3.1: Sensitivity of the RMSD to the variation of each of the 6 DOFs.

DOF	humerus	radius	ulna
S_{T_x} $[mm \cdot mm^{-1}]$	5.5×10^{-1}	5.7×10^{-1}	5.3×10^{-1}
S_{T_y} $[mm \cdot mm^{-1}]$	9.6×10^{-2}	7.6×10^{-2}	1.6×10^{-1}
S_{T_z} $[mm \cdot mm^{-1}]$	1.5×10^{-3}	0.5×10^{-3}	1.5×10^{-3}
S_{Θ_x} $[mm \cdot deg^{-1}]$	8.2×10^{-3}	1.0×10^{-3}	5.0×10^{-3}
S_{Θ_y} $[mm \cdot deg^{-1}]$	1.6×10^{-2}	0.3×10^{-2}	2.0×10^{-2}
S_{Θ_z} $[mm \cdot deg^{-1}]$	8.0×10^{-1}	9.2×10^{-1}	8.4×10^{-1}

3.3.2 Distance map resolution

Results of the convergence domain analysis without conditioning (DMR = 1 mm and 0.5 mm; $eps = 10^{-4}$ mm/deg) showed that a median error lower than 1 mm/deg was produced for each bone model and each DOF. The distributions, however, had large dispersions especially for T_z and Θ_x ($iqr > 5$ mm/deg). Nevertheless, also for the other DOF we found numerous outliers: k ranged from a minimum of 8 (T_y of the radius, DMR = 0.5 mm) to a maximum of 866 (Θ_z of the radius, DMR = 1 mm). For all three bone models, with $eps = 10$ -1 mm/deg, the iqr was larger than 1 mm/deg for in plane DOF and Θ_y, and larger than 10 mm/deg for Θ_x and T_z. Generally, for all three models and both values of eps, the interquartile ranges were always smaller when using a DMR = 0.5 mm rather than 1 mm ($P < 0.05$). We report in Table 3.2 the results obtained for the radius, representing the most problematic case.

Table 3.2: Effects of the distance map resolution on the pose parameters estimates for the radius model.

DOF	DMR = 1 mm			DMR = 0.5 mm		
	m	iqr	k	m	iqr	k
T_x $[mm]$	-0.03	0.01	20.2	-0.02	0.01	50.7
T_y $[mm]$	0.26	0.75	8.4	0.21	0.48	9.7
T_z $[mm]$	0.79	7.15	16.6	-0.2	4.41	47.3
Θ_x $[deg]$	-0.05	8.5	76.8	-0.11	5.5	74.1
Θ_y $[deg]$	-0.22	0.12	140.2	-0.19	0.1	293.7
Θ_z $[deg]$	0.02	0.02	307.8	0.01	0.02	866.2

3.3.3 Sequential alignment

The sequential alignment with DMR = 0.5 mm slightly decreased the number of local minima and outliers identified by the LMA(Figure 3.3): k ranged from a minimum of 1.4 (T_x of the ulna, $eps = 10^{-4}$ mm) to a maximum of 265 (T_z of the humerus, $eps = 10^{-4}$ mm). The mean value of k between the models and the DOFs was equal to 31 for $eps = 10^{-4}$ mm, and equal to 25 for $eps = 10^{-1}$ mm. Using $eps = 10^{-4}$ mm/deg, the optimization of T_x, Θ_z and Θ_y resulted in median < 0.04 mm/deg, $iqr < 0.10$ mm/deg even if Θ_y had a large number of outliers.

T_y had a median < 0.1 mm/deg, with $iqr < 0.50$ mm/deg: Figure 3.3 shows the outliers gathered together only for positive values of T_y. Especially for the radius, the minimization process of Θ_x and T_z tended to prematurely stop during its descent towards the global minimum, resulting in large dispersions (median < 0.05 mm/deg, $iqr = 5.10$ deg and $iqr = 4.10$ mm, respectively). Increasing the step eps to $10 - 1$ mm/deg, for all the three models, the median values for Θ_x and T_z were smaller than 0.08 m/deg, with a dispersion lower than 0.45 mm/deg.

3.3.4 Features

A further reduction of the number of outliers was introduced by the use of features to estimate an initial guess for the in-plane DOF, (Figure 3.4). As for the sequential alignment, the use of a big step ($eps = 10^{-1}$) for the forward Jacobian computation, increased the precision of the estimations of Θ_x and T_z (for the radius $iqr = 0.31$ deg and $iqr = 0.24$ mm respectively). The estimation of T_z was biased for the humerus and radius with medians approximately equal to -0.7 mm, as was Θ_y of the radius (median equal to 0.2 deg), while for the other DOFs and for the ulna the median values were always lower than 0.01 mm/deg. Considering the humerus and both the values of eps, the LMA sometimes converged to the local minimum shown in Figure 3.4 ($T_z \backsimeq -18$ mm, $\Theta_x \backsimeq +18$ mm), keeping the value of k high (medium values: 62 for the humerus, 2.8 for the ulna, 3.3 for the radius).

3.3.5 Features and sequential alignment

The simultaneous use of feat and seq had no significant effect on the final RMSD, nor on the errors of the single DOF estimates ($P > 0.05$). The final results obtained for humerus, ulna and radius with $eps = 10^{-1}$ mm/deg, and DMR=0.5 mm are reported in Table 3.3. The t-test showed that the final estimates were always statistically different from 0, thus biased.

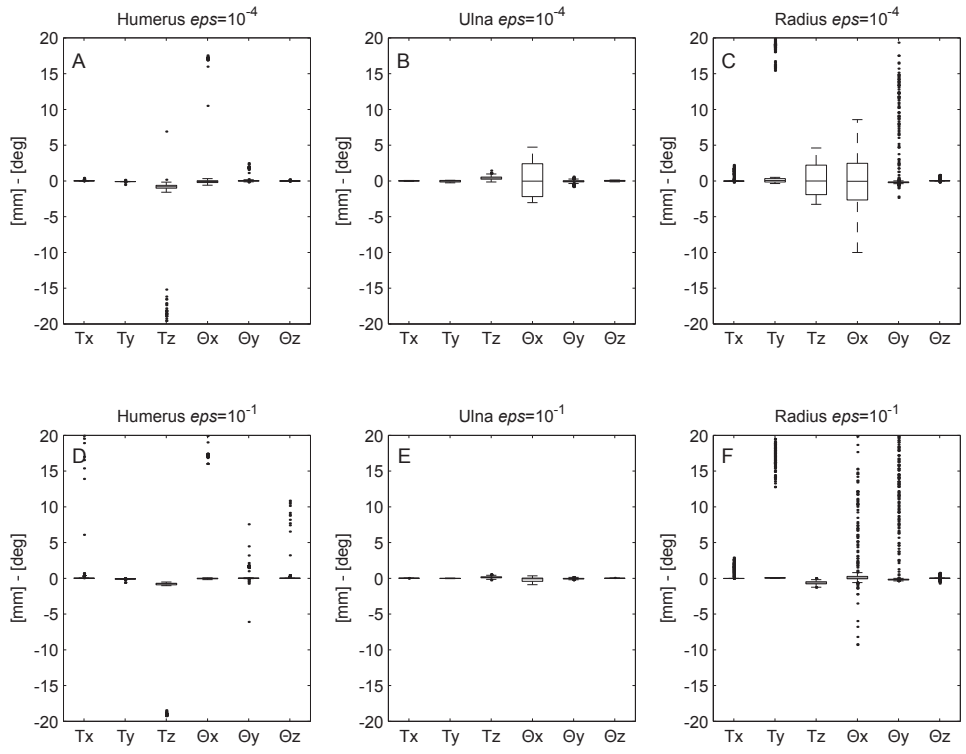

Figure 3.3: Box and whisker plots of the *seq* alignment with DMR $= 0.5\ mm$, (panels A, B, C) $eps = 10^{-4}\ mm/deg$, or $eps = 10^{-1}\ mm/deg$ (panels D, E, F).

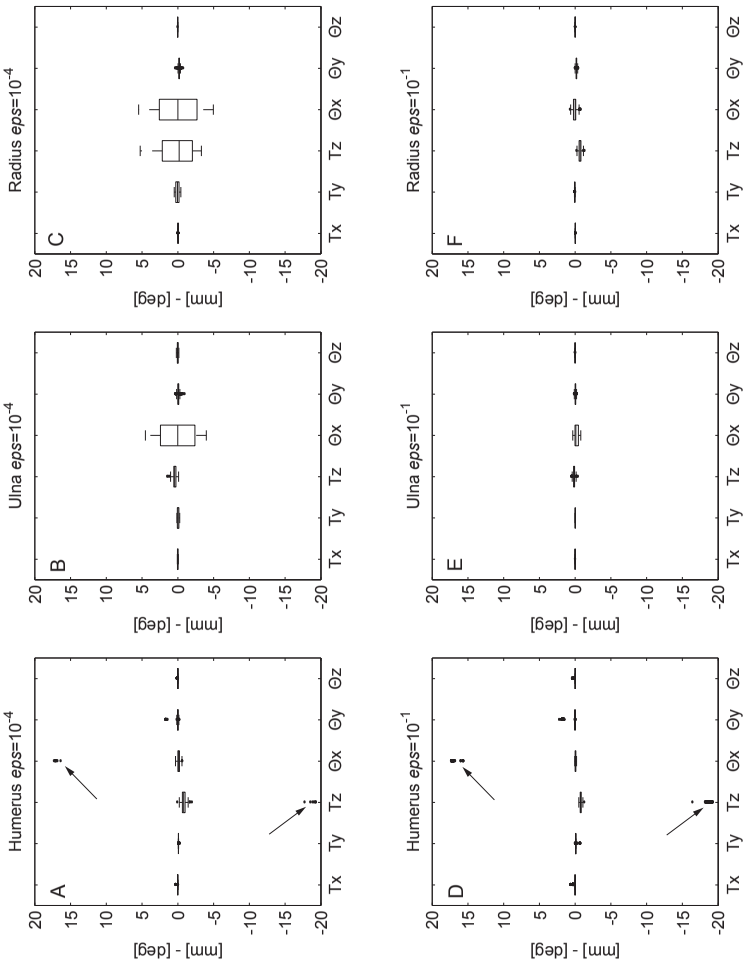

Figure 3.4: Box and whisker plots of the *feat* alignment with DMR = 0.5 mm, (panels A, B, C) $eps = 10^{-4}\ mm/deg$, or $eps = 10^{-1}\ mm/deg$ (panels D, E, F).

Table 3.3: Final accuracy in terms of median (m), interquartile range (iqr) and kurtosis (k) of the pose estimations, for the three bone models with the $seq-feat$ alignment.

DOF	Humerus			Ulna			Radius		
	m	iqr	k	m	iqr	k	m	iqr	k
T_x $[mm]$	0.003	0.004	14.0	0.005	0.008	3.0	-0.021	0.006	4.8
T_y $[mm]$	-0.087	0.005	73.7	-0.018	0.025	2.2	0.051	0.025	3.1
T_z $[mm]$	-0.766	0.153	5.0	0.132	0.155	3.3	-0.692	0.260	3.1
Θ_x $[deg]$	-0.766	0.153	5.0	0.132	0.155	3.3	-0.692	0.260	3.1
Θ_y $[deg]$	0.011	0.032	5.6	-0.044	0.086	3.2	-0.195	0.073	4.2
Θ_z $[deg]$	0.001	0.011	26.8	0.007	0.019	2.9	0.007	0.003	4.9

3.4 Discussion

In this work, a sensitivity analysis and a convergence domain analysis of the minimization algorithm for the pose estimation in 3DF were addressed. The sensitivity analysis showed that the cost function (RMSD) varies differently with each DOF: the in-plane pose parameters have a sensitivity at least one order of magnitude larger than the out-of-plane pose parameters. Moreover, the performed simulation showed that the cost function could have different behaviours depending on the analysed segment (Figure 3.2): considering Θ_x, we found a clear local minimum for the humerus but not for ulna and radius. For all three models, the RMSD with respect to T_y showed an asymmetric trend. That is due to the fact that only a partial part of the bone is included in the imaging field (Figure 3.1), thus, given the long diaphysis of the bone, two different scenarios occur while moving the model along the y-axis: if the models moves further into the imaging field, the projection lines coming from the bone contour points intersect or pass near to the model surface, continuing to give only a little contribution to the increment of the cost function. On the other hand, if the model moves further out of the imaging field, there is no model surface for part of the projection lines to intersect with, increasing their contribution to the cost function.

The findings about the RMSD explained the behavior of the unconditioned LMA, which was found to be noticeably sensitive to the local minima of the

RMSD. Given the longitudinal cylindrical symmetry, the estimations of the pose of long bones were affected by large dispersions not only for T_z, as previously thoroughly reported for the knee prostheses, but also for Θ_x (see Table 3.2). Moreover, for the DOFs with relative small *iqr* such as the in-plane pose parameters, the values of k were high (> 8), that is the distributions were affected by large number of outliers. The ANOVA confirmed the hypothesis that the higher is the Distance Map Resolution (DMR) the more the accuracy and the precision of the technique increase ($P < 0.05$). However, given the limits of the resolution of the fluoroscopic image and of the surface model mesh, a further increasing of DMR would be unnecessary. For the unconditioned minimization, varying the step for the forward Jacobian computation (*eps*) from 10^{-4} to 10^{-1} mm/deg induced a further instability.

To solve the convergence problems of the LMA, the effect of the *seq* alignment on the minimization process was evaluated. When the initial conditions are too far from the reference pose, if not conditioned, the pure algorithm tries to explore the value of the cost function varying all the 6 DOFs simultaneously, risking to move the less sensitive DOF away from the global solution. With the *seq* alignments, instead, the DOFs with larger convergence domain are aligned in a first step, while the more critical (out-of-plane) DOFs are minimized only when closed to the reference pose. Although this technique leads to an improvement of the precision of the estimate (Figure 3.3), the algorithm is still sensitive to local minima, or to local low-sensitivity areas of the cost function that can occur also for the in-plane pose parameters, such as for T_y (Figure 3.2). This could be the cause for the still high number of outliers (mean of $k > 25$) obtained with the *seq* alignment. Varying *eps* from 10^{-4} to 10^{-1} mm/deg permitted to improve the performance of the optimization avoiding the early convergence for the less sensitive DOF (T_z and Θ_x, Figure 3.3). However the problems of convergence are not completely solved, probably because two different DOFs could have a correlated effect on the RMSD, thus, a sequential minimization could interfere with a proper descending to the global minimum.

The use of features completely avoided the problems of the *seq* alignment, because, differently from *seq*, the $feat$ alignment is completely independent from the RMSD and, thus, from its local minima. For our simulations, we used two simple features: [(a)] (a) the direction of maximum variance of the distribution of bone-contour points to extrapolate Θ_z, and (b) a characteristic point such as the farthest from the Field Of View (FOV) border for T_x and T_y. These features

are particularly suitable for long bones, which cannot be completely included in the FOV; for short bones or prosthesis, however, the mean of the coordinates of the contour points can equally be used. These minimization settings, together with a forward Jacobian step $eps = 10^{-1}$ (bigger enough to filter small noisy fluctuation of the RMSD), permitted to significantly reduce m, iqr, and k.

Even if the combined effects of $feat$ and seq did not introduced further improvements ($P > 0.05$), with a fine tuning of the minimization parameters, a high level of precision can be achieved ($iqr < 0.025$ mm/deg for in-plane pose parameters, $iqr < 0.5$ mm/deg for out-of-plane pose parameters) but with a high variability between the models (i.e. considering Θ_x, iqr equal to 0.09 deg for the humerus, and equal to 0.47 deg for the ulna), confirming the hypothesis that the performances of the method should be assessed for each bone model to be analysed.

The results also showed that the final estimate is biased. This is due to the intrinsic limitations of the technique given by the resolution of the fluoroscopic projections and of the distance maps. Moreover, in spite of the fine tuning of the optimization parameters, the local minima showed in Figure 3.2 of the RMSD versus Θ_x for the humerus, seldom caused the LMA to detect false poses. These false poses can generally be easily identified by an operator with a visual feedback of the alignment and, in such cases, the minimization can be repeated starting from a different initial condition.

The results of this study confirm that the accuracy and the precision that can be achieved, especially with the $feat$ alignment, allow the technique to be suitable for the kinematic study of the elbow, but without excluding the complete independence by the operator.

3.5 Conclusions

In the present work, an analytical process was proposed to evaluate the performance of 3DF for its application to the analysis of kinematics of long bones, by means of *in-silico* simulations. The effects of the dominant sources of error such as bone symmetries, distance map resolution and image spacing, were investigated. Solutions were proposed to improve the accuracy and the precision of the method. Given the high variability of the morphology of the bones or prostheses that could be analysed with 3DF, different performance assessment studies should be carried out before undertaking any new application of the technique,

especially for clinical purpose. We focused on the elbow because it allowed to investigate different characteristics of 3DF applied to long bones. Compared to knee prosthesis, which have been widely studied during the past years with 3DF [15, 44, 45], the marked cylindrical longitudinal symmetries of long bones constitute a dominant disturbing factor that could interfere with the final accuracy of the technique.

The robustness of the alignment algorithm applied to the elbow joint was completely characterized. Even if the convergences to local minima was not completely avoided, with a proper conditioning and a fine tuning of the minimization algorithm parameters, excellent results can be achieved in term of low bias and high precision. Moreover, the methods and the findings addressed in this work focusing on mono-planar projections, can easily be extended also to bi-planar 3DF.

In order to achieve a complete automation of the pose estimation algorithm, the problem of local minima should be completely solved. Robust optimization algorithms based on simulated annealing [13] or on Unscented Kalman Filtering [95] have been proposed. These techniques will be implemented and evaluated in future works in combination with the conditioning of minimization based on $feat$ and seq which was proven to effectively improve the performance of LMA. However, the bias errors committed will not be avoided with either of these robust techniques, because the errors are due to characteristics intrinsic to the mono-planar fluoroscopic analysis. Furthermore, when considering other sources of error typical of real fluoroscopic sessions such as the geometric distortions, surface model inaccuracies, errors in the calibration of the fluoroscopic models, and incompleteness of the bone contours, the accuracy would certainly worsen.

Again, all these considerations are to confirm that for application to the kinematics of any particular joint, a detailed validation study should be carried out, especially for clinical studies.

The accuracy and the precision achieved with the feat alignment, allow the technique to be suitable for the kinematic study of the elbow, and most likely even of other long bones, however further *in-vitro* validation must be carried out (see Chapter 5).

CHAPTER

FOUR

MEMETIC ALGORITHMS FOR LIMITATION OF MISALIGNMENTS RESULTING FROM LOCAL MINIMA

4.1 Introduction

Notwithstanding the major improvements introduced in Chapter 3 on the local search algorithm for the pose estimation, there is still room for ameliorations on the optimization algorithm from a global point of view. The use of a robust global optimization algorithm will contribute to a significant reduction of the user interaction during the laborious manual alignment procedure, provided that it is characterized by acceptable computational performance. Costs reduction and reliability improvements may also be foreseen.

To estimate the 6 Degrees Of Freedom (DOFs) of a bone segment in a frame

The material described in this chapter was submitted to:

- **L. Tersi**, S. Fantozzi, R. Stagni: A Memetic Algorithm for Joint Kinematic Estimation with 3D Fluoroscopy, submitted to *IEEE Transaction on Biomedical Engineering*.
- **L. Tersi**, R. Stagni, S. Fantozzi, A. Cappello: Genetic Algorithm as a robust method for the joint kinematics estimation with mono-planar 3D fluoroscopy. In: Proceedings *XVII ESB Conference 2010*. Edinburgh, Scotland UK, 5-8 July 2010.

acquired by 3D video-fluoroscopy (3DF), a 3D model of the bone is virtually moved until it is best aligned to the relevant 2D image. This automatic procedure is typically carried out by means of local iterative optimization algorithms [11, 12]. Different metrics have been used to quantify a cost or a fitness function for the optimization such as: (*a*) the euclidean distance between the contour of the virtual projection of the model and the contour extracted from the fluoroscopic image [43, 51], (*b*) the root mean square distance between the projection lines and the model surface [3], and (*c*) similarity measures between the fluoroscopic image and digitally reconstructed radiographies [52, 53, 54, 55, 56, 96].

Lavallée and Szelinsky [11] proposed for this kind of application the Levenberg-Marquardt minimization Algorithm (LMA), which is a maximum neighborhood method performing an optimum interpolation between the Gauss-Newton and the Steepest-Descent methods [73]. However, the performance of the minimization is affected by the geometry of the bone segments analyzed, and its accuracy could vary considerably because local-minima, caused by occlusions, symmetries or concavities of the models surfaces, could severely interfere with a correct estimation of the pose [18]. Therefore, if gradient-based method such as LMA are used, the technique is highly dependent on the initial guess of the pose for the optimization which is typically specified manually [18]. Consequently, 3DF might currently still be operator-dependent [51] and the application of 3DF is too cumbersome to be suitable for routine clinical practice.

To exploit its potential, a concrete automation of the procedure is then necessary. Different workarounds have been proposed such as: (*a*) the automatic estimation of the initial guess of the pose using geometrical features [18] (Chapter 3), (*b*) multi-scale coarse-to-fine alignments [97], (*c*) collision detection between prostheses components [98], (*d*) approximate evaluation curve to optimize independently the depth position of the other variables [99], or (*e*) the use of metaheuristic global optimization methods such as Genetic Algorithms (GAs) [100] or simulated annealing [13]. Among these, the use of GAs is the most robust and generalizable approach [101]. It could be applied to every kind of joint or pose estimation algorithm and, depending on the contest, it could also be used together with others of the proposed approaches.

First introduced by Holland [102], GAs are population-based search and metaheuristic optimization method belonging to the larger class of evolutionary algorithms. GAs became popular due to their ability to find optimal solution to highly non-linear problems mimicking techniques inspired by natural evolution and ge-

netic dynamics [103], such as inheritance, mutation, selection, and crossover. Following this metaphor, the population is a group of individuals that constitute a set of possible solutions to the problem (chromosomes). Each chromosome is characterized by its own genetic makeup and a fitness (f), i.e. the value of the function to be optimize. f determines also the rate a certain chromosome can reproduce and then its possibility to transmit its gene pool to the future generations through inheritance. In this way, the population will eventually evolve towards best solutions and then to the global optimum of the problem.

The performance of any optimization algorithm depends on the mechanism for balancing the two conflicting objectives, which are (a) exploiting the best solutions found so far and, at the same time, (b) exploring the search space for new promising solutions. The power of GA comes from their ability to theoretically combine both exploration and exploitation in an optimal way [102]. However, there are problems in practice which arise from the finite population size, which influences the sampling ability of a GA and as a result affects its performance. Nonetheless, a GA is able to incorporate other techniques within its framework to produce a hybrid that reaps the best from the combination. Hybrid GAs, also referred as Memetic Algorithms (MAs) [104], have received significant interest in recent years because, incorporating a local search method (metaphor of learning) within a GA can help to accelerate the search towards the global optimum [103]. In nature, only information in an organism's genotype can be transmitted to the next generation. However, the discredited Lamarckian notion that offspring can inherit acquired changes can be implemented in MAs. An intermediate idea is due to Baldwin: chromosomes can encode a predisposition for learning beneficial behaviors. A Baldwinian mechanism for MAs carries out local search and assigns any improved fitness as the fitness of the chromosome, but does not modify the chromosome; this fitness represents the chromosome's inherent fitness and the organism's capacity to improve.

Being MA scarcely influenced by local minima, its use in the 3DF context could considerably reduce the user interaction preserving the overall computational time to clinically suitable level. In the present work, we propose a MA for the operator independent pose estimation in 3DF. By means of computer simulation, we analyzed the convergence property of the modified version of the pose estimation algorithm proposed by Lavallée and Szelinsky [11] described in 1.3.1. Even for this evaluation study we focused on the elbow, because, as highlighted in [18], it is particularly suitable to evaluate the performance of the method (see

Chapter 3). To the same aim, even this Chapter focused on mono-planar fluoroscopy because, in contrast with bi-planar fluoroscopy which is more robust, it can best highlight the eventual limitations of the technique. Moreover, foreseeing clinical application of the method, mono-planar fluoroscopy can investigate bigger volume with smaller X-ray dose for the patient, and with simpler instrumentation.

In this evaluation study we considered (*a*) the geometric characteristic of the bone models, (*b*) the resolution of the fluoroscopic projection images, (*c*) the resolution of Adaptive Distance Map (ADM), and (*d*) the convergence properties of the new MA as the only sources of errors. Confounding effects caused by the geometric distortions, by errors in the calibration of the fluoroscopic models, or by the incompleteness of the bone contours were disregarded in the present study but treated elsewhere (Section 2.3, Chapter 6).

The aim of the present study was to investigate the suitability of MA applied to the 3D fluoroscopic analysis of elbow bones kinematics, through a detailed exploration of the convergence domain of the minimization algorithm, in order to quantify and optimize measurement reliability in terms of accuracy and precision.

4.2 Methods

An established technique, described in section 1.3.1, was implemented to estimate the 3D pose of an object of known 3D geometry given its mono-planar fluoroscopic projection [3].

A global reference frame was defined with the x and y axis parallel and z-axis perpendicular to the image plane, and with the origin at the center of the image. The Euler zxy convention was used for rotations. The X-rays source was virtually placed in $F = (0, 0, 1000)$ mm, representing a typical distance of a standard fluoroscope, and pixel spacing was fixed at 0.3 mm for 1024x1024 pixel images. The effects on the final accuracy of the errors associated to the identification of the principal point (xy-coordinates of the X-ray source) and principal distance (z-coordinate of the X-ray source) were disregarded in the present study as already quantified elsewhere [63]. The X-rays were represented by a beam of straight lines and the effect of the geometrical image distortions, caused by the electronics of the image formation chain of real fluoroscopes [62], was not considered in the present study because, dealing with real images, the geometrical distortion can be efficiently corrected using global spatial warping

techniques [60, 61].

A new global optimization algorithm for the pose estimation based on MA was developed and will be illustrated in the following sections.

4.2.1 Memetic algorithm

Houck et al. [105] compared Baldwinian, and Lamarckian strategies in MA for several non-linear function optimization, obtaining the best results with a partially Lamarckian strategy that was applied to only 20% to 40% of the chromosomes. However, there is no evidence of the primacy of the Lamarckian approach in all the situations [103], thus in the present work we have evaluated the performance of both the strategies. The algorithm flowchart is depicted in figure (4.1); details of the implementation will be given below and typical parameters values are reported in table 4.1.

Initialization

The first fundamental MA design operation is to find a proper representation of the searching space domain for the optimization. This means to define a coding system for the 6 DOFs (chromosome) representing the pose. A range of value for each variable was defined considering the exploitation-exploration trade-off (T_{range}, Θ_{range}). Each variable was represented by a binary code. In order to guarantee a better stability in the algorithm evolution, the Gray code [106] was chosen in the way that two adjacent values in the variable space are represented with a small number of different bits. Moreover it is best suited to code the periodic rotation domain. The number of bit (N_{bit}) was chosen in order to assure a resolution of the order of 10^{-3} mm/deg. The genoma of each individual is then a string of $6 \cdot N_{bit}$ bits. The range is centered on an initial guess, which in a real session could be the alignment of the previous frame. The number of individuals (N_{ind}) of the population is designed considering the trade off between exploration and computational time. The algorithm is initialized generating a first set of N_{ind} random individuals uniformly distributed in the chosen domain.

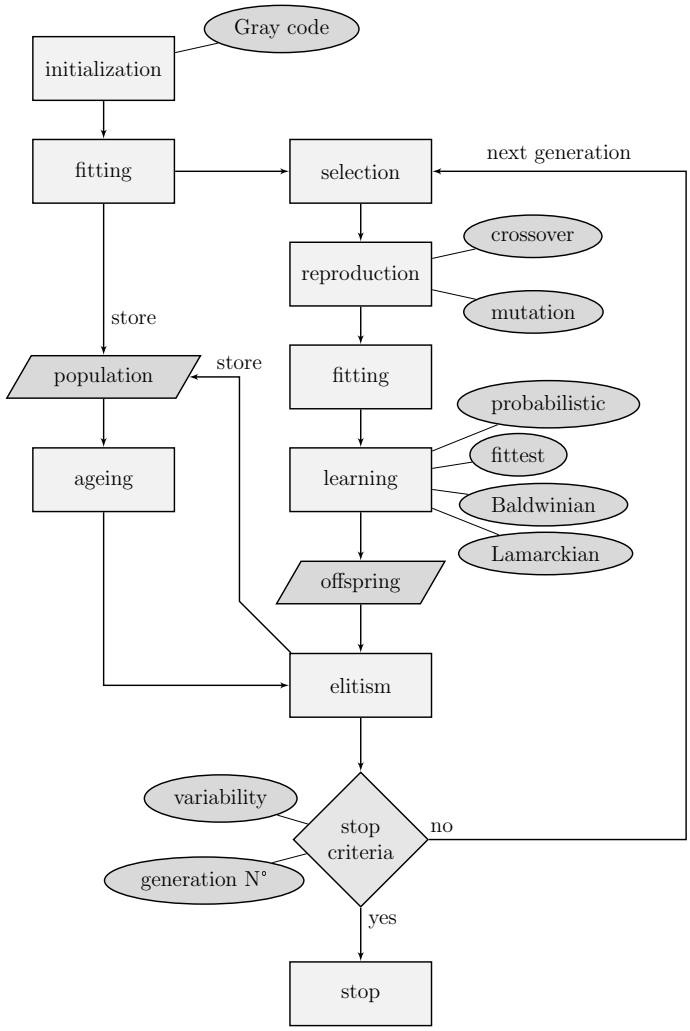

Figure 4.1: Genetic Algorithm flowchart. Given a suitable coding, an initial random population is generated. For each individual, f is calculated as the inverse of Root Mean Square Distance (RMSD). The best individuals are selected to generate an offspring through reproduction. Each new chromosome will probabilistically go through a learning process. The new generation is then formed by the best individuals among the aged previous generation and the offspring. The process is then iterated untill the convergence of the algorithm, detected evaluating stop criteria.

Fitting

For each individual, the fitness function f is calculated as the inverse of RMSD (see equation 1.3).

$$f(p) = \frac{1}{RMSD(p)} = \frac{1}{\sqrt{\frac{1}{n}\sum_{i=1}^{n}[d(S_m(p), l_i)]^2}} \tag{4.1}$$

where $S_m(p)$ is the surface of the model m positioned in the pose

$$p = (T_x,\ T_y,\ T_z,\ \Theta_x,\ \Theta_y,\ \Theta_z) \tag{4.2}$$

and l_i are the n projection lines (see section 1.3.1 for details).

Selection

N_{ind} couples will be formed and each couple will generate one child. The selection criteria of the parents for the reproduction is based on the fitness values. For every couple, the first approximation of the probability that the individual j is chosen to be a parent is equal to:

$$P(j) = 2f_j \cdot \left[\sum_{i=1}^{N_{ind}} f_i\right]^{-1} - \lambda \tag{4.3}$$

Thus, the individuals with a larger f are most likely to become parents and they can reproduce even more than once per generation. The λ coefficient is subtracted to consider that an individual cannot reproduce with itself. Being the number of couples equal to the number of individuals, N_{ind} will be preserved during the generations.

Reproduction

The operator that generates a child given the gene pools of the parents is called crossover. In the present work we implemented a full multi-point crossover. This means that each bit of the child is chosen between the ones of its two parents

with a probability dependent on f:

$$P(b_k^{child} = b_k^{father}) = \frac{f_{father}}{f_{father} + f_{mather}}, \qquad \forall\ k = 1, \ldots, 6 \cdot N_{bit} \tag{4.4}$$

where b_k is the k-th bit of the genoma, considering the 6 DOFs. To increase the exploration capability of the algorithm, a mutation operator was also implemented that commutes a bit of the genoma with a probability equal to P_{mut}.

Learning

The local search was implemented as few iterations (maximum 10, correspondent to 60 evaluations of f, or less in case of early convergence) of a features-enanched LMA as proposed in chapter 3 [18]. Briefly, the features permitted to give a first estimation of the in-plane pose parameters (T_x, T_y, and Θ_z) improving the convergence rate of the LMA. The VXL implementation of the LMA was used [94]. As suggested in [105], a partial learning scheme was applied. The LMA was applied (a) probabilistically to randomly chosen chromosomes (with a probablity P_{LMA}), (b) and deterministically to every new candidate to be optimum, thus every time a new fittest chromosome was found. In the Lamarckian approach, the chromosome was effectively modified, while for the Baldwinian approach, only the value of f was modified without modifying the chromosome bit-string.

Ageing and elitism

After the offspring is generated, it is merged to the previous generation and the best N_{ind} chromosomes between the two are selected as a new generation. This process goes with the name of elitism, and increases the convergence rate. Nevertheless, a risk of getting stuck in local minima is introduced. Thus, to increase the exploration capability of the MA, the fitness of the chromosomes of the previous generation is multiplied by a certain coefficient $a < 1$ simulating the ageing process, and thus decreasing the chances to reproduce of the old chromosomes already exploited in previous generations.

Stop criteria

Two different stopping criteria were considered to terminate the algorithm: (a) a maximum number of generations (N_{gen}) without any new candidate to be opti-

Table 4.1: Standard MA parameters setting.

Parameter	Value
N_{ind}	100
N_{bit}	18
P_{mut}	0.04
P_{LMA}	10%
LMA_{it}	< 10
a	0.9
N_{gen}	10
σ_{min}	2 mm/deg

mum, and (b) the convergence was detected when the maximum dispersion among the population DOFs in the current generation was below a certain threshold (σ_{min}). The dispersion was quantified computing the standard deviation (σ) of the distribution of each DOF.

4.2.2 Performance evaluation

The same high resolution models of humerus, ulna, and radius downloaded from the official site of the European project VAKHUM (contract #IST-1999-10954 [77]) for the previous tests, were used in the performed analysis. For each model an ADM was calculated and stored with DMR equal to 0.5 mm. An anatomical reference frame was associated to each bone model according to the International Society of Biomechanics (ISB) recommendations [78]. The RMSD cost function, and its inverse f, are non-linear functions of the 6 DOFs. To give a qualitative description of the cost function, the bone model was virtually placed in a reference position and the RMSD was evaluated varying T_y and Θ_x with a step of 0.1 mm/deg, keeping the other DOFs constant at the correct values. The subsequent tests were carried out placing each model in a set of random reference poses

$$p^{ref} = (T_x^{ref}, T_y^{ref}, T_z^{ref}, \Theta_x^{ref}, \Theta_y^{ref}, \Theta_z^{ref}) \tag{4.5}$$

simulating typical fluoroscopic frames. The extent of the domain for the reference pose was referred as Δ_T and Δ_Θ for translations and rotations respectively.

Table 4.2: Ranges of the reference poses (Δ_T,Δ_Θ), and of the MA initial population (T_{range}, Θ_{range}). All the reference poses are centered in $\overline{p} = (0, 0, 300, 0, 0, 0)$. T_{range} and Θ_{range} is centered in $\overline{p}$ for trials 1 and 2, and in $T^{in}_{xyz} = T^{ref}_{xyz} \pm 25\ mm$ and $\Theta^{in}_{xyz} = \Theta^{ref}_{xyz} \pm 25\ deg$ for trial 3.

Trials	Learning	Δ_T [mm]	Δ_Θ [deg]	T_{range} [mm]	Θ_{range} [deg]
1	Lamarckian	± 50	± 90	± 60	± 180
	Baldwinian	”	”	”	”
2	Lamarckian	± 10	± 10	± 60	± 180
	”	± 25	± 25	”	”
	”	± 50	± 50	”	”
	”	± 50	± 90	”	”
	”	± 50	± 180	”	”
3	Lamarckian	± 50	± 180	$T^{in}_{xyz} \pm 50$	$\Theta^{in}_{xyz} \pm 50$

For every reference pose p^{ref}, a flat shaded projection was generated and the complete contour was extracted and then used for the alignment. Different tests were carried out varying the MA parameters in order to test the effects of the different bone models, the best learning method between the Lamarckian and the Baldwinian, and the accuracy and precision of the pose estimation algorithm.

1. **Learning strategies:** for each model, two sets of pose estimations were carried out with $\Delta_T = 50\ mm$ and $\Delta_\Theta = 90\ deg$ using the two different learning strategies. The reference poses domains and T_{range} and Θ_{range} were centered in $\overline{p} = (0, 0, 300, 0, 0, 0)$.

2. **Accuracy test:** the accuracy of the pose estimation was evaluated for different sets of Δ_T and Δ_Θ according to table 4.2. The domain extent were centered in $\overline{p}$.

3. **Precision test:** the precision of the algorithm was evaluated analyzing the convergence properties of the alignments with 15 different reference poses in the domain $\Delta_T = 50\ mm$ and $\Delta_\Theta = 180\ deg$ centered in $\overline{p}$ (see Table 4.3). For every reference pose, the alignment was repeated with $T_{range} = 50\ mm$ and $\Theta_{range} = 50\ deg$ but with different centers of the domain around the reference pose: the domain was centered in all the 64 possible permutations

Table 4.3: Reference poses for precision test. The relative flat shaded projections are depicted in Figure 4.4.

Pose	T_x^{ref}	T_y^{ref}	T_z^{ref}	Θ_x^{ref}	Θ_y^{ref}	Θ_z^{ref}
a)	0.0	0.0	300.0	0.0	0.0	0.0
b)	-32.1	-17.8	260.7	-25.0	-38.5	141.4
c)	46.4	32.1	325.0	65.0	-141.4	38.5
d)	-46.4	46.4	289.2	-55.0	64.2	167.1
e)	25.0	17.8	282.1	15.0	-115.7	12.8
f)	-25.0	-32.1	332.1	55.0	-167.1	90.0
g)	-17.8	25.0	317.8	25.0	38.5	115.7
h)	-10.7	-39.2	346.4	-45.0	-64.2	-64.2
i)	-39.2	-10.7	267.8	5.0	12.8	-115.7
j)	3.5	-3.5	253.5	-65.0	90.0	-167.1
k)	39.2	3.5	275.0	35.0	115.7	-38.5
l)	-3.5	-25.0	303.5	-15.0	-12.8	64.2
m)	10.7	10.7	310.7	-35.0	167.1	-90.0
n)	17.8	39.2	339.2	45.0	141.4	-12.8
o)	32.1	-46.4	296.4	-5.0	-90.0	-141.4

obtained varying each DOF between the values ± 25 mm/deg.

$$T_{xyz}^{in} = T_{xyz}^{ref} \pm 25 \ mm \tag{4.6}$$

$$\Theta_{xyz}^{in} = \Theta_{xyz}^{ref} \pm 25 \ deg \tag{4.7}$$

The maximum value of Δ_T was set to 50 mm in order to assure that a significant part of the fluoroscopic projection felt inside the Field Of View (FOV). Moreover, to avoid reference poses redundancy, the maximum $\Delta_{\Theta x}$ was equal to 90 deg. In order to optimally explore the whole pose domain, a Latin Hypercube Square design [107] was used with 100 (for trials 1 and 2) and 15 (trial 3) different levels for each of the 6 DOFs.

It is important to stress that, differently from previous approaches [3, 18], these *in-silico* tests were carried out in a completely unsupervised way. This means that the algorithm investigate the entire domain of the possible poses, without any a-priori knowledge that could be specified by the user in a real fluoroscopic session.

4.2.3 Data analysis

For each set of parameters, the final deviations between estimated and reference poses, and the relevant residual RMSD were quantified.

The Kolmogorov-Smirnov test was used to investigate whether the error distribution of each DOF was normal. Differences between the two learning strategies were tested with a Mann-Whitney U-test. Bias and precision of the final estimates of the pose were quantified calculating for each DOF the median (m) and the interquartile range (iqr). For bias results, a Wilcoxon test ($P < 0.05$) was performed to determine if the values were statistically different from zero, indicating the presence of a systematic error. Moreover, to measure how outlier-prone the distributions were, the kurtosis (k) was also calculated. All statistical analyses were performed with NCSS (NCSS, Kaysville, USA).

4.3 Results

A simplified representation of the cost function RMSD was obtained varying only T_y and Θ_x. As an example, figure 4.2 shows the resulting surface for the humerus in side view (left panel), and top view (right panel). The global minimum basin (deep blue) is small and surrounded by local minima, moreover, for positive Θ_x, there is a wide flat area that may interfere with a proper identification of the global minimum.

Nonetheless, the MA was robust enough to find the global minimum in an acceptable amount of time ($\sim 1-2\ min$). Figure 4.3 shows a typical evolution of the initial population through the generations. The humerus bone model was placed in a reference pose $p^{ref} = (0, 0, 300, 0, 0, 0)$. The in-plane-pose parameters are the first to converge, and the last one is T_z. When its standard deviation is smaller than σ_{min} the stop criterion stops the evolution. Looking at the second generation of Θ_z it is possible to note that the symmetric pose at $\pm 180\ deg$ was also explored but easily excluded from the evolution.

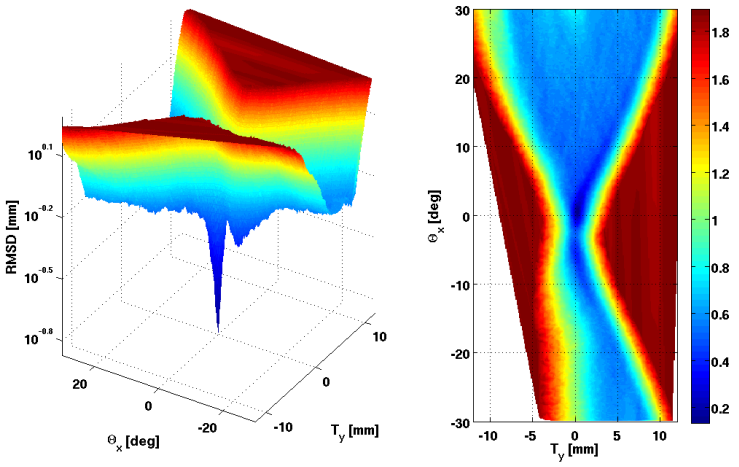

Figure 4.2: Cost function RMSD as a function of the only T_y and Θ_x. The global minimum attraction basin is limited and surrounded by many local minima basins.

The Kolmogorov-Smirnov test performed on every DOF error demonstrated that the distributions were not normal. Non-parametric statistical tests were used to analyze the results.

4.3.1 Learning strategies

The Mann-Whitney U-test did not highlighted any statistically significant difference comparing the error distributions between the pose estimated using the Lamarckian or the Baldwinian learning strategy ($p > 0.05$). The computational weight, however, was higher for the Baldwinian learning as testified by comparing the number of evaluations to convergence of the two methods with the Mann-Whitney U-test ($p < 0.01$). Table 4.4 shows m, iqr, k and the average number of evaluations of f. Similar results were obtained for the three bone models, and thus the Lamarckian approach was used in the next experiments.

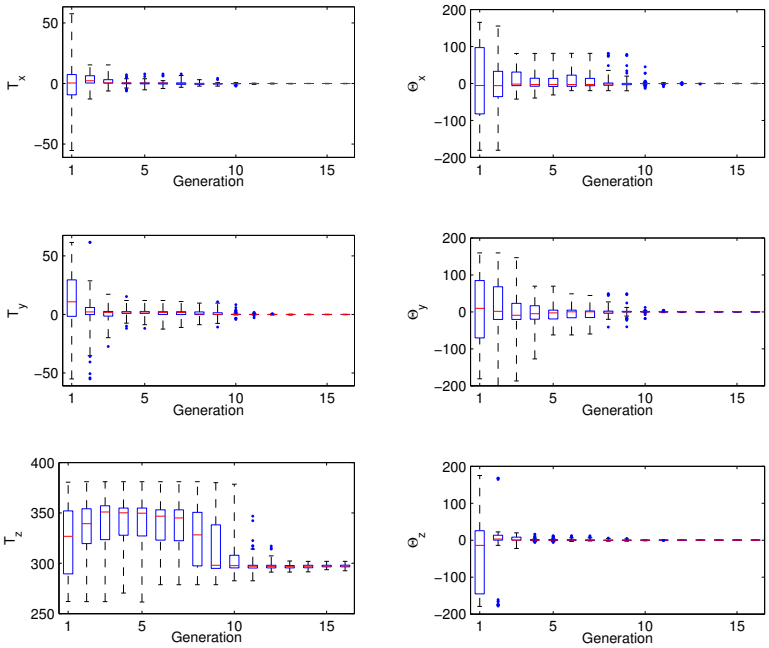

Figure 4.3: Box and whiskers plot of the distribution of the DOFs of the entire population during the MA evolution.

Table 4.4: Effects of the learning strategies.

DOF	Lamarckian			Baldwinian		
	m	iqr	k	m	iqr	k
T_x $[mm]$	-0.04	0.54	41.39	-0.05	0.51	26.65
T_y $[mm]$	0.03	0.63	26.06	0.01	0.61	21.94
T_z $[mm]$	3.40	3.47	16.35	2.97	4.64	12.18
Θ_x $[deg]$	0.10	0.53	12.15	0.12	0.61	9.98
Θ_y $[deg]$	-0.03	0.52	21.84	-0.11	0.88	15.57
Θ_z $[deg]$	-0.01	0.18	18.43	-0.01	0.24	16.32
N_{eval}	13560	9051	5.83	27382	21084	13.34

4.3.2 Accuracy

The extent of the reference pose domain had an effect on the accuracy of the estimations. Table 4.5 resumes the parameters of the error distributions related to every DOF for the humerus. If the reference poses were close to the center of T_{range} and Θ_{range} ($\Delta_T = \pm 10\ mm$,$\Delta_\Theta = \pm 10\ mm$), the convergence of the MA was fast (approximately 8000 evaluations of the fitness function). The number of generations to converge got larger when the reference poses to be estimated were spread in the whole fluoroscopic domain: approximately 15000 evaluations for $\Delta_T = \pm 50\ mm$, $\Delta_\Theta = \pm 180\ mm$.

The bias and the dispersion of the error, as quantified by m and iqr increased in the same way. Similar results were obtained for the three bone models.

Table 4.5: Effects of the domain extent of the reference poses for the accuracy tests on humerus model. Median (m), interquartile range (iqr) and kurtosis (k) of the error distributions and of the number of evaluations of the fitness function (f).

DOF	$\Delta_T = \pm 10$ $[mm]$ $\Delta_\Theta = \pm 10$ $[deg]$			$\Delta_T = \pm 25$ $[mm]$ $\Delta_\Theta = \pm 25$ $[deg]$			$\Delta_T = \pm 50$ $[mm]$ $\Delta_\Theta = \pm 50$ $[deg]$			$\Delta_T = \pm 50$ $[mm]$ $\Delta_\Theta = \pm 90$ $[deg]$			$\Delta_T = \pm 50$ $[mm]$ $\Delta_\Theta = \pm 180$ $[deg]$		
	m	iqr	k	m	iqr	k	m	iqr	k	m	iqr	k	m	iqr	k
T_x $[mm]$	-0.02	0.06	4.5	-0.06	0.26	34.2	0.01	0.61	9.5	-0.00	0.58	15.6	-0.01	0.54	7.9
T_y $[mm]$	0.05	0.09	4.2	0.06	0.25	16.9	0.03	0.65	14.2	0.05	0.60	62.3	0.04	0.57	5.4
T_z $[mm]$	1.82	3.16	2.7	5.38	3.19	19.3	5.02	4.03	8.3	4.30	5.53	5.4	4.64	22.64	6.2
Θ_x $[deg]$	0.07	0.25	3.6	0.16	0.39	43.0	0.08	0.56	17.5	0.07	0.75	10.5	0.27	17.97	5.4
Θ_y $[deg]$	0.08	0.19	4.3	0.04	0.54	30.9	-0.00	0.60	23.4	-0.02	0.54	12.9	-0.00	1.07	6.9
Θ_z $[deg]$	-0.05	0.08	3.6	-0.11	0.10	42.6	-0.06	0.13	50.3	-0.04	0.16	32.3	0.01	0.24	30.8
N_{eval}	8377	2908	5.3	12111	6830	6.5	15140	8323	4.8	13639	11933	6.0	15233	9228	3.2

4.3.3 Precision

The alignment was repeated starting from different domains around the reference poses and keeping the ranges of the initial MA population to $T_{range} = 50\ mm$ and $\Theta_{range} = 50\ deg$. As depicted in Table 4.6, the different bone models were analyzed with approximately the same number of fitness function evaluations ($N_{eval} \simeq 8500$), but led to variable errors especially for the out-of-plane pose parameters. The distributions of the errors showed increasing bias and dispersion with the symmetries of the models, being the humerus the less (for T_z $m = 3.26\ mm$, $iqr = 1.52\ mm$), and the radius the most symmetric (for T_z $m = 8.23\ mm$, $iqr = 3.64\ mm$).

However, a large variability of the error dispersions with respect to the relevant reference poses was found. Figure 4.4 shows how for each DOF the iqr varies with the reference pose. In particular, Figure 4.4a indicates that, for the humerus, the iqr is unrelated to all the DOFs reference poses except to Θ_x^{ref}. The iqr is lower than 1, if $\left|\Theta_x^{ref}\right| < 40\ deg$, but increases when approaching a pose closer to gimbal lock. Given the Euler zxy convention, in fact, the gimbal lock occurs at $\Theta_x = \pm 90\ deg$.

The same effect was found both for the ulna (Figure 4.4b) and the radius (Figure 4.4c), however the graphs indicate also that, for ulna and radius, Θ_y^{ref} introduce an error related to the model symmetry. The alignment is easier keeping the model closer to the image plane (low T_z^{ref}), but the error is dominated by Θ_x^{ref}. The reference pose j, in fact, has a low T_z^{ref} but, being close to the gimbal lock pose ($\Theta_x^{ref} = -65\ deg$), iqr is large.

4.4 Discussion

The simplified bi-varied surface of the cost function for the pose estimation, RMSD, is characterized by a limited global minimum basin, surrounded by many local minima, and wide flat areas that may not provide enough informations for a proper convergence of local optimization algorithms (Figure 4.2). Furthermore, the interference of local optima on the global convergence increases when considering all the 6 DOFs. To obtain reliable results it is then needed an extensive exploration of the whole domain that the local optimization algorithms cannot provide.

The developed MA proved to be a robust and accurate tool to deal with this

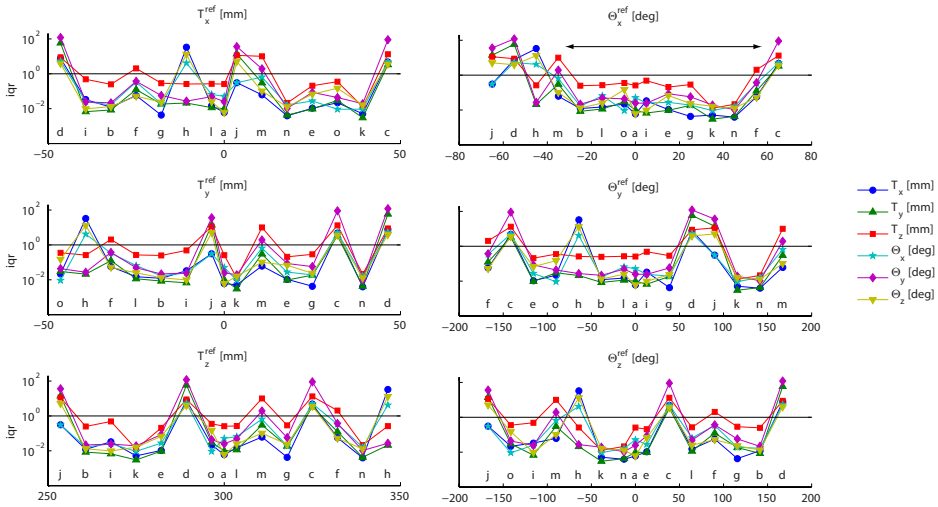

(a) Humerus

Figure 4.4: Variability of the *iqr* with respect to the reference poses (see Table 4.3). For every models, the *iqr* is correlated to the Θ_x^{ref}, but also to Θ_y^{ref} for ulna and radius . The alignment is easier keeping the model closer to the image plane (small T_z^{ref}), but the error is dominated by Θ_x^{ref} as testified by the reference pose j. The horizontal black line corresponds to $iqr = 1\ mm/deg$

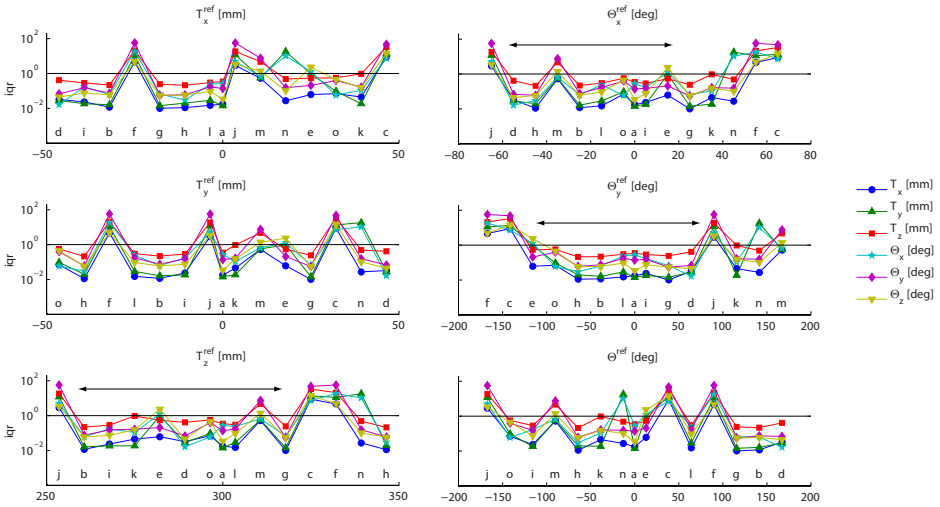

(b) Ulna

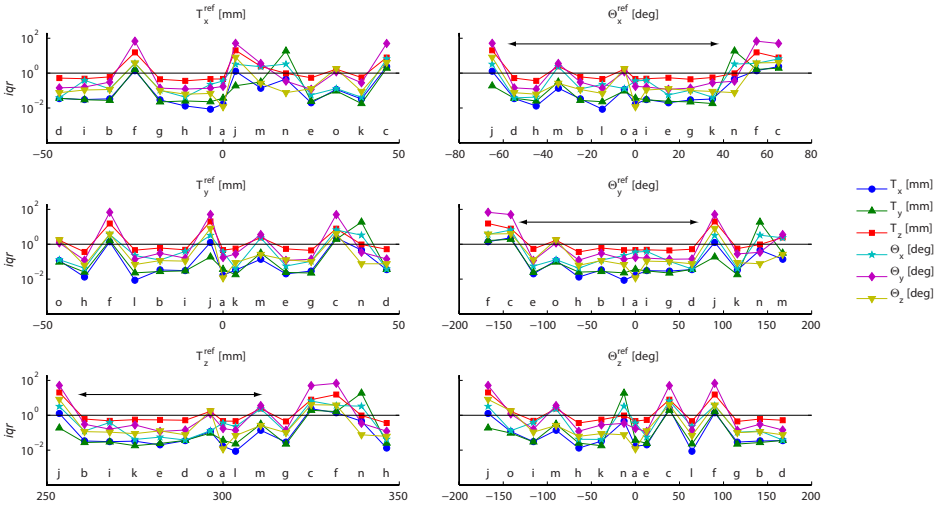

(c) Radius

Table 4.6: Precision tests on humerus, ulna, and radius models. Median (m), interquartile range (iqr) and kurtosis (k) of the error distributions and of the number of evaluations of the fitness function (f).

DOF	Humerus			Ulna			Radius		
	m	iqr	k	m	iqr	k	m	iqr	k
T_x $[mm]$	-0.01	0.34	34.8	0.04	0.56	43.9	0.04	0.85	79.6
T_y $[mm]$	0.01	0.49	17.0	0.11	0.62	22.7	0.02	0.80	50.6
T_z $[mm]$	3.26	1.52	11.4	5.12	2.31	9.9	8.23	3.64	14.3
Θ_x $[deg]$	0.05	0.50	41.6	-0.41	1.39	26.5	-0.07	2.13	42.8
Θ_y $[deg]$	0.04	0.33	14.8	0.04	0.62	15.0	0.10	1.27	15.6
Θ_z $[deg]$	-0.04	0.20	36.4	0.02	0.16	45.2	0.04	0.20	186.0
N_{eval}	8414	5512	9.1	7868	4827	8.2	9678	6576	10.1

ill conditioned optimization problem. The accuracy and precision tests allowed to quantify the performance of the algorithm, investigating the effects of the various algorithm parameters. The accuracy test indicated that it is easier to estimate poses that are approximately at the center of the investigating domain. This finding allowed the formulation an operative advice: with the previous optimization algorithm the user had to provide manual initial guess for the poses of every frame. With the new MA, instead, it is possible to obtain reliable results starting the alignment for the first frame using large T_{range} and Θ_{range}. In a second step, it is advisable to repeat the alignment with a reduced domain and to propagate the estimated pose as the center of the search for the following frames. This procedure is much more robust than the current analysis protocol which propagate the pose as the initial guess for the local optimization, which may not be inside the global optimum attraction basin for fast movements. With $T_{range} = \pm 25\ mm$ and $\Theta_{range} = \pm 25\ deg$ an iqr of the order of the lower bound determined by the pixel dimension ($\sim 0.3\ mm$) can be obtained, however the accuracy of the out-of-plane translation still remain a crucial issue.

The simulations to test the precision of the algorithm were carried out repeating the alignments starting from different poses around the reference p^{ref} and keeping the ranges of the initial MA population to $T_{range} = 50\ mm$ and $\Theta_{range} = 50\ deg$. These values were smaller as compared to the ones of the accuracy test, but still large enough to assure a good exploration. Investigating

the trend of the *iqr* with respect to the reference absolute poses, it was possible to understand that the reliability of the procedure depends on the absolute poses of the segments. The *iqr*, which quantified the repeatability of the technique, was lower than 1 mm/deg if the absolute orientation of the segments avoided poses nearly parallel to the image plane (i.e. see poses *a), i), l*) in Figure 4.4 and Table 4.3), but the *iqr* became larger for poses approaching the gimbal lock or which generated symmetric silhouettes (i.e. poses *c), d), f), j), h)*). Two possible explanations stem from these results:

- given the defined anatomical reference frame, the gimbal lock occurs when the segments are nearly orthogonal to the image plane; in this situation, the modifications of the contours following any rotations do not carry significant information for the pose estimation;
- the Euler angles are not a robust representation of the rotations for a proper evolution of the MA.

To deal with the first limitation, when designing a joint kinematics investigation protocol, it is important to consider that, for long bones, the gimbal lock may interfere with the reliability of the estimation. The main movement must occur in the in-plane direction, and the task must avoid the occurrence of poses that will be projected as symmetric silhouettes. Moreover, a different representation of the rotations (i.e. based on quaternions) may improve the stability of the algorithm even for critical poses, but further investigation are needed to confirm this hypothesis.

As compared to the local search methods, the GA introduces an increased computational weight for the analysis. However, this is largely overcome by the elimination of the manual user interaction for the alignment. The manual alignment may last from 10 seconds to a couple of minutes per frame depending on the skills of the user, which may become hours for long acquisitions and high frame rates. Moreover, the MA can improve the computational performances of the pose estimation algorithm especially if the Lamarckian learning strategy is adopted.

4.5 Conclusions

The aim of the present Chapter was to investigate the suitability of Memetic Algorithm (MA) applied to 3DF for the analysis of long bones kinematics, through

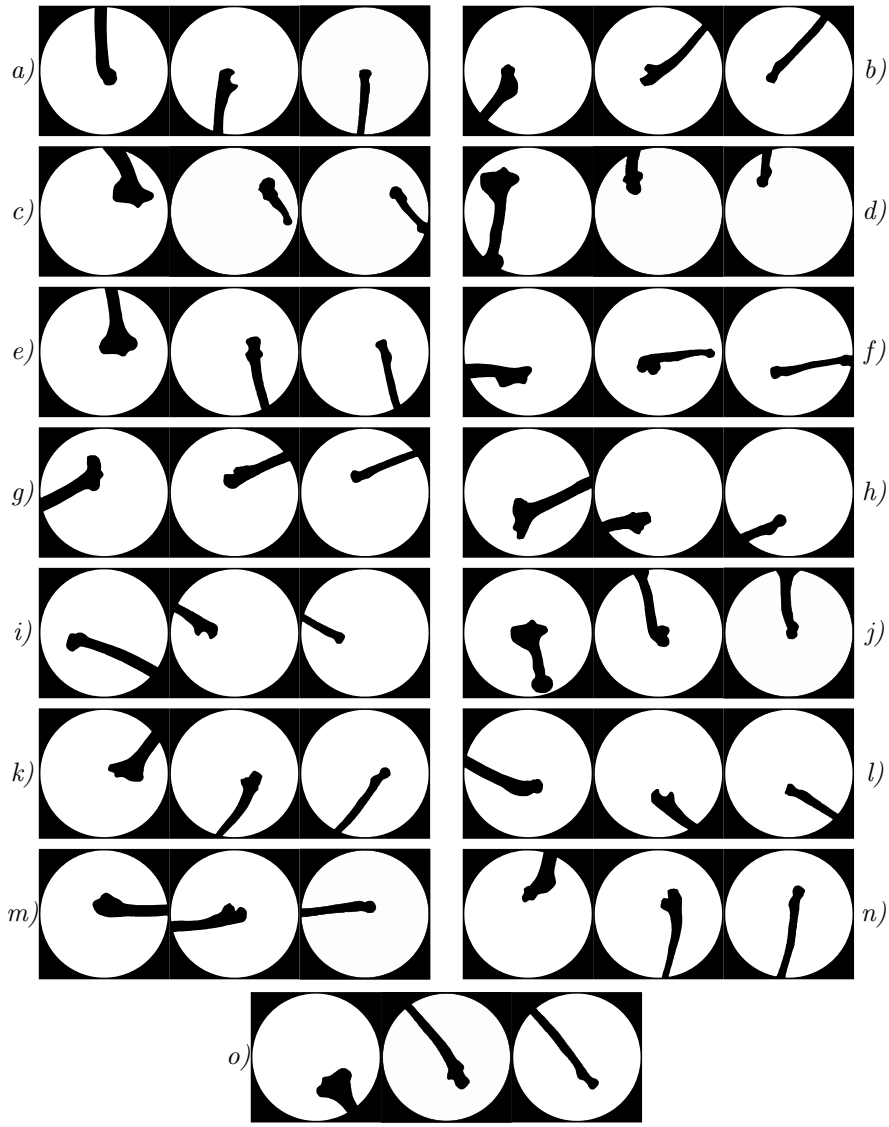

Figure 4.4: Silhouettes of humerus, ulna and radius reference poses for precision test.

a detailed exploration of the convergence domain of the minimization algorithm around different reference poses, in order to quantify and optimize measurement accuracy in terms of bias and precision. In this evaluation study we considered (*a*) the geometric characteristic of the bone models, (*b*) the resolution of the fluoroscopic projection images, (*c*) the resolution of ADM, and (*d*) the convergence properties of the new MA as the only sources of errors.

The MA proved to be extremely robust if compared to the local search algorithm typically used for the pose estimation (see Chapters 2 and 3). With the only exception of the out-of-plane translation, the accuracy of the measurements was in the order of the mm/deg even if the algorithm evolution was completely unsupervised. As testified by the accuracy test, to increase the performance of the method it is better if the searched pose is in the middle of the search domain. This factor will improve the convergence rate and reduce the chance of false pose estimation. In a real acquisition session, it is advisable then to repeat the alignment for the first frame with a large search domain, in order to obtain a good starting point. Then it is possible to propagate the estimated pose as the center of the search domain for the following frame. For these estimations, it is possible to reduce the search domain to increase the performance of the algorithm.

The issue related to the estimation of the translation along the projection axis, remain unsolved because intrinsic to the mono-planar method. The alignment of the radius is characterized by a larger error in the estimation also of the out-of-plane orientations, due to its marked longitudinal cylindrical symmetry.

The work presented here constitute a major advance in the development of the fluoroscopic method. For the first time, the reliability of the new technique will introduce a real reduction of the user interaction. Moreover, the presented results can easily be extended to other 3D fluoroscopic method because it is independent by the metric used for the alignment and by the number of projections.

CHAPTER

FIVE

IN-VITRO QUANTIFICATION OF THE PERFORMANCE OF THE IMPROVED PROCEDURE

5.1 Introduction

The present Chapter describes an *in-vitro* validation of mono- and bi- planar 3D video-fluoroscopy (3DF) for the reconstruction of the joint kinematics through the estimation of joint poses from video-frames sequences.

To validate the proposed methodology, a gold-standard measurement is needed. Roentgen Stereo-photogrammetric Analysis (RSA) is an accurate technique for measuring the three-dimensional position of an object in space using roentgen rays [10]. RSA is currently considered as a radiologic gold-standard, but it cannot be extensively used for clinical evaluations on non-pathological subjects because

Part of the content of this chapter was submitted to:

- **L. Tersi**, A. Barré, S. Fantozzi, R. Stagni,: *In-vitro* validation of monoplanar 3D fluoroscopy with RSA, submitted to *Journal of Biomechanics*.
- **L. Tersi**, A. Barré, S. Fantozzi, K. Aminian, R. Stagni: Quantification of the performance of mono- and bi-planar 3D fluoroscopy compared to marker-based RSA. Submitted to *XXIII congress of ISB 2011*, Brussels, Belgium, July 3-7, 2011.

of its invasiveness.

Although the history of RSA dates back to the invention of X-rays, the broad application of modern RSA started after the development of the roentgen stereophotogrammetry system by Göran Selvik in 1972 in Lund, Sweden [108]. The technique was validated both with static phantom studies and with *in-vivo* test re-test repeatability studies. Bragdon et al. [88] declared for the hip arthroplasty an accuracy of $22-86\ \mu m$ and a precision of $8-14\ \mu m$, and similar results were declared by Önsten et al. [89] and Börlin et al. [109]. The technique was applied to spine pathologies [110], growth [111], joint stability and fractures [112, 113], but mainly to study prosthesis migration in total joint arthroplasty [34, 114, 115].

Spherical tantalum markers are used almost exclusively to serve as well-defined landmarks. They are inserted into bone and may be attached to implants to form a cluster. The position and the orientation of the cluster could be defined given 2 radiographic projections in a calibrated system and triangulating the positions of the labeled markers. Standard markers have diameters of 0.5, 0.8 and 1.0 mm, affecting the precision of measurements. Larger markers result in a larger X-ray image; this larger projection in turn holds more information, which results in higher precision. But they also have a less well defined contour and a less well defined profile, because the marker image is the result of a central projection with an X-ray source of a definite size [35]. At least 3 non-collinear markers should be used to mark each rigid body under study. However, because of the fact that markers can be obscured by metal objects, and a redundancy of markers will increase the precision of the measurements, Valstar et al. [35] advise to use about 6-9 well-scattered bone markers for each bony structure. Nonetheless, due to manufacturing issues, the number of prosthesis markers is kept to a minimum: in most instances 3 markers are attached. Markers should not be obscured by the metal of the prosthesis, and in order to avoid galvanic corrosion the markers should not be in contact with the prosthesis.

In addition to static analysis, RSA has also been used to assess joint kinematics dynamically. The first study on knee joint kinematics was initiated as early as 1979, but was performed on cadaver specimens [116]. The technique was then applied to the study of anterior cruciate ligament reconstruction [117] and to the comparison of Total Knee Replacement (TKR) kinematics with normal knee patterns [15, 36].

Nevertheless, the errors committed in static analysis worsen when propagated

to dynamically estimation of joint kinematics [118]. The validity of the RSA applied to joints in motion was tested by De Lange et al. in 1990 [119], finding out that the accuracy strictly depends on the number and the distribution of the markers on the bone or prosthesis surface.

One of the major disadvantages of RSA is that implants manufactured with special markers drastically increases cost and extends study planning. The modified implant is essentially a different implant from the device that will be widely distributed. Marking the implant may also jeopardize its strength and cause local stress raisers in the bone cement. This can result in cement cracks, which compromise fixation strength. Because the markers are attached to the implant they are often over-projected by the implant. Moreover, being based on markers implant, for obvious ethical reasons, RSA cannot be applied to the study of the intact joints kinematics. Another invasiveness issue is determined by the high X-ray dose for the analyzed subject. The small size of the tantalum beads implies the acquisition of double projections using traditional high dose radiography, and this may become a limiting factor of the allowable duration of dynamic analysis.

To circumvent these problems, since the middle of the nineties, different model-based protocols were proposed in contrast to the marker-based RSA [11, 72]. An invasiveness reduction was introduced by the use of mono-planar methods [12]. The accuracy of mono-planar 3DF was previously investigated. For total knee replacement kinematics, an accuracy level of the order of mm/deg was reported [3, 12, 13, 99], but major problems were encountered to estimate the translation along the projection axis (accuracy approximately one order of magnitude lower). More recently Acker et al. [19, 120] reported the accuracy of a fluoroscopic approach specifically in determining the relative pose between the femoral and tibial prosthesis components along knee motion axes, while the components were in motion relative to one another. The registration algorithm proposed by Mahfouz et al. [13] was used for the optimized pose of the prosthesis components during dynamic trials. The limits of agreement, between which 95% of differences can be expected to fall, were -2.9 to 4.5 deg in flexion, -0.9 to 1.5 deg in abduction, -2.4 to 2.1 deg in external rotation, -2.0 to 3.9 mm in anterior-posterior translation, -2.2 to 0.4 mm in distal-proximal translation and -7.2 to 8.6 mm in medial-lateral translation.

A part than applications on joint prostheses, 3DF has been also applied to intact joints. The accuracy estimated for TKR kinematics cannot be a-priori be considered valid in general for intact joints, due to the low quality of images

and joint models. Fregly et al. [17] proposed an *in-silico* evaluation of 3DF for the analysis of natural knee absolute pose, declaring a slightly worse accuracy ($\simeq 2\ mm, \simeq 3\ deg$) even if in computer simulations, many fluoroscopic errors were disregarded. The less contrasted nature of the fluoroscopic projections and the marked morphologic symmetries interfered with a proper alignment.

Especially for intact joint analyses, the reduction of information introduced by the mono-planar fluoroscopy can affect the accuracy and reliability of the technique. On the other hand, these validation studies were carried out considering different setups, softwares, 2D-3D registration algorithms, and testing different prostheses or joints models. The provided results may then not be comparable to each other. It is necessary to provide a comparison of the kinematics estimations performed on the same datasets with mono- and bi- planar 3DF and with a gold-standard. In Section 2.2, a preliminary *in-silico* comparison of mono- and bi-planar techniques applied to prosthesis models was proposed. Investigating only a small domain ($\pm 4\ mm/deg$) around a reference pose, both mono- and bi-planar achieved excellent results in the pose estimation ($\simeq 0.1\ mm/deg$), but $\simeq 2\ mm$ for the mono-planar out-of-plane translation. Many sources of error typical of real fluoroscopic sessions were disregarded and further investigations were needed.

Moreover, due to the discussed limitation of the optimization algorithms (Chapter 4), the automatic 2D-3D registration were only used to refine previous time consuming manual alignments [19]. Without quantifying the intra- and inter-rater reliability, it was not clarified how the user experience may affect the results. In this Chapter a novel *in-vitro* study will then be presented to evaluate the robust registration algorithm based on Memetic Algorithm (MA) and described in Chapter 4. Being robust and non-dependent by the user, it is not necessary to evaluate the intra- and inter-rater reliability of this novel method, and the provided results will be more generalizable than those of previous studies.

The objectives of the current work are the validation of 3DF for the quantification of intact knee kinematics, and the concomitant comparison of mono-planar and bi-planar techniques. Mono- and bi-planar 3DF were then applied to knee phantom kinematics, considering marker based RSA as a gold-standard.

5.2 Material and methods

5.2.1 Data acquisition

A Sawbones™[121] composite bone model of the knee joint (composed by tibia and femur) was used for the validation study. Images of five repetitions of 10 s simulated walking tasks were acquired with two synchronized fluoroscopes BV Pulsera (Philips Medical Systems) at a frame rate of 30 fps. An home made synchronization device was developed and used for the acquisitions. The projection axis of the two fluoroscopes were coplanar with an angle of approximately 50 deg [122] (Figure 5.2). Images of calibration devices were acquired and used for the distortion correction, and foci and spacing calibration [60], but also to accurately determine the pose of each fluoroscope in the global reference frame.

Four tantalum beads with a diameter of 1 mm were implanted on each segment for the RSA analysis. Surface mesh models of the Sawbones™knee segments were generated from Computer Tomography (CT) scans (Lightspeed VCT, GE Medical Systems). Due to the absence of soft tissue, a simple thresholding was used for the segmentation purpose (Figure 5.1). Using virtual palpation, anatomical landmarks were identified and used to define anatomical reference frames according to International Society of Biomechanics (ISB) [123], but due to absence of the fibula in the model, the reference frame definition of Conti et al. [124] was used for the tibia. The relevant relative positions of the tantalum beads clusters were also reconstructed from the CT scan. For each mesh model an Adaptive Distance Map (ADM) with a resolution of 0.5 mm was computed and stored.

5.2.2 Pose estimation algorithms

The alignment algorithm implemented was described in chapters 1 and 4, but adapted to bi-planar analysis. The fluoroscopes were represented by two perspective projection models. A global system of reference was defined with the x and y axis in the image plane of the one fluoroscope (F1), and the z axis perpendicular to the image pointing towards the X-ray source, forming a right-hand reference frame. The position and the orientation of the second fluoroscope (F2) was estimated with the acquisition of calibration devices.

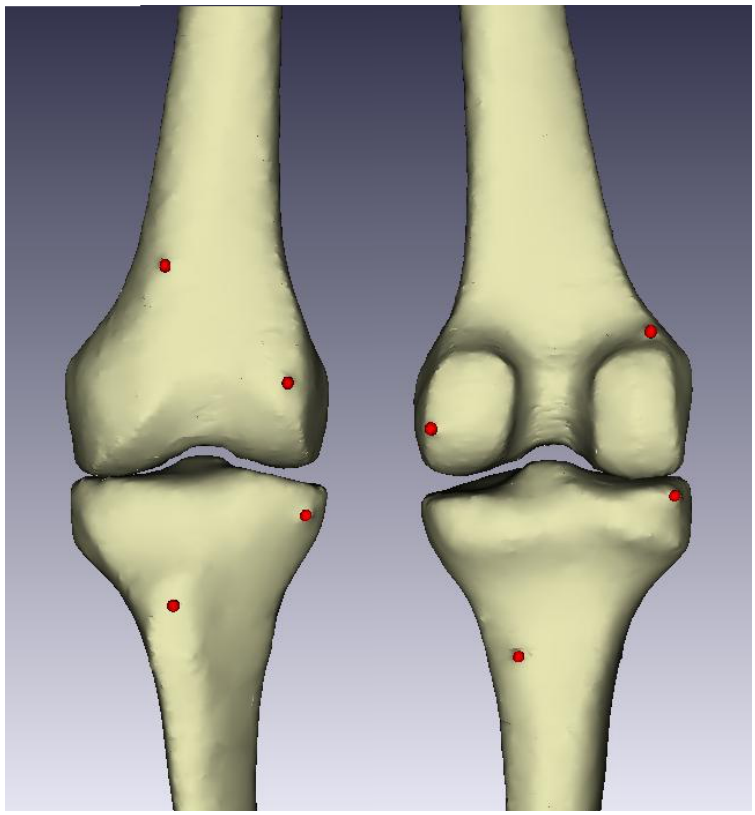

Figure 5.1: Frontal and back views of the CT segmentations of the Sawbones™phantom models of tibia and femur with the relative cluster of markers for the RSA.

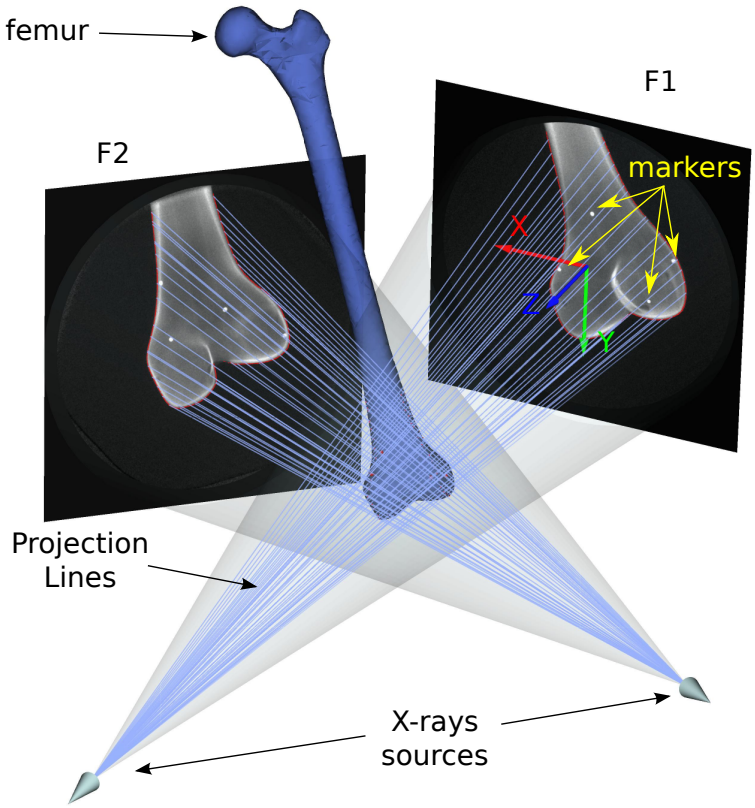

Figure 5.2: Virtual representation of the system, the femur model is tangent to the projection rays connecting the contours in the image and the X-rays source. The markers in the image are used for the RSA elaborations.

3D video-fluoroscopy

Each task repetition was analyzed using both (bi-planar) or only one of the fluoroscopic projections (F1 or F2). The pose was estimated minimizing the Euclidean Root Mean Square Distance (RMSD) between each surface model and the beams of lines connecting the X-ray sources and the edges of the bone extracted in the projected images. Differently from what described in section 1.3.1, for the bi-planar setup, the RMSD was computed considering both the beams of projecting lines of the two fluoroscopes. The optimization algorithm was a completely unsupervised MA (chapter 4). Briefly, each Degree Of Freedom (DOF) was coded with an 18 *bit* Gray code [106], an initial population of 100 chromosomes (poses) evolved to convergence using multipoint crossover, ageing, mutation and Lamarckian learning operators. For the first frame, as suggested in Chapter 4, the initial population was made of 100 chromosomes uniformly distributed spanning the entire Field Of View (FOV) domain (± 100 *mm* for translation, and ± 180 *deg* for rotations). In order to increase the computational performance and the reliability of the estimates, for the following frames, the search domain was centered in the optimal pose estimated for the previous frame and the domain extent was reduced to ± 50 *mm* for translation, and ± 50 *deg* for rotations. Moreover, if the RMSD of the estimated optimal pose was at least 3 times larger than the residual of the previous pose, the alignment was automatically repeated.

The contours for the alignments were semi-automatically generated using a hybrid region growing and Malladi-Sethian level-set method [125] (see Chapter 6), which was designed for prosthesis segmentation but was feasible for this phantom study due to the absence of soft tissues that, in *in-vivo* condition, do not allow automatic contours extraction.

Roentgen Stereo-photogrammetric Analysis

The coordinates of each marker in the image planes were obtained with a Hough transform [126] and manually labeled in the first frame. The labeling was then automatically propagated to the nearest neighbors on the following frames for the whole dataset. The RSA 3D kinematics was computed using the method described by Valstar et al. in [127]. The reconstruction of the 3D reference position of each marker is the linear algebra problem of computing the closest point in the space between two skewed projection lines connecting the X-ray sources and the labeled points in the fluoroscopic images.

Having n markers on a rigid segment, let $\underline{a}_1, \ldots, \underline{a}_n$ be the coordinates of the markers in the anatomical reference frame, and $\underline{g}_1, \ldots, \underline{g}_n$ be the reference markers coordinates in the global reference frame. To estimate the pose of the segment, the rotation matrix M and the translation vector $\underline{d}$ must be assessed solving the following equation:

$$\min_{M,d} \sum_{i=1}^{n} \left\| M\underline{a}_i + \underline{d} - \underline{g}_i \right\|^2 \tag{5.1}$$

so that M is an orthogonal matrix.

This problem can be solved using the matrix singular value decomposition [128, 129]. The translation vector $\underline{d}$ can be expressed as:

$$\underline{d} = \frac{1}{n} \sum_{i=1}^{n} \left(\underline{g}_i - M\underline{a}_i \right) = \overline{g} - M\overline{a} \tag{5.2}$$

Substituting this expression in 5.1, the only unknown remains M:

$$\min_{M} \sum_{i=1}^{n} \left\| M(\underline{a}_i - \overline{a}) - (\underline{g}_i - \overline{g}) \right\|^2 \tag{5.3}$$

When we define $A = [\underline{a}_1 - \overline{a}, \ldots, \underline{a}_n - \overline{a}]$ and $G = [\underline{g}_1 - \overline{g}, \ldots, \underline{g}_n - \overline{g}]$, the problem may be written as:

$$\min_{M} \|MA - G\| \tag{5.4}$$

so that M is an orthogonal matrix. The solution of the rotation matrix is:

$$M = UV^t \tag{5.5}$$

in which

$$GA^t = U\Sigma V^t \tag{5.6}$$

is the singular value decomposition. The problem can be ill conditioned for small number of markers, and the reflection matrix ($\det(M) = -1$) can be erroneously

estimated. To solve this problem, Equation 5.5 is modified as follow [130]:

$$M = U \begin{bmatrix} 1 & 0 & 0 \\ 0 & 1 & 0 \\ 0 & 0 & \det(UV^t) \end{bmatrix} V^t \tag{5.7}$$

The solution of $\underline{d}$ is found when M is substituted in Equation 5.2.

The frames with less than three couple of visible markers were excluded from the analysis because the problem would degenerate.

5.2.3 Data reduction

For each data frame ($\sim$ 1500 frames), the deviation from the gold-standard kinematics of each estimated DOF was quantified as:

$$diff^i = \underline{p}^i_f - \underline{p}^i_{gs} \tag{5.8}$$

where $\underline{p}^i = [T^i_x, T^i_y, T^i_z, \Theta^i_x, \Theta^i_y, \Theta^i_z]$ is the pose vector for the i-th frame estimated with the fluoroscopic methods (f) and the gold-standard RSA (gs).

The Kolmogorov-Smirnov test was used to investigate whether the error distributions were normal. The trial and the bone model effects were evaluated with a Kruskal-Wallis test ($\alpha = 0.05$). The accuracy and precision of the estimate were expressed as the median (m) and interquartile range (iqr) of the distributions. The agreement between the RSA and fluoroscopic results was also described by the Bland-Altman "limits of agreement" approach [131], and adapted to non-normal distributions [132]. This method defines the upper and lower limits, between which 95% differences between the two methods can be expected to fall, and plots the differences ($diff$) between the gold-standard and estimated measurements (Equation 5.8) against the means of the two measurements (Equation 5.9).

$$mean^i = \frac{1}{2}(\underline{p}^i_f + \underline{p}^i_{gs}) \tag{5.9}$$

All statistical analyses were performed with NCSS (NCSS, Kaysville, USA).

Table 5.1: Pose estimation error relative to the comparison of the kinematic quantifications carried out considering the mono-planar projection of the fluoroscope 1, of the fluoroscope 2, and the bi-planar projection with the RSA gold-standard. Median m and interquartile range iqr of the error distributions are reported.

DOF	mono F1		mono F2		bi-planar	
	m	iqr	m	iqr	m	iqr
T_x $[mm]$	0.1	0.3	-1.4	1.2	0.1	0.3
T_y $[mm]$	~ 0	0.4	-0.6	0.4	~ 0	0.1
T_z $[mm]$	3.1	4.9	1.5	1.0	0.2	0.2
Θ_x $[deg]$	1.2	1.3	0.4	0.4	0.1	0.2
Θ_y $[deg]$	-0.3	1.1	-0.2	0.6	-0.2	0.4
Θ_z $[deg]$	~ 0	0.2	-0.2	0.4	0.1	0.1

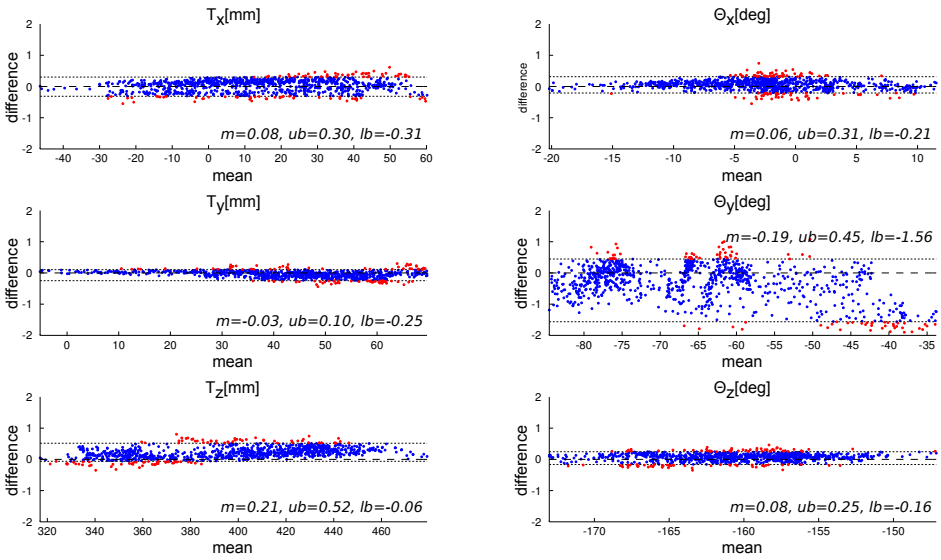

Figure 5.3: Bland-Altman plots for the evaluation of the agreement between RSA and bi-planar 3DF.

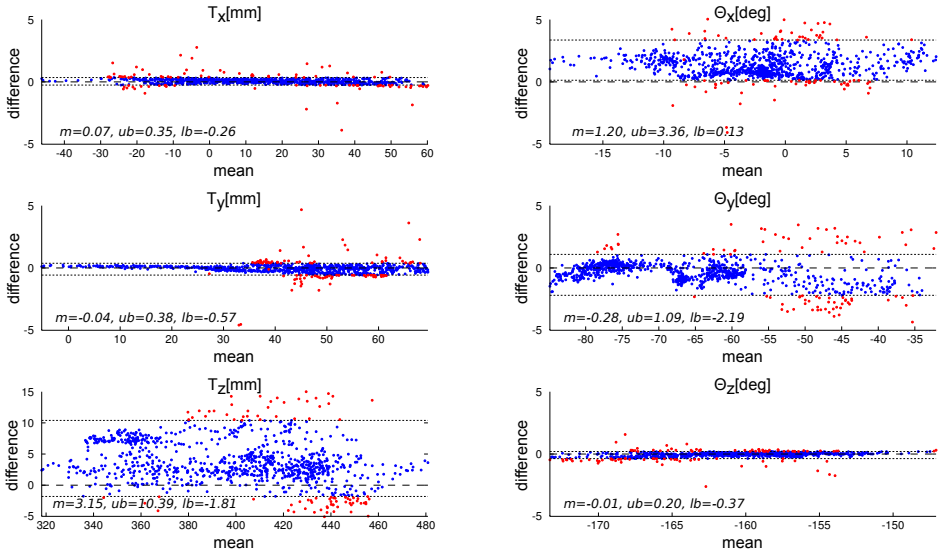

(a) F1

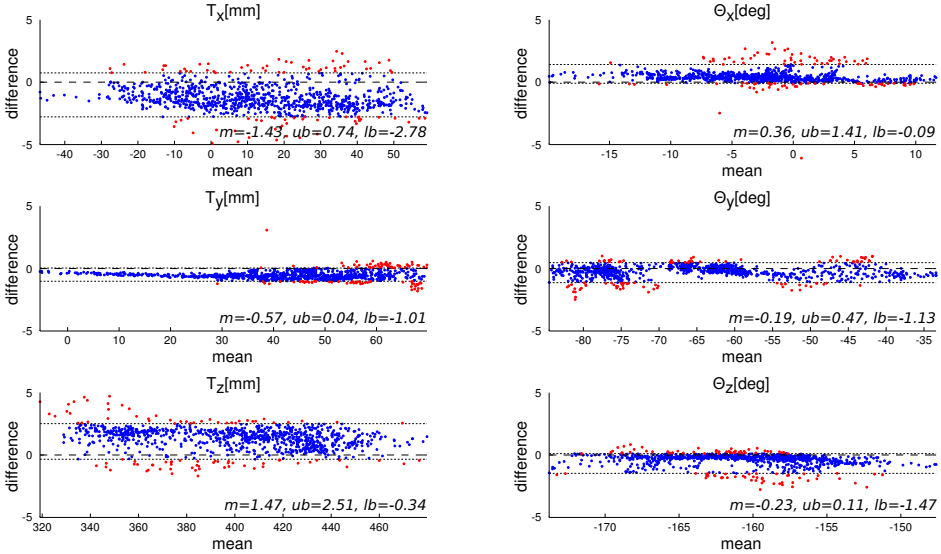

(b) F2

Figure 5.4: Bland-Altman plots for the evaluation of the agreement between RSA and F1 and F2 mono-planar 3DF.

5.3 Results

About 20% of the frames were excluded from the analysis because not all the tantalum markers necessary for the RSA pose reconstruction were visible inside the FOV. The differences in the alignments of the mono-planar and the bi-planar analysis compared to the RSA gold-standard were quantified. Similar results were obtained both for the femur and for the tibia, moreover no significant differences were obtained among the repetitions (Kruskal-Wallis, $P > 0.05$). All the data were then analyzed together and the results are reported in Table 5.1.

5.3.1 Bi-planar

The Bland-Altman plot shows the median and the upper and lower limits of agreement (upper and lower dotted lines) are the bounds between which 95% of the differences between the two methods can be expected to fall. For the bi-planar alignment (Figure 5.3), the translation error was in the order of magnitude of the lower bound determined by the fluoroscopic image pixel spacing (equal to 0.3 mm as quantified with the calibration process) with the worst iqr for the translation in the x direction (0.3 mm). A positive bias was found for T_z ($m = 0.21$ mm, lower and upper bounds 0.06/0.52 deg). Unbiased results were obtained for rotations, with the worst case for the estimation of the rotation around the bones longitudinal y axis ($m = -0.19$ deg, lower and upper bounds $-1.56/0.45$ deg). No linear trends was highlighted.

5.3.2 Mono-planar

Two different mono-planar alignments were carried out considering each of the two fluoroscopes. No linear trends was highlighted by the Bland-Altman analyses. For F1 (Figure 5.4a), unbiased results were obtained for the in plane pose parameters (T_x, T_y, Θ_z). In this configuration, the out of plane translation (T_z) is the most critical with $iqr \simeq 5$ mm; the out-of-plane rotation (Θ_x) is biased and with a relatively large dispersion ($iqr = 1.3$ deg). For the fluoroscope F2 (Figure 5.4b) the error was spread among the DOFs with the largest dispersion for T_x with $iqr = 1.2$ deg. The T_z positive bias was found also for both the mono-planar alignments.

5.4 Discussion

Due to the small dimension of the bi-planar setup investigation volume, about 20% of the frames were excluded from the validation analysis, because not all the tantalum markers necessary for the RSA pose reconstruction were visible inside the FOV. The model-based bi-planar method, however, provided accurate analyses of these frames, because it managed to combine the lacking information on one fluoroscope, with the second projection, proving to be more robust than the mono-planar techniques. On the other hand, in order to be analyzed at the same time both with bi-planar and mono-planar methods, the acquired volume for the task was designed considering the limited intersection between the two X-rays beams of the two fluoroscopes (see Figure 1.1). In a merely mono-planar setup, the motion task could exploit a bigger acquisition volume, and then reduce the chances of exiting from the FOV.

For the bi-planar alignment, excellent results were obtained: the translation error was in the order of magnitude of the lower bound determined by the fluoroscopic image pixel spacing with the worst *iqr* for the translation in the x direction (0.3 mm). The most problematic DOF was the rotation around the bones longitudinal y axis, but this result was expected due to the longitudinal cylindrical symmetries of the long bones analyzed.

The orientation of the global reference frame with respect to the direction of the projection of the two fluoroscopes, had an effect on the results. The 50 deg angle on the xz plane, was chosen in order to maximize the investigable volume in one direction, to be aligned with the sagittal direction of the walking task [122]. In this configuration, F1 is aligned to the reference frame, and the out of plane translation (T_z) is the most critical with $iqr \simeq 5\ mm$, and, differently from the bi-planar alignment, the error related to the out-of-plane rotation (Θ_x) is dominant over the inter-intra rotation error (Θ_y). The fluoroscope F2 was not aligned with global reference frame, thus the error was not condensed in the estimation of T_z but spread among the DOFs. In particular, the uncertainty of the translation along the projection axis, was projected and split along the x and z direction.

5.5 Conclusions

The objectives of the current work was the *in-vitro* validation of 3DF for the quantification of intact knee kinematics, and the concomitant comparison of mono-planar and bi-planar techniques. Mono- and bi-planar 3DF were then applied to knee phantom kinematics, considering marker based RSA as a gold-standard.

The bi-planar alignment proved to be extremely accurate and precise, but it is limited by the significant reduction of the investigable volume. The present setup, with an angle between the two fluoroscopes of 50 *deg*, was optimized for a treadmill walking task, because differently from an orthogonal setup, the investigable volume has a dominant direction which is aligned to the walking direction. When a bone is projected at the border of the FOV, the mono-planar reliability is limited, while the bi-planar manages to obtain accurate results exploiting the information of the second fluoroscope. The bi-planar reliability is then best suited for research purposes, that usually need excellent accuracy and for which the analysis costs and the elaboration time are not major issues. Nonetheless, the mono-planar setup has halved costs, halved analysis time and halved ionizing radiation dose for the patient. In a clinical environment, the trade-off between analysis costs and quality becomes a major constraint. Notwithstanding its accuracy limitations, we can finally conclude that the reliability of the mono-planar alignment can be sufficient for clinical analysis. To this aim, the acquired motion tasks must be designed in a way that the clinically significant information are not gathered in the out-of-plane direction.

CHAPTER

SIX

AUTOMATION OF THE SEGMENTATION PROCEDURE: APPLICATION TO PROSTHETIC COMPONENTS

This study was carried out in collaboration with
MEng. Giacomo Tarroni, Ph.D. Student in Bioengineering, XXIV cycle

6.1 Introduction

3D video-fluoroscopy (3DF) was proven to be a reliable and accurate method to study *in-vivo* joint kinematics (see chapters 4 and 5). However, the data analysis is cumbersome and time consuming and major concerns are raised regarding its possible use in a clinical environment. There are mainly two bottlenecks in the elaboration process for fluoroscopic data investigation: (*a*) the information

Part of the material described in this chapter will be submitted to:

- G. Tarroni, **L. Tersi**, C. Corsi, R. Stagni: A Fast and Automated Method for the Segmentation of Prosthetic Components in 3D Fluoroscopy, to be submitted to *IEEE Transaction on Biomedical Engineering*.

and was submitted to:

- **L. Tersi**, G. Tarroni, C. Corsi, R. Stagni: Automatic prosthesis segmentation in 3D fluoroscopy. In: proceedings *International Computer Vision Summer School, ICVSS 2010*, Sicily, Italy, July 12-18, 2010

retrieval in fluoroscopic images to be exploited for the 2D-3D registration, and (*b*) the manual alignment of the 3D model in order to provide the optimization algorithm with a proper initial guess. Solutions for the latter issue were discussed in chapter 4, and consisted in the design of a robust Memetic Algorithm (MA) independent from the initial guess for the pose optimization. On the other hand, the information retrieval still remains a challenging problem. Many fluoroscopic methods, such as the one investigated in the present study [3, 11] or the methods proposed by Banks et. al [12] and by Kaptein et al. [14, 133], rely on the accurate contour extraction in the fluoroscopic frames. The contour must be an exact segmentation of the structure of interest, and must avoid perturbation caused by soft tissue, bones, prosthesis or contralateral limb overlapping. To get this contour, a Canny edge detector [70] is typically applied to the whole image or to a smaller region of interest, but a time consuming manual procedure is needed to delete the undesired contours belonging to other anatomical structures. Commercial softwares, such as MBRSA of Medis Special (Leiden, The Netherlands), provide this solution.

To avoid this manual operation, Mahfouz et al. [13] proposed a contour matching method that does not need manual contour suppression. Informations related to spurious contours, however, interfere with a proper alignment. Bey et al. [74] proposed a method based on Digitally Reconstructed Radiography (DRR) to quantify the entity of the alignment in term of similarity between the real and the reconstructed fluoroscopic images. The DRR method uses not only the information about the silhouette of the segment but also information about the internal image gray levels. However, this technique can only be applied to intact joints and not to prosthetic components. Moreover, for both the approaches, it is still not clear whether the increase of information will improve the quality of the alignment or, on the other hand, will interfere with the optimization algorithm introducing local optima in the process.

Another possible solution to reduce the user interaction is the automation of the contour extraction. The automatic contour extraction is not feasible for intact joints, because the gray levels of the bones and of the surrounding anatomical structures are similar, and more importantly, it is not possible to discriminate between the necessary external and the spurious internal contours. On the other hand, it is possible to automate the contour extraction for prostheses, because their radiographic projections are highly contrasted. Oprea et al. [134] investigated the use of several classical adaptive region segmentation techniques, using

either the initial pixel luminance space (adaptive histogram thresholding), or an extended feature space (Fuzzy C-Means). The methods were applied to traditional radiographies of hip prostheses of static limbs, thus to better quality images as compared to the fluoroscopic ones. Moreover, even the best method (Fuzzy C-Means) provided a false positive pixels classification rate of $2 - 11\%$ which may be propagated as large errors to the pose estimation. Domokos et al. [135] proposed a template matching method for radiographic hip prosthesis segmentation. However the quality of the method was affected by illumination variations which is quite common in fluoroscopic images. Moreover, being based on template matching, the technique models the projective transformation of the prosthesis, which depends on the pose of the implant in 3D space, with a 2D affine transformation. The affine assumption, however, is valid only if the X-ray images are taken in a well defined standard position of the limb [135]. On the other hand, template matching methods cannot be used in kinematics estimation algorithm because these methods use a-priori knowledge about the shape of the prosthesis to be segmented which, in the 3DF context, is the unknown quantity to be estimated.

The quality of fluoroscopic images of prostheses is frequently affected (a) by image blurring, (b) by the presence of dark cemented region closed to prosthesis border, and (c) by the cluttering of other prosthetic components or of the contralateral limb. These, together with the fact that the prostheses projection shapes are mixture of round and sharp contours, constitute interfering factors that must be taken in consideration to design the segmentation methods, and prevent traditional techniques such as active contours, level-set or region growing to be effective. On the other hand, combining the strong points of these methods can be enough to develop a robust segmentation algorithm to be applied in the dynamic context of 3DF and to reduce the user interaction in the contour selection. Varshney et al. [136] followed this approach, developing a multi-view segmentation method where an active contours 3D surface evolution with level-set implementation is used to recover the shape of bones and prostheses in postoperative joints, getting promising results in a 3D shape recovering task.

The aim of the present work is then to speed up the prostheses contour extraction and to reduce the human interaction in the fluoroscopic analysis, through the development of a fast and robust semi-automated prostheses segmentation method, combining region growing and level-set methods.

6.2 Material and Methods

Well-known segmentation algorithms were combined together in order to develop a novel methodology with tuned characteristics specific for the application to the prostheses segmentation in fluoroscopic images. Design criteria included:

- *velocity*: reduced user interaction time;
- *flexibility*: in order to be applied to different prosthetic models;
- *accuracy*: few accurate contour points are better than many but wrong;
- *robustness*: ability to deal with blurred images, low contrast, and presence of illumination gradient;
- *specificity*: the algorithm should be able to discriminate prosthesis edge from cemented parts or high density bony tissue.

The fluoroscopic dataset is typically a series of 1024x1024 pixels images following the DICOM standard, acquired at $5 - 50$ fps. In a normal setup a 512x512 side square is enough to contain the prosthesis projection. Depending on the technology, 10 or 12 bits per pixel are reserved to code the gray tone, resulting in 1024 or 4096 levels. The Field Of View (FOV) may correspond to a circle with a diameter of about $20 - 40$ cm, thus it could easily happen that the prosthesis overlaps with the FOV border. If not acquired with modern flat-panels, fluoroscopic images are geometrically distorted. In this work we analyzed undistorted images, because, as discussed in section 2.3, effective procedures to compensate for the distortion were implemented [60]. To improve the quality of the image, also the vignetting compensation can be applied (section 1.2.1).

6.2.1 Segmentation algorithm

The algorithm is applied to each prosthesis component, and is briefly implemented as follow:

1. seeding and cropping;
2. level-set edge preserving anisotropic diffusion filter [137];
3. binary mask based on thresholding and morphology-based operations on an edge indicator g (Equation 6.3);

4. region growing [138];

5. contour refining with Malladi-Sethian [125];

6. automatic inaccurate contour suppression.

1. Seeding Giving the fact that the prosthesis dimension is limited as compared to the full extent of the image, the first operation is to identify a region of interest containing the whole prosthesis projection. This is done with a manual seeding operation, on an internal point approximately at the center of the prosthesis component. The image is then cropped to a square, the side of which is a power of 2 pixels wide (usually 512). This is necessary for the following region growing operation.

2. Diffusion filter To reduce the effect of the Poisson noise [139] typical of fluoroscopic images, and to make the prosthesis gray level as uniform as possible throughout the whole prosthesis extent, without losing information about its edges, a level-set edge preserving anisotropic diffusion filter was designed and applied to the image I:

$$\begin{cases} I_t = gK|\nabla I| + \nabla g \cdot \nabla I & \text{in } \Omega \times]0, \inf[\\ \frac{\partial I}{\partial n} = 0 & \text{in } \partial\Omega \times]0, \inf[\\ I(0) = I_0 & \text{in } \Omega \end{cases} \tag{6.1}$$

where I is the image, Ω is the image domain, K is the curvature

$$K = \nabla \cdot \frac{\nabla I}{|\nabla I|} \tag{6.2}$$

and g is an edge indicator controlled by the parameter β and defined as follow:

$$g = \frac{1}{1 + |\nabla I/\beta|} \tag{6.3}$$

The diffusion of the level-set is weighted by the edge indicator, it is then fast in the low gradient area, but it slows down and stops in correspondence of the edges. Equation 6.1 is approximated with a finite-difference scheme and solved iteratively (100 iteration per image).

3. Binary mask A binary mask is then computed thresholding the edge indicator g applied to the filtered image. This operation is carried out in order to obtain a uniform and closed white region inside the prosthesis area. To assure that the area is closed, a manual check of the threshold T is needed:

$$g_{max} = \max_{i,j}(g_{i,j}) \qquad \text{with} \quad i,j \in \Omega \tag{6.4}$$

$$g_{i,j}^{mask} = \begin{cases} 0, & if\ g_{i,j} < T g_{max} \\ 1, & if\ \ g_{i,j} > T g_{max} \end{cases} \qquad \text{with} \quad T \in [0,1] \tag{6.5}$$

To clean the spurious contours inside the prosthesis area a *fill holes* procedure is finally applied to g_{mask}. A hole is a set of background pixels that cannot be reached by filling in the background from the edge of the image. The result is a binary image, white in the uniform gray level area, and black in proximity of the edges (see Figure 6.2).

4. Region growing The resulting image is then elaborated with a region growing algorithm [138]. Region growing is a simple region-based image segmentation method. It is also classified as a pixel-based image segmentation method since it involves the selection of initial seed points. This approach examines neighboring pixels of initial seed points and determines whether the pixel neighbors should be added to the region. In the present implementation, the process started from the seed point specified in step 1, which was also used for cropping purpose. To avoid eventual overflow outside the prosthesis region, an 8-connected neighborhood criteria was used for the classification. The result is a binary image, white inside the seeded prosthesis, and black outside. It is now possible to extrapolate a contour as an iso-curve between the black and white pixels.

5. Malladi-Sethian The contour obtained with the region growing is closed and a shrunk version of the actual prosthesis contour. The previous thresholding operation are meant to get a first guess contour as close as possible to the prosthesis edge, but the thresholding of the edge detector g tends to widen the prosthesis border, both towards the inside and the outside of the prosthesis. Starting from an inside seed, the region growing detects the internal side of this border, which is certainly shrunk.

A final refining operation is then needed to evolve the extracted contour to the actual one. This is carried out with a Malladi-Sethian level-set algorithm [125], based on Equation 6.1, but in which the implicit surface to be evolved is a distance function of the contours point. The metric of the evolution is weighted by the edge indicator g applied to the original image I (Equation 6.3).

The procedure is iterated, and automatically stopped when the area inside the contours does not change of more than 4 pixels between two following iterations.

6. Contour suppression (CS) Image blurring is one of the major source of error (see chapter 5). The blurring is typically due to a motion of the analyzed limb, and is thus directional. This means that only the contours that are orthogonal to the motion vector of the limb will be affected by blurring. In 3DF it is then better to rely on few accurate contours than on many blurred contours. An automated procedure was then developed to find out whether the extracted points belong to a blurred or to an un-blurred contour. The gradient ($grad$) of the image is computed and convolved with a smoothing Gaussian function obtaining $grad^s$. The point of the contour at coordinates (i, j) is suppressed if the value of the correspondent pixel in the smoothed gradient is lower than a certain threshold ($grad^s_{i,j} < th$).

6.2.2 Performances evaluation

The performances of the algorithm were analyzed both with *in-silico* simulations and with the analysis of *in-vivo* real data.

In-silico

CAD models of the femur and tibial knee prosthesis components, and of the stem of a hip prosthesis [140], were virtually aligned over real fluoroscopic images of intact knees and hips. Considering the Lambert-Beer law (Equation 1.1), DRRs were generated and fused with the real images simulating different conditions of blurring and light gradient. The fusion was carried out using the following procedure:

1. The model was positioned in 10 physiological positions aligned to the underlying images.

2. Flat shaded binary projections were generated. The iso-lines at the edge between black and white pixels were extracted and used as gold-standard contours.

3. The binary images were then blurred in a random direction of $blur = 0, 5, 10\ pixels$.

4. A Poisson noise was added to the image according to [139].

5. A radial light gradient was added to the image simulating the vignetting effect (see section 1.2.1); the intensity of the gradient was varied in three levels $vig = 0, 5, 10$ % of the real image gray level range.

6. The resulting image was finally merged to the real fluoroscopic image to simulate the texture caused by soft tissues.

The algorithm was then applied to the to the resulting 270 perturbed image. The accuracy of the segmentation was evaluated computing the Hausdorff distance [141] between the extracted contours and the relevant gold-standards. Two sets are close in the Hausdorff distance if every point of either set is close to some point of the other set. The Hausdorff distance is the longest distance you can be forced to travel by an adversary who chooses a point in one of the two sets, from where you then must travel to the other set. In other words, it is the furthest point of a set that you can be to the closest point of a different set. Let R be the set of points r of the reference gold-standard contour, and E the set of points e of the estimated contour, we define:

$$H_{re}(R, E) = \max_{r \in R} d(r, E) \tag{6.6}$$

$$H_{er}(R, E) = \max_{e \in E} d(e, R) \tag{6.7}$$

where

$$d(u, V) = \min_{v \in V} \sqrt{(u_x - v_x)^2 + (u_y - v_y)^2} \tag{6.8}$$

is the minimum Euclidean distance between the single point u and the set of points V. Thus, the Hausdorff distance is:

$$H(R, E) = \max \{H_{re}, H_{er}\} \tag{6.9}$$

The Hausdorff distance is defined for closed curves, however, when the contour suppression is applied ($CS = 1$), the procedure ends up with open curves. We need then to compare a reference closed curve (in red in Figure 6.1b), with an estimated opened contour. In these cases, only H_{er} (Equation 6.6) will be use to compare the results, because H_{re} may overestimate the actual contour distance.

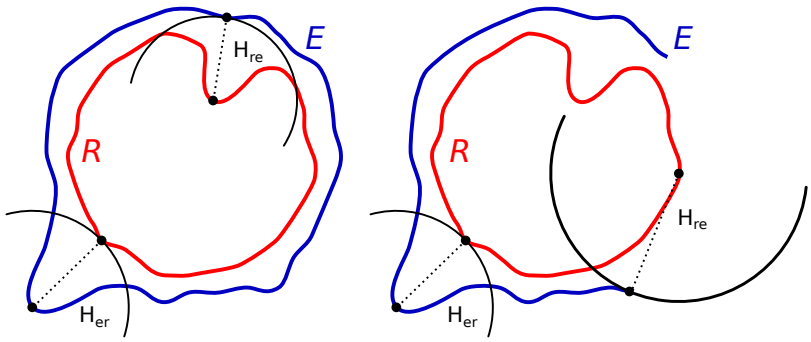

(a) Closed curves **(b)** Opened curves

Figure 6.1: Outline of the Hausdorff distance for closed (6.1a), and opened (6.1b) curves. H_{re} is not a suitable measure of the distance between the opened curves because it overestimates the actual distance.

The Hausdorff distance quantifies the maximum discrepancy among the contours and constitutes then an upper limit of the error. To quantify the average error the Mean Absolute Deviation (MAD) [142] was also estimated according to the following equation:

$$MAD(R,E) = \frac{1}{2}\left(\frac{1}{N_r}\sum_{r\in R} d(r,E) + \frac{1}{N_e}\sum_{e\in E} d(e,R)\right) \tag{6.10}$$

where N_r and N_e are the number of points of the contours. Also MAD is not a suitable measure of the discrepancy between opened curves, thus the following quantity was used to evaluate the effects of CS:

$$MAD_{re}(R,E) = \frac{1}{N_e}\sum_{e\in E} d(e,R) \tag{6.11}$$

Both H and MAD do not give information about bias. The areas of the closed contours were quantified to compute the ratio among the areas:

$$A_r(R, E) = \frac{\Gamma_E}{\Gamma_R} \tag{6.12}$$

where Γ_R is the area circumscribed by the set of point of the reference contour, and Γ_E by the estimated contour.

The Kolmogorov-Smirnov test was used to investigate whether the parameters distributions were normal. To evaluate the effects on the estimated parameters of the prosthesis models, *blur* and *vig*, different sets of Kolmogorov-Smirnov tests were performed ($P < 0.05$). The post hoc Bonferroni correction was then used for multiple comparison. The effect of the contour suppression was analyzed with the Mann-Whitney U-test ($P < 0.05$). All statistical analyses were performed with NCSS (NCSS, Kaysville, USA).

In-vivo

In order to evaluate its performance, the algorithm was applied to a dataset of 100 images of a knee prosthesis kinematics acquired with the bi-planar fluoroscopic acquisition system described in chapter 5. The same dataset was also segmented manually with the commercial software MBRSA of Medis Special (Leiden, The Netherlands). The same software, which implements the alignment algorithm described in [72], was used to quantify the kinematics considering either the automatic or the manual contours, in order to test whether the final accuracy of the pose estimation is affected by the new automatic segmentation algorithm. The differences between the results from the two methods were calculated for each frame of data and resumed in terms of median (m), interquartile range (iqr) and kurtosis (k). The limits of agreement of the alignments were determined using the methods described by Altman and Bland [131]. These methods were specifically developed in order to describe agreement between measurement methods. This "limits of agreement" approach calculates an upper and lower limit, between which 95% of the differences between the two methods can be expected to fall. Being the distribution of the variable non-gaussian, the non parametric Bland-Altman plot was used [132].

6.3 Results

The new semi-automatic algorithm requires the user to provide only one seed and the choice of one threshold level per image, per segment. The computational time is $\sim$1 min per segment (AMD Turion64 X2 2.00 GHz, RAM 2.00 GB laptop), $\sim 5-10$ s of which of user interaction only. The algorithm can efficiently avoid cemented part (Figure 6.2, a5), but is negatively affected by image blurring (Figure 6.2, b5).

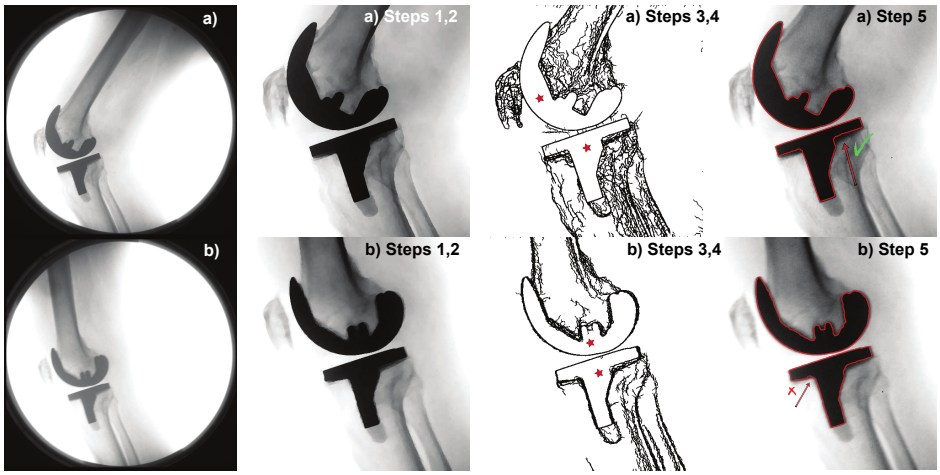

Figure 6.2: Intermediate steps of the image elaboration for the automatic prosthesis segmentation. The stars represent the seed points.

6.3.1 *In-silico*

The Kolmogorov-Smirnov test performed on the extracted parameters demonstrated that the distributions were not normal ($P > 0.1$). Non-parametric statistical tests were used to analyze the results. The Kruskal-Wallis test was performed on every combination of the factor levels. It highlighted that the procedure was not sensitive to the vignetting vig (no significant difference on any parameter). The prosthetic model significantly influenced ($P < 0.01$) the quality of the segmentation, being the hip model the most problematic with a median $H \simeq 5$ px. However, the average error, quantified by MAD, was not significantly different among the models, ranging from 0.1 px for $blur = 0$ px to a maximum

of $\simeq 2\ px$ for $blur = 10\ px$.

As expected, the level of blurring ($blur$) had major effects on all the parameters (see Figure 6.4). Both H and MAD increased with the blurring. Moreover, if A_r was approximately equal to 1 with $blur = 0\ px$, it became significantly lower than 1 with larger $blur$. This result implies a Γ_R larger than Γ_E and a bias in the contour extraction (Figure 6.3).

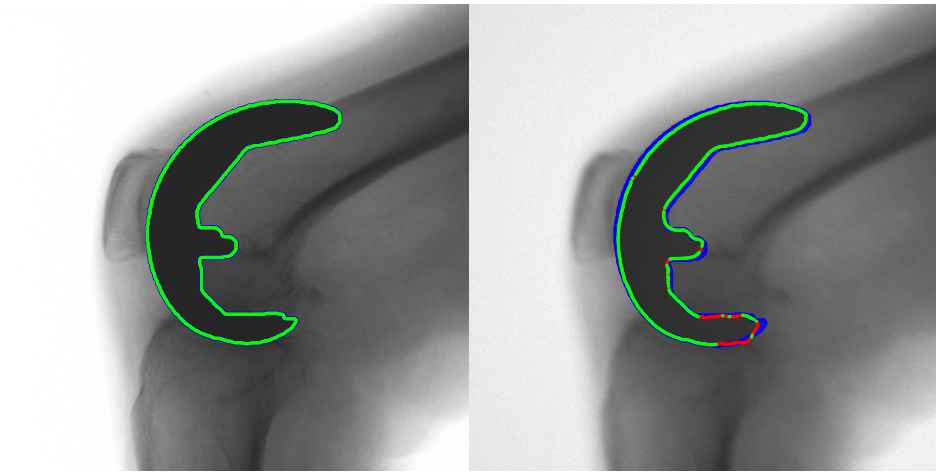

(a) $blur = 0\ px, vig = 0$ **(b)** $blur = 10\ px, vig = 0.10$

Figure 6.3: Examples of the results of the *in-silico* evaluations. The blue contour is the gold-standard reference, the green is the extracted one and the red points are the one automatically suppressed ($CS = 1$). Without blurring (Figure 6.3a) the two contours are overlapping, while with high level of blurring the extracted contour is shrunk (Figure 6.3b). The CS contributed to automatically eliminate the less accurate points.

The automatic contour suppression (CS) contributed to the reduction of both the Hausdorff distance and Mean Absolute Deviation. Figures 6.5 and 6.6 show the effect of CS on H_{re} and MAD_{re} respectively. The reduction was statistically significant (Mann-Whitney U-test, $P < 0.01$) and larger for the hip model.

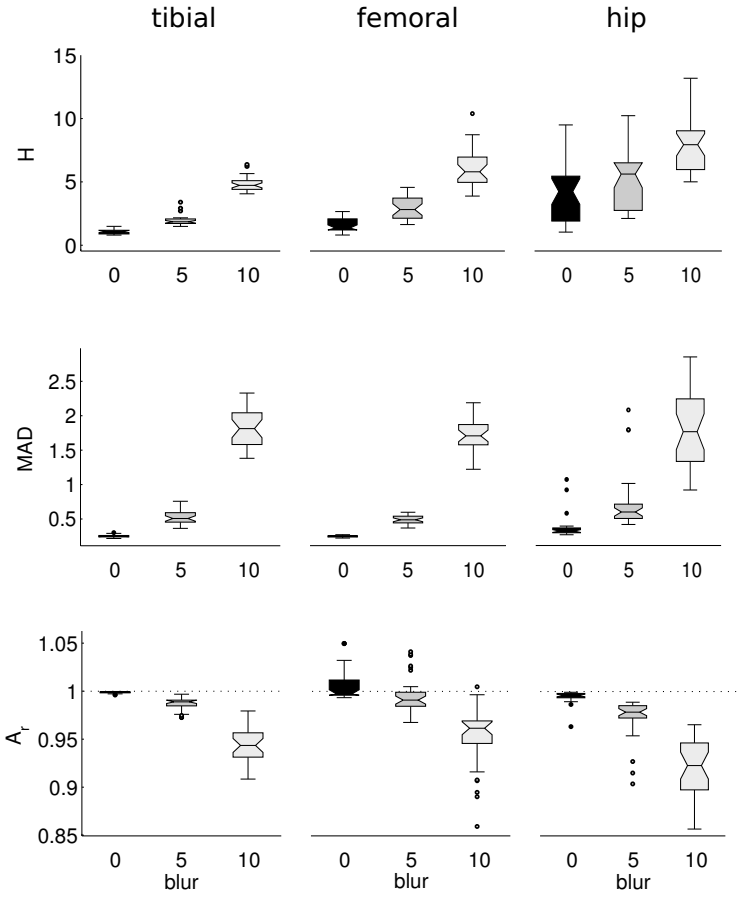

Figure 6.4: Hausdorff distance (H), Mean Absolute Deviation (MAD), and area rate (A_r) with respect to different level of *blur* and different prosthesis models. The Kolmogorov-Smirnov test highlighted a significant statistical effect of both the model and *blur*. All the values but A_r are expressed in *pixel*.

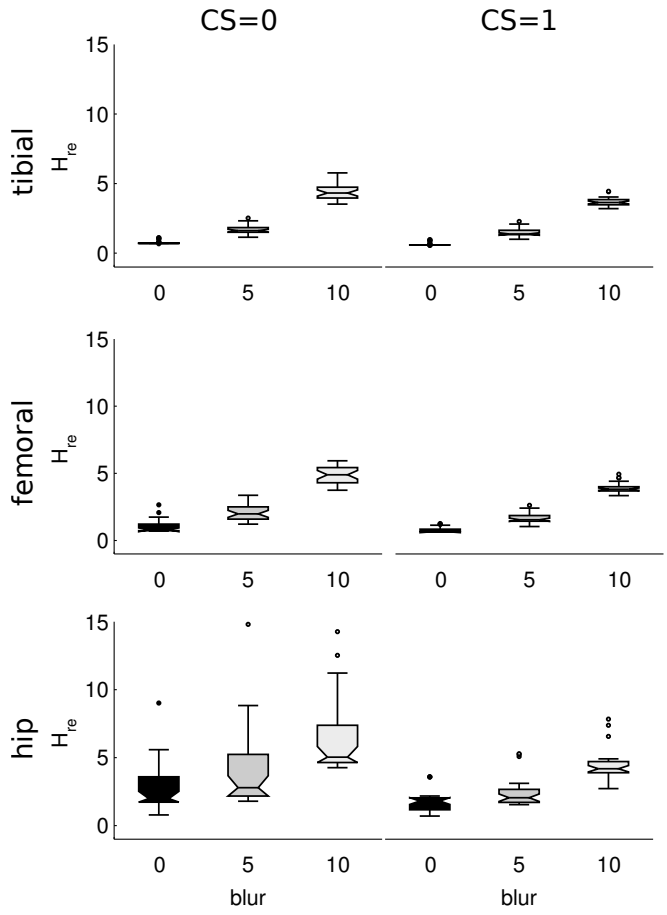

Figure 6.5: Hausdorff distance (H_{re}) with respect to different level of *blur*, different prosthesis models and with ($CS = 1$) or without ($CS = 0$) the contour suppression. The Mann-Whitney U-test highlighted a statistically significant reduction of H_{re} with the contour suppression. All the values are expressed in *pixel*.

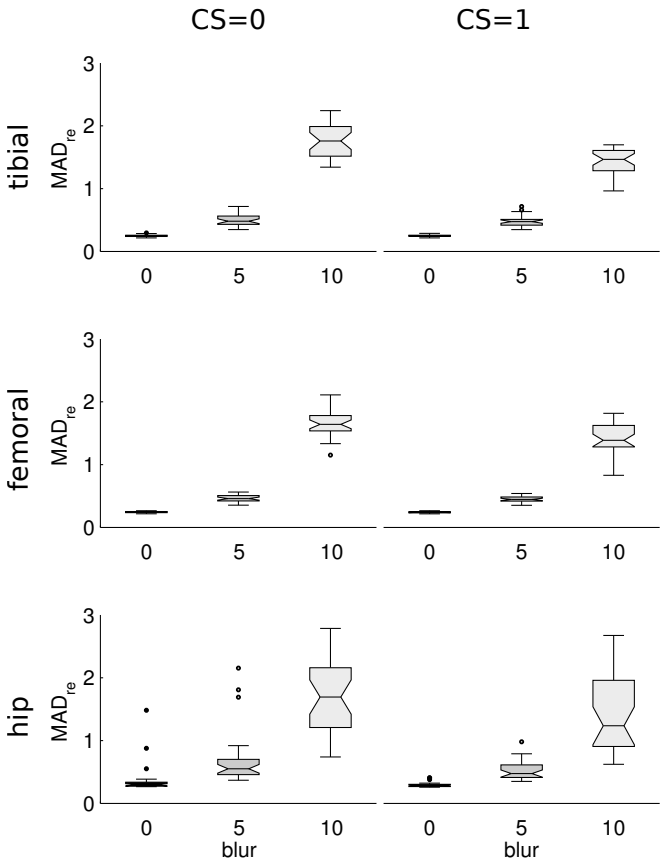

Figure 6.6: Mean absolute deviation (MAD_{re}) with respect to different level of *blur*, different prosthesis models and with ($CS = 1$) or without ($CS = 0$) the contour suppression. The Mann-Whitney U-test highlighted a statistically significant reduction of MAD_{re} with the contour suppression. All the values are expressed in *pixel*.

Table 6.1: Median m, interquartile range iqr and kurtosis k of the discrepancies between the alignment quantified with automatic and manually extracted contours in the *in-vivo* evaluation.

DOF	femur			tibia		
	m	iqr	k	m	iqr	k
T_x $[mm]$	0.31	0.12	7.41	0.27	0.20	32.31
T_y $[mm]$	~ 0	0.07	5.68	0.03	0.17	40.87
T_z $[mm]$	0.11	0.32	12.62	0.01	0.59	13.34
Θ_x $[deg]$	0.05	0.21	5.66	-0.01	0.12	8.36
Θ_y $[deg]$	-0.04	0.27	3.47	-0.15	1.45	6.47
Θ_z $[deg]$	0.06	0.18	3.31	0.01	0.32	8.26

6.3.2 *In-vivo*

No qualitative macroscopic differences were found comparing the visual appearances of the automatic and the manual extracted contours on the *in-vivo* evaluation of the algorithm. The comparison of the absolute kinematics estimations made on the two different contours (see Figure 6.7a for the femoral component), highlighted that the curves are overlapping for all the Degrees Of Freedom (DOFs).

Table 6.1 resumes the distributions of the differences in the pose estimation for every DOFs and for the prosthetic models. The iqr were always lower than 1 excepts for the tibial Θ_y. Figure 6.7b represents the same data for the femur in the form of a Bland-Altman plot. It is confirmed that the agreement between the two alignments is in the order of magnitude of the accuracy of the fluoroscopic technique, but a small bias of 0.3 mm is highlighted only for T_x.

6.4 Discussion

A promising method for the semi-automatic prosthesis segmentation in 3DF was implemented. While the traditional methods need $\sim 1-2$ min completely born by the user, the computational time of the new method is ~ 1 min per segment (AMD Turion64 X2 2.00 GHz, RAM 2.00 GB laptop). Only $\sim 5-10$ s of user interaction were needed to specify a seed point and a threshold on the edge

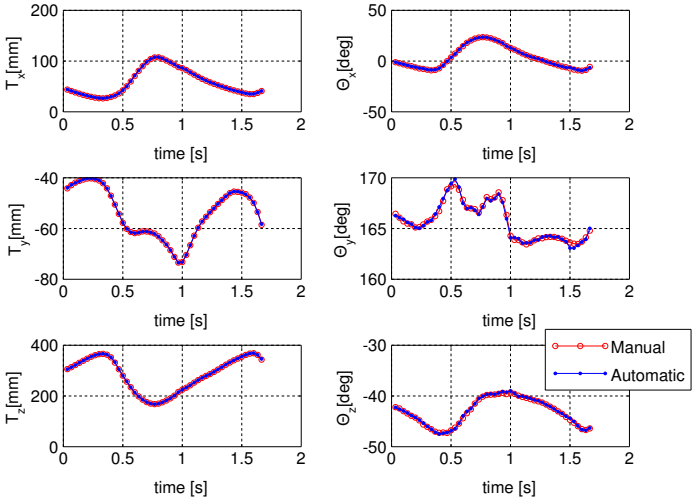

(a) Absolute kinematics

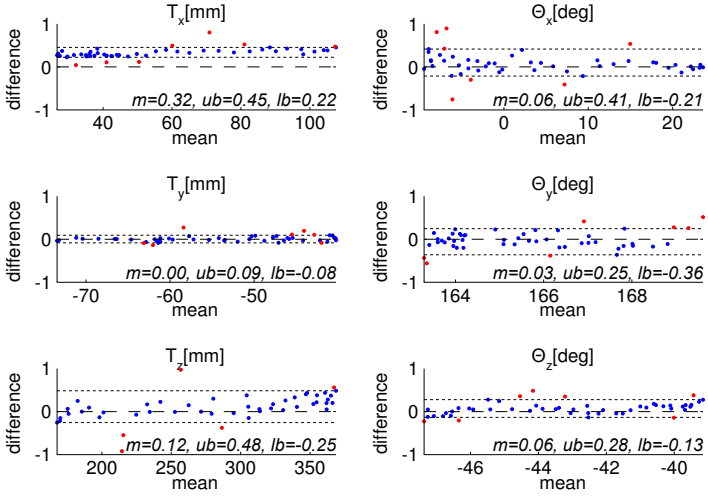

(b) Bland-Altman

Figure 6.7: Comparison of the absolute kinematics of the femur (6.7a) quantified with automatic and manually extracted contours. Figure 6.7b shows the Bland-Altman comparison plot with the relevant 95% upper and lower limit of agreement.

indicator (Equation 6.3). Even if a short manual procedure is still useful to eliminate wrong contours in case of components overlapping, the manual time can be further reduced implementing a batch processing to propagate the seed from the first frame to the following.

The prosthesis shape had no effect on the average error MAD, but influenced the maximum error quantified by H. This might be explained by the fact that the hip prosthesis shape is longer than the femoral and tibial knee components, and then it went across parts of the image with different gray levels, which became as dark as the prosthesis closed to the proximal thigh due to the massive presence of soft tissues. On the other hand, even without using any a priori knowledge about the prosthesis shape, the algorithm can efficiently avoid eventual cemented parts (Figure 6.2, a5) and the results are then generalizable to other prosthetic models. Even if not eliminated with the procedure described in Section 1.2.1, the presence of vignetting does not interfere with a proper segmentation of the prosthesis. The light invariance is an improvement step if compared to the segmentation method proposed by Domokos et al. [135] which was affected by illumination variations typical of fluoroscopic images.

The major limitation of the technique is that image blurring can negatively affect the accuracy of the segmentation (Figure 6.2, b5). If a prosthesis move in one direction, this will create two opposite front of blurred contour on the sides orthogonal to the movement (Figure 6.3). Being based on an internal region growing method, the technique can only detect the inner contours, as confirmed by the area ratio parameter which is always lower than 1 for blurred images (Figure 6.4). The contour suppression can reduce the presence of outliers (decreasing H_{re}), but a residual error, of approximately halved magnitude with respect of $blur$, is present (Figure 6.5). The mean absolute deviation was however always lower than 1 $pixel$ even with a medium level of blurring ($blur = 5\ px$)

On the other hand, the *in-vivo* evaluation of the method highlighted that the agreement between the alignments carried out on the manual and automatic extracted contours is in the order of magnitude of the accuracy of the technique (Figure 6.7). Only the iqr of agreement in the estimation of the tibial Θ_y was slightly larger than one (Table 6.1), but this is probably due to a prosthesis model intrinsic symmetry and not related to the segmentation. Thus, the effect of blurring affected in the same way both the manual and the automatic extracted contours. On top of that, the increasing use of flat panels, that are substituting the X-Ray Image Intensifier (XRII), will certainly introduce technical improve-

ments in the fluoroscopic image acquisition chain, that will reduce the occurrence of blurred images.

The implemented method is then a major improvement of the fluoroscopic analysis of prostheses, the analysis time has been halved and delegated to the computer, without losing in accuracy and robustness.

6.5 Conclusions

The present work represents a first evaluation study of the application of well-known segmentation algorithms in the specific context of 3D fluoroscopy. Promising results were obtained allowing the improvement of the analysis of prosthesis kinematics in term of automation and reduction of the user interaction. A batch processing will also allow to automate the seeding step.

CHAPTER

SEVEN

3D VIDEO-FLUOROSCOPY FOR THE QUANTIFICATION OF 3D FOOT KINEMATICS: A PRELIMINARY STUDY

Part of the material described in this chapter was submitted to:

- R. Stagni, **L.Tersi**, S. Fantozzi, Z. Sawacha, A. Guiotto, C. Cobelli: In-vivo foot kinematics: definition of a fluoroscopic gold standard for the evaluation of marker-based protocols. In: proceedings *i-Fab 2010*, Seattle, September 16-18, 2010.
- Z.S. Sawacha, A. Guiotto, C. Fassina, S. Fantozzi, R. Stagni, **L. Tersi**, C. Cobelli. Use of multiple calibration in multisegment 3D foot kinematics: In: proceedings *i-FAB 2010*, Seattle, September 16-18, 2010.
- Z. Sawacha, A. Guiotto, S. Fantozzi, R. Stagni, C. Fassina, **L. Tersi**, C. Cobelli: Advantages of multiple calibration in multisegment foot 3D kinematics. In: Proceedings *GCMAS 2010*, Miami, Florida USA. May 12-15 2010.
- A. Guiotto, Z.S. Sawacha, C. Fassina, **L. Tersi**, S. Fantozzi, R. Stagni, C. Cobelli: Use of multiple calibration in multisegment foot 3D kinematics. In: proceedings *GNB 2010*, Torino, 8-10 July 2010.
- R. Stagni, **L. Tersi**, S. Fantozzi, Z. Sawacha, A. Guiotto, C. Cobelli: Definition of a fluoroscopic gold standard for the evaluation of marker-based protocols. Submitted to *XXIII congress of ISB 2011*, Brussels, Belgium, July 3-7, 2011.
- R. Stagni, **L. Tersi**, S. Fantozzi, Z. Sawacha, A. Guiotto, C. Cobelli: In-vivo foot kinematics: definition of a fluoroscopic gold standard for the evaluation of marker-based protocols. Submitted to *2011 Gait and Clinical Movement Analysis Society - GCMAS*, Bethesda, MD, USA, April 26-29, 2011.

7.1 Introduction

To explore the potentialities of the new validated method, its first preliminary application will be presented in the following Chapter. This methodological study aimed at the definition of a fluoroscopic gold-standard based on a functional-anatomical model for the assessment of marker-based foot protocols.

The evaluation of the foot segmental kinematics is a clinical information extremely relevant for several pathologies such as clubfoot, flatfoot, cerebral palsy and in particular diabetes. Standard protocols of gait analysis [143, 144, 145, 146] model the foot as a single rigid segment, thus are not suitable for performing this type of evaluation.

For this reason, in the last years, several multi-segmental foot models were proposed [25, 147], they differ for several characteristics such as (a) the number of segments into which the foot is divided from 2 to 9, (b) the type of angular convention adopted, (c) the technology used for kinematics quantification. Applying these models different pathologies were investigated: rheumatoid arthritis [148], hallux rigidus [149], posterior tibial tendon dysfunction [150]. Despite the number of models proposed, two questions, clinically and methodologically relevant, are still open: the definition of the neutral reference position, compatible with the deformities associated to foot pathologies, and the influence of Soft Tissue Artefact (STA) in the kinematics estimation, which is strictly related to the definition of foot sub-segments that are not rigid.

Foot protocols evaluate segmental specific kinematics applying skin sensors, mainly using stereophotogrammetry while in few cases using electromagnetic sensors. Thus, the kinematics assessment is subjected to STA, that leads to errors in joint translations and rotations of some centimeters and several degrees, respectively [29]. Moreover, foot sub-segments are intrinsically deformable. The majority of proposed protocols were validated in terms of measure repeatability [23, 24, 25, 151], but only few studies estimated accuracy [26, 27, 28, 152] and thus the significance for the clinical decision process of the quantified variables.

Cadaver studies evaluated the rigidity hypothesis of the foot sub-segments [27] and the choice of anatomical landmarks for the definition of a reference systems appropriate for the relevant kinematics description [152]. All these evaluations were performed on cadavers, thus they can hardly represent the clinically operative *in-vivo* conditions: furthermore, it is difficult to expand the approach for the evaluation of new protocols. When bone kinematics reconstructed us-

ing markers applied on the skin and on rigid plates was compared *in-vivo* with the one obtained from intra-cortical pins [26], it was not possible to acquire all the measurements simultaneously due to the limited dimension of the Field Of View (FOV). Thus, the results can be considered valid under a strict hypothesis of motor task repeatability, and even a simultaneous acquisition would have underestimated STA, because pins limit skin motion. Less recently, using radiologic techniques that do not limit skin motion, STA was evaluated *in-vivo* in the foot, but the performed analysis was only 2D [28].

In order to validate stereophotogrammetric protocols, it is essential to have a gold-standard for the accurate *in-vivo* quantification of the 3D multi-segmental foot kinematics during activities of daily living, that could be applied for several models and protocols. Several techniques allow to estimate, with accuracy sufficient for validation purpose, *in-vivo* joint kinematics, i.e. the six Degrees Of Freedom (DOFs) that define position and orientation in 3D space. Although the use of intra-cortical pins allows one of the best accuracy, it cannot be adopted for human tests [26, 32, 33] for obvious ethical reasons, skin movement limitation and possible kinematics alteration. Roentgen Stereo-photogrammetric Analysis (RSA), designed for the quantification of prostheses components fixation, was also used for *in-vivo* joint kinematics [36], but is highly invasive as it is based on traditional X-rays and requires surgical intervention for radiopaque markers implantation. Finally, techniques based on computer axial tomography or magnetic resonance [37, 39] have a small FOV, and a frame rate not sufficient for dynamic tests without combining data from a sequence of cyclic repetitions.

The best compromise among low invasiveness, high accuracy of dynamic analyses and flexibility was found by Banks et al. using a mono-planar fluoroscopic technique [12]. 3D video-fluoroscopy (3DF), has not been applied to quantify *in-vivo* kinematics of foot segments yet, but it was used for kinematic evaluation of ankle joint [46]. For the accuracy level and the possibility to acquire relatively fast dynamics (up to 50fps with modern fluoroscopes), 3DF was used as a gold-standard for the validation and the evaluation of error associated with non invasive techniques for the quantification of motion [4, 49] and to compare the performance of different STA compensation methods [50], and markers configuration [153, 154]. Up to now, 2D radiological techniques were used to quantify STA at the foot [28], estimating a motion of 4.3 *mm* of skin markers with respect to the underlying bony segments or cadaver studies were performed [27].

In order to apply 3DF to the foot and to obtain data for the validation of foot

protocols, the kinematics of the foot bony segments quantified using 3DF must be related to the kinematics of the deformable foot segments quantified using stereophotogrammetry. Due to the number and dimension of foot bony segments [155], to the impossibility of estimating the kinematics using skin markers, to the low correlation between internal dimension and external measures [4], and to the deformability of the biomechanical model segments, typically functional axes are adopted [155, 156, 157]. Thus, in contrast with other joints analyzed using 3DF, where the 6 DOFs of the two bony segments in the joint (for the knee, femur and tibia) are estimated, in this case the technique must give the estimation of the functional rather than the anatomical axes. In this way, the estimated reference kinematics can be compared with kinematic data from stereophotogrammetry.

This Chapter describes the preliminary tests performed following this approach, starting from the definition of the fluoroscopic gold-standard based on foot functional models to assess the performance of the multiple calibration [5]. This method is expected also to deal with the anatomical deformation of foot segments.

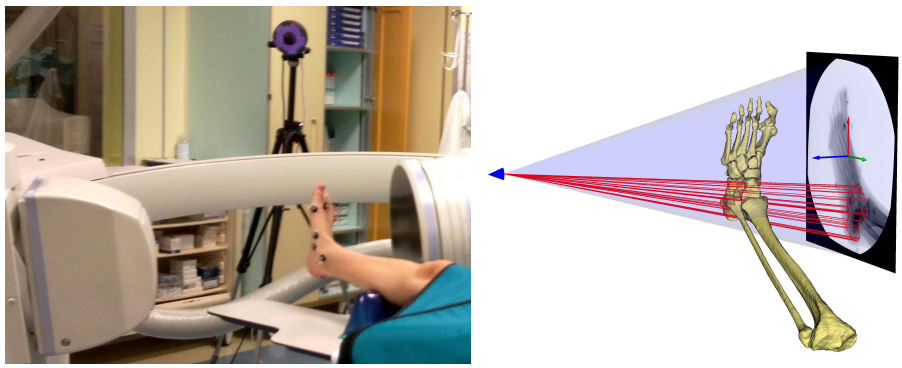

(a) Setup **(b)** Virtual

Figure 7.1: Synchronous stereophotogrammetric and fluoroscopic acquisition systems (7.1a), and relative virtual representation (7.1b).

7.2 Material and methods

7.2.1 Data acquisition

One subject (female, 26 years, 174 cm, 61 kg) signed an informed consent and participated to the study. The kinematics of foot and ankle was synchronously acquired using stereophotogrammetry (SMART-D, BTS, Italy) and fluoroscopy (Sirecon 40hd, Siemens), see Figure 7.1a. A 3D multisegment foot protocol proposed by Sawacha et al. [25] was applied on the same subject first by means of anatomical landmarks direct skin marker placement method, and second in a modified version which entails calibrating each anatomical landmark with respect to a local cluster of marker. Flexion-extension and inversion-eversion cycles were acquired, together with neutral and maximal flexion, extension, inversion and eversion static postures. Simplified movements were used to analyze the specificity of the modeling approach.

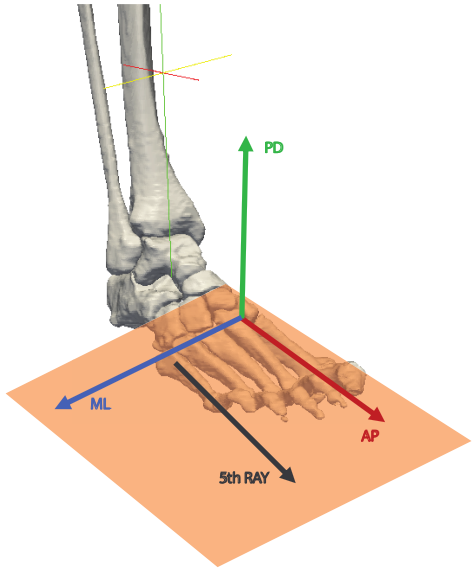

Figure 7.2: Definition of the functional model for the forefoot.

7.2.2 Functional models definition

Bone models of the foot were reconstructed from MRI scan using Simpleware [158], and used for the reconstruction of bony segments kinematics based on the anatomical-models. A function-based model was then adopted for the reconstruction of the kinematics of the 3 foot segments. Functional axes of each segment were associated to specific anatomical features of the relevant bony segments. For the forefoot, the antero-posterior axis was associated to the long-axis of the first ray and the vertical one to the plane containing the first and the fifth ray (7.2).

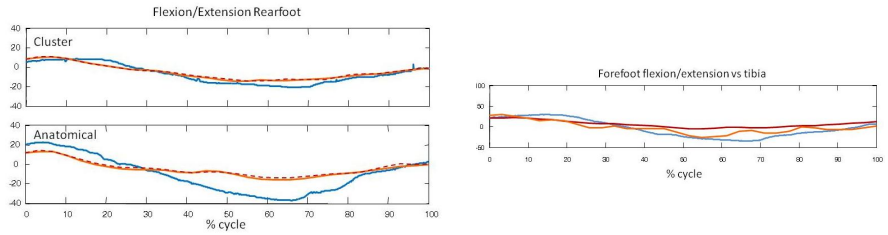

(a) Hind-foot **(b)** Fore-foot

Figure 7.3: Flexion-extension of the hind-foot (7.3a), and of the fore-foot (7.3b) reconstructed using stereophotogrammetry (blue), fluoroscopy on solid model (red), and fluoroscopy on compound deformable model (yellow). For the hind-foot, two stereophotogrammetric protocols were compared.

The hind-foot reference frame was defined using anatomical landmarks on the multiple segments. In particular the medio-lateral direction was defined parallel to the substentaculum talii and the fibular tuberosity. The vertical direction was defined orthogonal to the plane defined by medio-lateral axis and the line connecting the upper ridge of the calcaneus posterior surface to the substentaculum talii, and the antero-posterior axis was orthogonal to the previous. Given this reference frame, the alignment was repetead considering the single calcaneus, and considering the compound segment composed by calcaneus and talus.

7.3 Results

The preliminary results show that, for the hind-foot, angles quantified using stereophotogrammetry overestimated the motion quantified using 3D fluoroscopy,

particularly for large motion ranges. On the other hand, during unloaded motion no significant difference could be observed between the motion of the calcaneus and the motion of the whole hind-foot (talus-calcaneus), reconstructed using 3D fluoroscopy. For the forefoot, instead, significant difference can be observed between the kinematics reconstructed considering the whole fore-foot geometric model using 3D fluoroscopy and the one reconstructed from the 3D kinematics of the I, II and V metatarsal separately.

7.4 Discussion

The preliminary results show that the function-based model constrained to bony segment kinematics provides a good specificity in describing the relative kinematics of foot sub-segments, while the kinematics of the different bony segments within the sub-segments can hardly be generalized, without the proposed functional approach. The two different stereophotogrammetric protocols could not be compared because the motion tasks were not standardized, however the anatomical protocol seems to overestimate the flexion-extension angle for the fore-foot.

For this *in-vivo* acquisition, the fluoroscopic system Sirecon 40hd (Siemens) declared a dose of 4.8 μR per image. A total number 600 frames were acquired at 6 fps, corresponding to 3000 μR which are equivalent to 0.36 mSv, approximately one third of the annual limit of 1 mSv(Section 1.2.1). Moreover, this value correspond to the emitted dose while the skin absorbed dose would certainly be lower. To obtain a reliable measurement of the skin absorbed dose, dosimeters will be used in future evaluations.

The present methodology is ongoing further evaluation, resulting a promising tool for the evaluation of marker-based foot protocols.

7.5 Conclusions

Once validated, the improved 3DF method was applied for the first time to a preliminary methodological study on the *in-vivo* foot and ankle kinematics. Synchronous stereophotogrammetric and fluoroscopic data of the foot kinematics were acquired. The fluoroscopic data were used as a gold-standard to validate a stereophotogrammetric foot protocol. Like any marker-based protocol, even the ones for the foot are prone to accuracy limitations due to STA and to the

deformability of the foot throughout the gait cycle. 3DF can accurately quantify the necessary gold-standard foot kinematics, but, due to the small size and the symmetries of the involved bones, the hind-, mid- and fore-foot had to be analyzed as compound segments. These segments, however, are intrinsically deformable, and the proposed gold-standard had to be based on functional-anatomical models.

Preliminary results showed that the function-based model constrained to bony segment kinematics provides a good specificity in describing the relative kinematics of the foot sub-segments, while the kinematics of the different bony segments within the sub-segments can hardly be generalized, without the proposed functional approach. The present methodology is ongoing further evaluations, resulting a promising tool for the evaluation of marker-based foot protocols. Among these, the use of image based features seems to be promising for the estimation of the projections of the heads and the bases of metatarsal bones, which can assist the pose estimation process and to provide higher accuracy and robustness of the results.

GENERAL CONCLUSIONS

The goal of the current Ph.D. project is to introduce methodological improvements in the 3D fluoroscopic analysis to make it more robust and reliable. To this aim, an analytical identification of the various sources of error was carried out, investigating solutions to improve the reliability of the results and to automate and speed up the data analysis, reducing user and computational errors on the human joint kinematics estimation. The objectives were fully achieved leading to a more mature and user friendly technique, in which the user interaction was reduced and the cumbersome data analysis delegated to the machine. The reduction of the manual interaction contributed not only at decreasing the "cost" of the analysis, but it also went in favor of the robustness and the reliability of 3D video-fluoroscopy (3DF).

The fluoroscopic methods are mainly divided into two categories: the mono-planar methods, which investigate a big volume with a low X-ray dose, and the bi-planar methods, more accurate but invasive and expensive. A number of alignment algorithms are proposed in the literature such as the contour matching, the one based on Digitally Reconstructed Radiographies, or the model based Roentgen Stereo-photogrammetric Analysis. The analyzed 2D-3D registration algorithm was based on tangency condition between the 3D model of an object and the relevant projection rays, due to its light computational weight and to the ability of dealing with opened contours.

To consider the worst case scenario, the less reliable mono-planar setup was characterized in depth. The main result concerns with the improvements on the optimization algorithm for the pose estimation, which is a common step of every alignment algorithms. The introduced ameliorations, thus, lie outside the speci-

ficity of the presented mono-planar method and can be easily generalized to the other alignment algorithms (both mono-planar and bi-planar). The achievements constitute a general improvement of 3DF favoring its introduction in the clinical practice.

To achieve this general results it was necessary to identify the points of strength and the potentially improvable limitations of the 3D fluoroscopic analysis. This analytical process was carried out starting from *in-silico* preliminary analyses which contributed to isolate the effects of different sources of errors. The image distortion correction and the calibration procedures were found to be effective. It was pointed out that the errors related to the bone morphology and symmetries cannot be avoided because intrinsic to the analyzed segment. The accuracy of the technique is then joint-dependent, and different validation studies must be accomplished any time a new joint is analyzed, characterizing precision and accuracy of 3DF in the specific context.

The *in-silico* evaluations highlighted that the major source of error was related to the poor global performance of the local optimization algorithm typically used to detect the bone or prosthesis pose. An extensive sensitivity analysis was carried out in order to describe the convergence properties of the algorithm, and to develop local and global solutions to enlarge the global optimum basin of attraction. A sequential optimization algorithm combined to a geometrical feature-based estimation of the initial guess for the pose optimization contributed to improve the local search algorithm. From a global point of view, a further improvement was introduced by a memetic algorithm designed merging together the improved local search and a global genetic algorithm. The performed *in-silico* evaluations quantified the accuracy and precision of the new robust method, and it was demonstrated that the memetic algorithm can provide excellent results even without the supervision of the user. Tuning the optimization parameters, it was possible to estimate the most problematic out-of-plane pose parameters with limited bias and dispersion (in the order of few millimeters and degrees depending on the considered bone model) also with a mono-planar setup.

Due to the absence of non-invasive gold-standards, the *in-vivo* validation of 3DF applied to intact joints was not viable. The new robust method was then validated considering the accurate marker based Roentgen Stereo-photogrammetric Analysis (RSA) as an *in-vitro* gold-standard for the quantification of the kinematic of a phantom knee joint. The RSA was based on the implantation of a cluster of markers on the bone model surfaces and on the acquisition of two

synchronized fluoroscopic projections. This allowed the comparison of the performances of the mono-planar and bi-planar setups considering all the sources of error that could be found in an *in-vivo* session. The bi-planar alignment proved to be extremely accurate and precise, but it was limited by the significant reduction of the investigable volume. The performances of the mono-planar setup were comparable to the bi-planar when considering the in-plane pose parameters, and the error is condensed in the out-of-plane direction. Nonetheless, the mono-planar setup has halved costs, halved analysis time and halved ionizing radiation dose for the patient. It was concluded that the high accuracy of the bi-planar method is better suited for research activities, but the reliability of the mono-planar alignment can be sufficient for clinical analysis. Given the mono-planar specific limitations, however, the acquired motion tasks must be designed in a way that the important informations are gathered in the in-plane directions.

A further improvement towards the automation of 3DF concerning the image segmentation was proposed. Many fluoroscopic methods rely on the contours extraction of the segment of interest in the fluoroscopic images. The procedure was typically accomplished with a time consuming manual elaboration. Little can be done for the segmentation of intact joint bones, due to the bones overlapping and to the low constrasted images. On the other hand, the segmentation process can be automated for prosthesis analysis. A new semi-automated method for prosthesis segmentation was designed as a combination of well-known algorithms such as level-set and region growing, in the specific context of 3DF. With the new algorithm the analysis time was halved and, more importantly, only few and fast manual steps were needed. Promising accuracy and repeatability results were quantified with an controlled *in-silico* evaluation. An *in-vivo* analysis highlighted that no differences can be seen on the final pose estimation accuracy comparing the manual and the automatic segmentations. The analysis of prosthesis kinematics was then improved in term of automation and reduction of the user interaction.

Once validated, the improved method was applied for the first time to a methodological study on the *in-vivo* foot and ankle kinematics. Synchronous stereophotogrammetric and fluoroscopic data of the foot kinematics were acquired. The fluoroscopic data were used as a gold-standard to validate a stereophotogrammetric foot protocol. Like any marker-based protocol, even the ones for the foot are prone to accuracy limitations due to soft tissue artefact and to the deformability of the foot throughout the gait cycle. 3DF can accurately quantify the

necessary gold-standard foot kinematics, but, due to the small size and the symmetries of the involved bones, the hind-, mid- and fore-foot had to be analyzed as compound segments. These segments, however, are intrinsically deformable, and the proposed gold-standard had to be based on functional-anatomical models. A fluoroscopic gold-standard was proposed and the preliminary results showed that the function-based model constrained to bony segment kinematics provides a good specificity in describing the relative kinematics of the foot sub-segments, while the kinematics of the different bony segments within the sub-segments can hardly be generalized, without the proposed functional approach. The present methodology is ongoing further evaluation, resulting a promising tool for the evaluation of marker-based foot protocols

Concluding, this Ph.D. delved deeply into the problems concerning the 3DF analysis. The limitations were identified, described and, when possible, overcome. In the improved methodology, the user interaction was reduced in favor of the robustness of the technique. The introduced improvements made the mono-planar method more reliable. As compared to the more accurate bi-planar method, the mono-planar halves the radiation dose for the patient and the costs associated with the examination. Its use in the clinical practice is then more suitable than that of the bi-planar method. Still, the mono-planar has some accuracy limitation in the out-of-plane direction, and this aspect must be taken in consideration during the design of the motor task to be analyzed.

Further improvement may be introduced analyzing and comparing the different alignment algorithm proposed in the literature in relation to the specificity of the investigated joint. On the other hand, now that 3DF has been improved and validated, future applications might be foreseen. From a methodological point of view, further validation study will be undertaken along the path indicated by the first foot study. Certain advances will be made in the soft tissue artefact quantification and modeling and, finally, the technique will eventually be introduced in the clinical field thanks to contacts with industrial and clinical partners established during the Ph.D. activities.

APPENDIX

A

THE FLUOROTRACK SOFTWARE: USER GUIDE

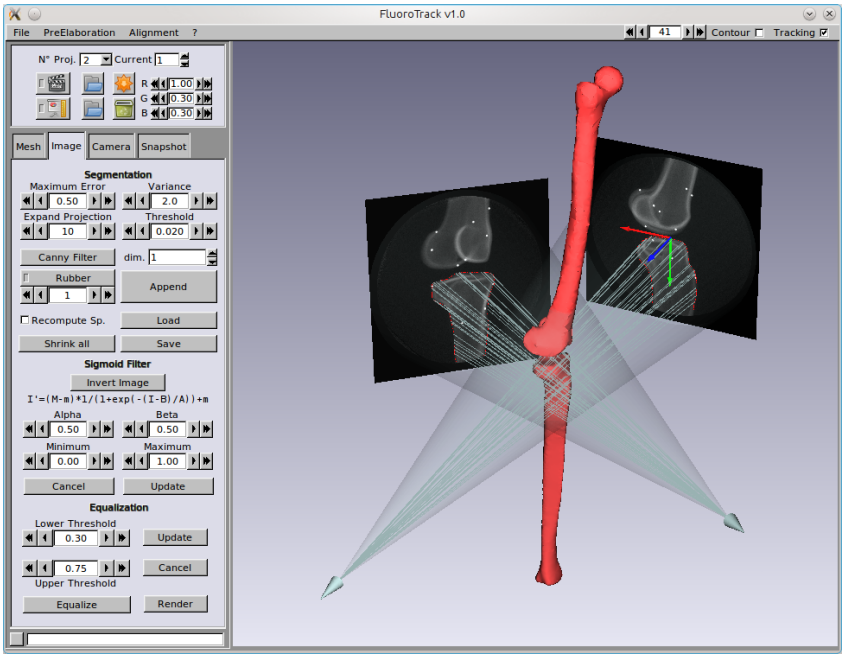

Figure A.1: FluoroTrack snapshot

A.1 Introduction

The software FluoroTrack was developed in order to provide a comprehensive framework for the 3D fluoroscopic analysis for the kinematics estimation of natural and prosthetic joints. FluoroTrack was used both for the analysis of real fluoroscopic data, and to generate *in-silico* datasets used for testing previous and newly developed algorithms. It was coded in C++ language, based on algorithms and tools provided by open source libraries:

- Fast Light Toolkit - FLTK, for the development of the graphical user interfaces [159],
- Insight Segmentation and Registration Toolkit - ITK, for 2D and 3D image processing [160],
- Visualization Toolkit - VTK, for the 3D computer graphics, image processing and visualization [161].

The software provides a virtual scene in which it is possible to manually or automatically interact with the fluoroscopes (image planes and X-ray sources) and the 3D models representing the segments to be aligned.

In the following sections, the main steps of the various data analysis will be presented.

A.2 Typical analysis workflow

A.2.1 Distortion correction

The first operation, before the estimation of the 3D kinematics with any radiographic technique, is the geometrical distortion correction of the fluoroscopic images. The *Calibration* window can be found in *Pre-Elaboration* → *Calibration* menu, and it provide the functionality necessary to this aim (Figure A.2). The steps for the elaboration will hereby be described:

1. **Open Light**: button to open an image of the empty Field Of View (FOV) in order to correct for vignetting (Section 1.2.1).
2. **Open Grid**: button to open the acquired image of the calibration grid.

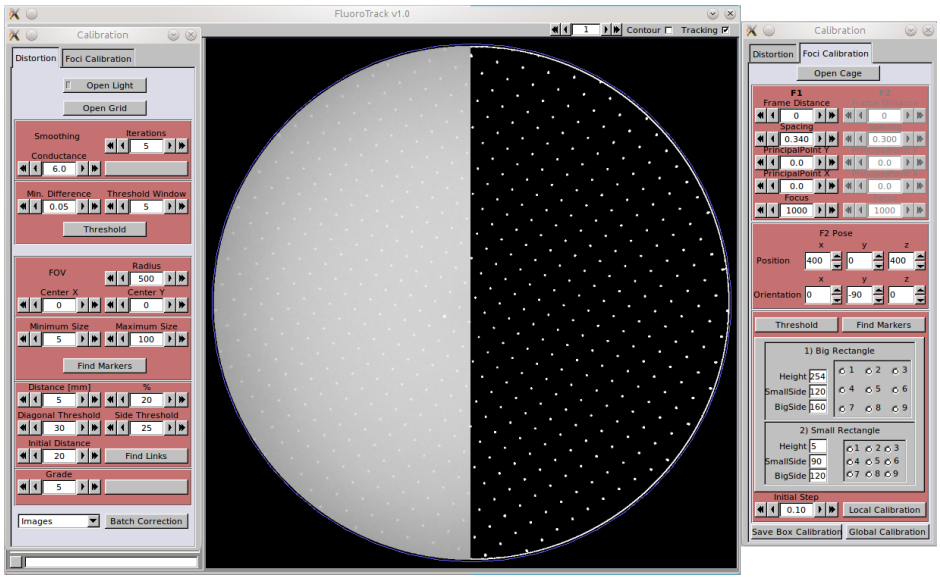

Figure A.2: FluoroTrack: Calibration window (tab Distortion, and tab Foci Calibration). The calibration grid before and after thresholding is displayed.

3. **Smoothing**: parameters to be set for the curvature anisotropic diffusion image filter which is an edge preserving smoothing filter.

4. **Threshold**: parameters to be set for an brightness-invariant adaptive threshold filter aimed at the calibration grid beads detection. For each pixel, two automatic thresholds t are chosen as follow:

$$t_1 = m_d(I_M - I_m); \tag{A.1}$$

$$t_2 = \frac{2W_M + W_m}{3}; \tag{A.2}$$

$$p_{i,j} = \begin{cases} 0, & if \quad W_M - W_m < t_1 \\ 0, & if \quad W_M - W_m > t_1, \quad I_{i,j} < t_2 \\ 1, & if \quad W_M - W_m > t_1, \quad I_{i,j} > t_2 \end{cases} \tag{A.3}$$

   where I_m and I_M are the minimum and maximum gray levels in the entire image I; W_m and W_M are the minimum and maximum gray levels in a window centered in the pixel i, j the side of which is specified in *Threshold Window*. The pixel is set to 0 if uniform areas and if it is darker than t_2, it is white otherwise. The beads will appear as white blobs (Figure A.2).

5. **Marker identification**: the beads centers are identified as the center of mass of the original image gray levels correspondent to each connected component, with a dimension included in *Minimum Size* and *Maximum Size*, and included inside the FOV specified by *Radius*, *Center X*, and *Center Y*.

6. **Linking**: *Find Links* starts an iterative procedure to associate the each marker with real grid. The grid spacing is specified by *Distance [mm]*, and the other parameters control the iterative procedure.

7. **Correction**: finally a polynomial correction is applied to a single image or to the whole fluoroscopic series in batch. *Grade* specify the grade of the polynomial [60]. This procedure estimates also the pixel spacing.

A.2.2 Foci calibration

Once corrected for distortions, the image of a calibration cage is analyzed with the tools provided by the *Foci calibration* tab.

1. **Open Cage**: to open the calibration cage image (already corrected for distortions).

2. **Threshold** and **Find Markers**: to identify the calibration cage beads with the same procedures described for the distortion correction.

3. **Labeling**: a manual labeling is necessary to associate the coordinates of a beads the real tantalum bead of the calibration cage. The labeling is carried out choosing a bead ID in *Big Rectangle* and *Small Rectangle*, and clicking on the correspondent bead center in the image with the middle mouse button.

4. **Local Calibration**: to estimate the position of the fluoroscope focus with respect to the center of the image (*Principal Point X*, *Principal Point Y*,*Focus*).

5. **Global Calibration**: to estimate the relative position of the two fluoroscopes in case of bi-planar 3D video-fluoroscopy (3DF).

6. **Saving**: it is possible to save the calibration settings in a .cal file, from the *Pre-Elaboration* → *Save Calibration* menu.

A.2.3 Setting the scene

The perspective projection calibration file can be imported through *Pre-Elaboration* → *Load Calibration*. The opening box in the main window provides the functionalities to open the image series (.dcm files), and the mesh models (.stl, .vtk, .txt file formats) of the bone or the prosthesis. Moreover, it is possible to display the absolute kinematics of a model, and to play a video of the acquisition. It is also possible to load a scene file (file .scn) using the *File* → *Open Scene* menu to open all the actors and calibration files at once. On the top right corner of the main window, a counter lets the user navigate to the opened frames.

The four tabs accessible in the main window (Figure A.3) provide the main functionalities to interact with the scene.

- **Mesh**: the user can change the opacity of the selected surface model (picked with the "p" keyboard key), and manually specify its position and orientation in the current frame. It is also possible to interact with the model using the mouse (left button to rotate, and right to translate, ctrl button

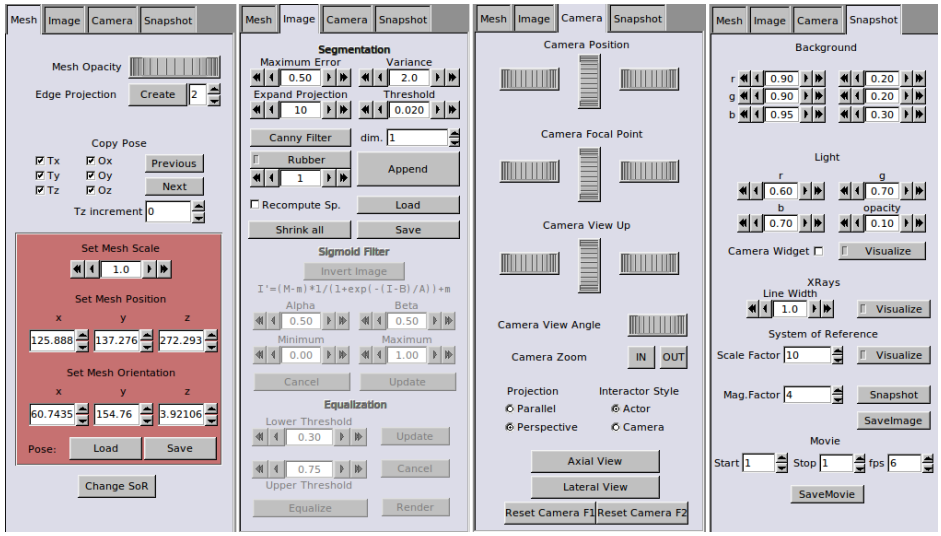

Figure A.3: FluoroTrack: Tools accessible from the main windows tabs.

must be pressed to act in the third dimension). The button *Edge Projection Create* can be used to project on the image plane the contour of the mesh in the current pose. The *Copy Pose* box is used to copy the pose from the previous or from the following frames. The *Save* and *Load* button are used to save and load the pose for the picked mesh (file .pose).

- **Image**: this tab provides the image processing tools useful for the contour extraction. The *Equalization* box is used to equalize the image in the gray level range specified by *Lower Threshold* and *Upper Threshold*. The values outside that range are forced to black or white respectively. The *Sigmoid Filter* applies a sigmoid to tune contrast and brightness of the image. The *Segmentation* box lets the user specify the parameters for the Canny edge detection. In particular *Expand Projection* is the dimension of a band, along the projection of the mesh, in which the Canny filter is applied. The rubber button changes the interactor in order to manually erase the undesired contours after the Canny edge detection. The contour are saved in .vtk file format. *Append* is used to append the contours of the single parts of a compound segment.

- **Camera**: is used to specify the position and the orientation of the camera on the scene. It is possible to use the sliders or to change the interactor from *actor* to *camera* to use the mouse. The *Reset Camera* put the camera exactly in the calibrated position of the X-ray sources. In this particular condition, if the mesh pose is correctly estimated, it is rendered aligned to the correspondent fluoroscopic image.
- **Snapshot**: is used to visualize and to change the color of the background, the X-ray cone of light, the X-ray source widget, the projection lines and the global reference frame. Snapshots of the scene can be saved in .tif format, the processed DICOM image can be saved as .dcm, and videos of the kinematics reconstruction can be saved in .avi or .mpg formats.

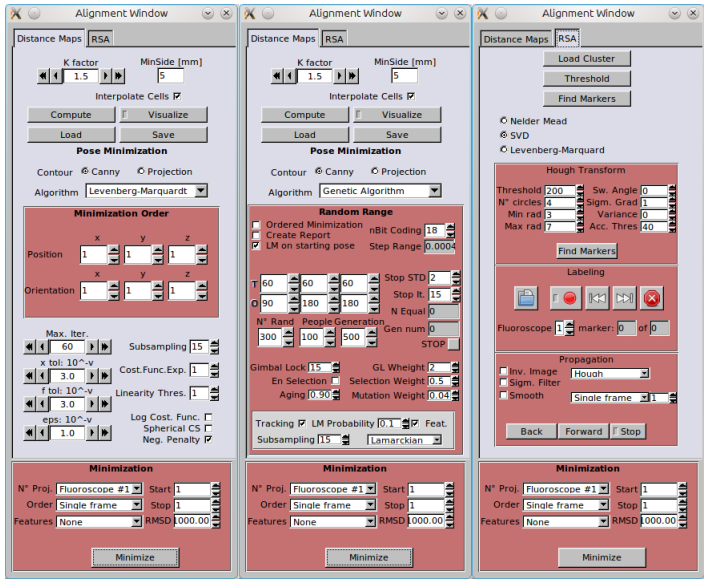

Figure A.4: FluoroTrack: Alignment functionalities.

A.2.4 Alignment

The functionalities for the automatic alignment are gathered in the *Alignment Window* (*Alignment* → *Alignment Window* menu, Figure A.4). Two main kinds

of alignemnt are currently implemented: the model-based 3DF based on Adaptive Distance Map (ADM) and tangency condition, and the marker-based Roentgen Stereo-photogrammetric Analysis (RSA).

The *Minimization* panel, at the bottom of the window, determines the type of alignment to be used:

- **N°Proj**: determines whether to use mono-planar or bi-planar projections
  - *Fluoroscope #1*, mono-planar with the fluoroscope number 1,
  - *Fluoroscope #2*, mono-planar with the fluoroscope number 2,
  - *Both*, for bi-planar alignments.
- **Order**: four options can be chosen:
  - *Single frame*: to optimize the current frame,
  - *Forward*: to propagate the estimated pose of the current frame as the initial guess for the following,
  - *Backward*: to propagate the estimated pose of the current frame as the initial guess for the previous,
  - *No Propagation*: to use the user defined initial guess for every frame

For multi frame alignments the value of *Start* and *Stop* determine the ID of the frames to be analyzed.

Distance Maps

The *Distance Maps* tab is used for the mono- and bi-planar 3DF alignments.

1. **Distance map**: the buttons at the top are used to compute or to load an ADM. The map resolution is specified in *MinSide [mm]* and the *K Factor* determines how bigger the first octant must be with respect to the maximum dimension of the picked mesh.
2. **Pose Minimization**: this box lets the user choose the reference contour to be used for the alignment between the Canny and the projection of the picked mesh (used for validation studies). Three optimization methods are implemented: (*a*) Nelder-Mead, (*b*) Levenberg-Marquardt, and (*c*) Genetic Algorithms. For the first two, the *Minimization Order* group specifies

the Degree Of Freedom (DOF) priority for the alignment (for sequential optimization, see Chapter 3), and the following parameters determine the tolerances to be used as stop criteria. *Subsampling* determines whether to use all the points of the contour or only a subset. A different set of parameters can be set for the Genetic Algorithm such as: the extent of the investigated domain, the number of bit use to code the chromosomes, the population number, stopping criteria, aging and mutation weights, and the type and probability of learning strategies.

Roentgen Stereo-photogrammetric Analysis

The *Load Cluster* button associates to the picked mesh the coordinates of a cluster of landmarks (file .ctr). Two methods can be used to estimate the position of the beads on the images: the Hough Transform, or the Threshold method described for the distortion correction. The tools provided by the *Labeling* box are used to label and propagate backward or forward the association between the 3D coordinates of the beads and their projections in the fluoroscopic images.

A.3 Other Tools

In addition to the described functionalities, FluoroTrack provides also tools to:

- generate Digitally Reconstructed Radiography (DRR),
- to align two 3D datasets using the Iterative Closest Point method (ICP),
- to simulate dataset and to organize deep *in-silico* explorations of the convergence domain of the alignment algorithms,
- to transform the mesh model and associate different local anatomical frames,
- to extract 2D .dcm images from a DICOM series.

These functionalities can be accessed through the toolbar menu.

LIST OF FIGURES

LIST OF TABLES

BIBLIOGRAPHY

[1] P. M. Ludewig and J. E. Reynolds, "The association of scapular kinematics and glenohumeral joint pathologies," *The Journal of Orthopaedic and Sports Physical Therapy*, vol. 39, pp. 90–104, Feb. 2009. PMID: 19194022. 13, 19

[2] S. Tashman, P. Kolowich, D. Collon, K. Anderson, and W. Anderst, "Dynamic function of the ACL-reconstructed knee during running," *Clinical Orthopaedics and Related Research*, vol. 454, pp. 66–73, 2007. PMID: 17091011. 13, 19, 28

[3] S. Zuffi, A. Leardini, F. Catani, S. Fantozzi, and A. Cappello, "A model-based method for the reconstruction of total knee replacement kinematics," *Medical Imaging, IEEE Transactions on*, vol. 18, no. 10, pp. 981–991, 1999. 13, 19, 22, 27, 29, 33, 46, 51, 55, 57, 61, 76, 78, 86, 101, 116

[4] R. Stagni, S. Fantozzi, A. Cappello, and A. Leardini, "Quantification of soft tissue artefact in motion analysis by combining 3D fluoroscopy and stereophotogrammetry: a study on two subjects," *Clinical Biomechanics*, vol. 20, pp. 320–329, Mar. 2005. 13, 14, 19, 21, 49, 60, 137, 138

[5] A. Cappello, R. Stagni, S. Fantozzi, and A. Leardini, "Soft tissue artifact compensation in knee kinematics by double anatomical landmark calibration: performance of a novel method during selected motor tasks," *Biomedical Engineering, IEEE Transactions on*, vol. 52, no. 6, pp. 992–998, 2005. 13, 19, 138

[6] T. S. Curry, J. E. Dowdey, R. C. Murry, and E. E. Christensen, *Christensen's physics of diagnostic radiology*. Lippincott Williams & Wilkins, Aug. 1990. 13

[7] N. Sugano, "Computer-assisted orthopedic surgery," *Journal of Orthopaedic Science*, vol. 8, no. 3, pp. 442–448, 2003. 13

[8] J. T. Cusma, M. R. Bell, M. A. Wondrow, J. P. Taubel, and D. R. Holmes, "Real-time measurement of radiation exposure to patients during diagnostic coronary angiography and percutaneous interventional procedures," *J Am Coll Cardiol*, vol. 33, pp. 427–435, Feb. 1999. 13

[9] K. Perisinakis, N. Theocharopoulos, J. Damilakis, E. Manios, P. Vardas, and N. Gourtsoyiannis, "Fluoroscopically guided implantation of modern cardiac resynchronization de-

vices: Radiation burden to the patient and associated risks," *J Am Coll Cardiol*, vol. 46, pp. 2335–2339, Dec. 2005. 13

[10] G. Selvik, P. Alberius, and A. S. Aronson, "A roentgen stereophotogrammetric system. construction, calibration and technical accuracy," *Acta Radiologica: Diagnosis*, vol. 24, no. 4, pp. 343–352, 1983. PMID: 6637575. 14, 99

[11] S. Lavallee and R. Szeliski, "Recovering the position and orientation of free-form objects from image contours using 3D distance maps," *Pattern Analysis and Machine Intelligence, IEEE Transactions on*, vol. 17, no. 4, pp. 378–390, 1995. 14, 28, 29, 33, 36, 51, 60, 61, 76, 77, 101, 116

[12] S. A. Banks and W. A. Hodge, "Accurate measurement of three-dimensional knee replacement kinematics using single-plane fluoroscopy," *IEEE Transactions on Bio-Medical Engineering*, vol. 43, pp. 638–49, June 1996. PMID: 8987268. 14, 20, 21, 22, 27, 37, 49, 55, 57, 76, 101, 116, 137

[13] M. Mahfouz, W. Hoff, R. Komistek, and D. Dennis, "A robust method for registration of three-dimensional knee implant models to two-dimensional fluoroscopy images," *Medical Imaging, IEEE Transactions on*, vol. 22, no. 12, pp. 1561–1574, 2003. 14, 21, 28, 57, 64, 74, 76, 101, 116

[14] B. L. Kaptein, E. R. Valstar, B. C. Stoel, P. M. Rozing, and J. H. C. Reiber, "A new model-based RSA method validated using CAD models and models from reversed engineering," *Journal of Biomechanics*, vol. 36, pp. 873–882, June 2003. 14, 28, 116

[15] S. Fantozzi, A. Leardini, S. Banks, M. Marcacci, S. Giannini, and F. Catani, "Dynamic in-vivo tibio-femoral and bearing motions in mobile bearing knee arthroplasty," *Knee Surgery, Sports Traumatology, Arthroscopy*, vol. 12, pp. 144–151, Mar. 2004. 14, 21, 49, 55, 74, 100

[16] S. Yamaguchi, K. Gamada, T. Sasho, H. Kato, M. Sonoda, and S. A. Banks, "In vivo kinematics of anterior cruciate ligament deficient knees during pivot and squat activities," *Clinical Biomechanics*, vol. 24, no. 1, pp. 71–76, 2009. 14, 49

[17] B. J. Fregly, H. A. Rahman, and S. A. Banks, "Theoretical accuracy of Model-Based shape matching for measuring natural knee kinematics with Single-Plane fluoroscopy," *Journal of biomechanical engineering*, vol. 127, pp. 692–699, Aug. 2005. PMC1635456. 14, 22, 49, 50, 64, 102

[18] L. Tersi, S. Fantozzi, and R. Stagni, "3D elbow kinematics with mono-planar fluoroscopy: in-silico evaluation," *EURASIP Journal on Advances in Signal Processing*, vol. 2010, 2010. 14, 50, 76, 77, 82, 86

[19] S. Acker, R. Li, H. Murray, P. S. John, S. Banks, S. Mu, U. Wyss, and K. Deluzio, "Accuracy of single-plane fluoroscopy in determining relative position and orientation of total knee replacement components," *Journal of Biomechanics*, vol. In Press, Corrected Proof, 2011. 14, 101, 102

[20] M. Völk, O. W. Hamer, S. Feuerbach, and M. Strotzer, "Dose reduction in skeletal and chest radiography using a large-area flat-panel detector based on amorphous silicon and thallium-doped cesium iodide: technical background, basic image quality parameters, and review of the literature," *European Radiology*, vol. 14, no. 5, pp. 827–834, 2004. 14, 23

[21] S. Hirokawa, M. A. Hossain, Y. Kihara, and S. Ariyoshi, "A 3D kinematic estimation of knee prosthesis using x-ray projection images: clinical assessment of the improved algorithm for fluoroscopy images," *Medical and Biological Engineering and Computing*, vol. 46, pp. 1253–1262, Dec. 2008. 19

[22] D. A. Dennis, M. R. Mahfouz, R. D. Komistek, and W. Hoff, "In vivo determination of normal and anterior cruciate ligament-deficient knee kinematics," *Journal of Biomechanics*, vol. 38, pp. 241–253, Feb. 2005. 19

[23] P. Caravaggi, M. Benedetti, L. Berti, and A. Leardini, "Repeatability of a multi-segment foot protocol in adult subjects," *Gait & Posture*, vol. 33, pp. 133–135, Jan. 2011. 19, 136

[24] J. Stebbins, M. Harrington, N. Thompson, A. Zavatsky, and T. Theologis, "Repeatability of a model for measuring multi-segment foot kinematics in children," *Gait & Posture*, vol. 23, no. 4, pp. 401–410, 2006. 19, 136

[25] Z. Sawacha, G. Cristoferi, G. Guarneri, S. Corazza, G. Dona, P. Denti, A. Facchinetti, A. Avogaro, and C. Cobelli, "Characterizing multisegment foot kinematics during gait in diabetic foot patients," *Journal of NeuroEngineering and Rehabilitation*, vol. 6, no. 1, p. 37, 2009. 19, 136, 139

[26] C. Nester, R. Jones, A. Liu, D. Howard, A. Lundberg, A. Arndt, P. Lundgren, A. Stacoff, and P. Wolf, "Foot kinematics during walking measured using bone and surface mounted markers," *Journal of Biomechanics*, vol. 40, no. 15, pp. 3412–3423, 2007. 19, 20, 136, 137

[27] N. Okita, S. A. Meyers, J. H. Challis, and N. A. Sharkey, "An objective evaluation of a segmented foot model," *Gait & Posture*, vol. 30, no. 1, pp. 27–34, 2009. 19, 20, 136, 137

[28] R. Tranberg and D. Karlsson, "The relative skin movement of the foot: a 2-D roentgen photogrammetry study," *Clinical Biomechanics (Bristol, Avon)*, vol. 13, pp. 71–76, Jan. 1998. PMID: 11415773. 19, 20, 136, 137

[29] J. L. McGinley, R. Baker, R. Wolfe, and M. E. Morris, "The reliability of three-dimensional kinematic gait measurements: A systematic review," *Gait & Posture*, vol. 29, pp. 360–369, Apr. 2009. 19, 136

[30] A. G. Cutti, G. Paolini, M. Troncossi, A. Cappello, and A. Davalli, "Soft tissue artefact assessment in humeral axial rotation," *Gait & Posture*, vol. 21, pp. 341–349, Apr. 2005. 19, 42, 49, 60

[31] H. E. J. Veeger, B. Yu, K. An, and R. H. Rozendal, "Parameters for modeling the upper extremity," *Journal of Biomechanics*, vol. 30, pp. 647–652, June 1997. 20, 49, 60

[32] Y. Ishii, K. Terajima, S. Terashima, and Y. Koga, "Three-dimensional kinematics of the human knee with intracortical pin fixation," *Clinical Orthopaedics and Related Research*, pp. 144–50, Oct. 1997. PMID: 9345219. 20, 137

[33] D. K. Ramsey and P. F. Wretenberg, "Biomechanics of the knee: methodological considerations in the in vivo kinematic analysis of the tibiofemoral and patellofemoral joint," *Clinical Biomechanics*, vol. 14, pp. 595–611, Nov. 1999. 20, 137

[34] J. Kärrholm, R. H. S. Gill, and E. R. Valstar, "The history and future of radiostereometric analysis," *Clinical Orthopaedics and Related Research*, vol. 448, pp. 10–21, 2006. 20, 100

[35] E. R. Valstar, R. Gill, L. Ryd, G. Flivik, N. Börlin, and J. Kärrholm, "Guidelines for standardization of radiostereometry (RSA) of implants," *Acta Orthopaedica*, vol. 76, pp. 563–572, Aug. 2005. PMID: 16195075. 20, 100

[36] T. Saari, L. Carlsson, J. Karlsson, and J. Kärrholm, "Knee kinematics in medial arthrosis. dynamic radiostereometry during active extension and weight-bearing," *Journal of Biomechanics*, vol. 38, pp. 285–292, Feb. 2005. 20, 100, 137

[37] M. A. R. Freeman and V. Pinskerova, "The movement of the normal tibio-femoral joint," *Journal of Biomechanics*, vol. 38, pp. 197–208, Feb. 2005. 20, 137

[38] R. von Eisenhart-Rothe, T. Vogl, K. Englmeier, and H. Graichen, "A new in vivo technique for determination of femoro-tibial and femoro-patellar 3D kinematics in total knee arthroplasty," *Journal of Biomechanics*, vol. 40, no. 14, pp. 3079–3088, 2007. 20

[39] R. von Eisenhart-Rothe, M. Siebert, C. Bringmann, T. Vogl, K. H. Englmeier, and H. Graichen, "A new in vivo technique for determination of 3D kinematics and contact areas of the patello-femoral and tibio-femoral joint," *Journal of Biomechanics*, vol. 37, no. 6, pp. 927–934, 2004. 20, 137

[40] R. D. Komistek, D. A. Dennis, and M. Mahfouz, "In vivo fluoroscopic analysis of the normal human knee," *Clinical Orthopaedics and Related Research*, pp. 69–81, May 2003. PMID: 12771818. 20, 21, 49, 55

[41] L. E. DeFrate, H. Sun, T. J. Gill, H. E. Rubash, and G. Li, "In vivo tibiofemoral contact analysis using 3D MRI-based knee models," *Journal of Biomechanics*, vol. 37, pp. 1499–1504, Oct. 2004. 20

[42] D. C. T. Leondes, *Biomechanical Systems Technology*. 21

[43] J. Stiehl, R. Komistek, D. Dennis, R. Paxson, and W. Hoff, "Fluoroscopic analysis of kinematics after posterior-cruciate-retaining knee arthroplasty," *J Bone Joint Surg Br*, vol. 77-B, pp. 884–889, Nov. 1995. 21, 27, 49, 55, 76

[44] D. A. Dennis, R. D. Komistek, M. R. Mahfouz, B. D. Haas, and J. B. Stiehl, "Multicenter determination of in vivo kinematics after total knee arthroplasty," *Clinical Orthopaedics and Related Research*, pp. 37–57, Nov. 2003. PMID: 14646738. 21, 49, 55, 74

[45] S. A. Banks, G. D. Markovich, and W. A. Hodge, "In vivo kinematics of cruciate-retaining and -substituting knee arthroplasties," *The Journal of Arthroplasty*, vol. 12, pp. 297–304, Apr. 1997. 21, 49, 55, 74

[46] R. D. Komistek, J. B. Stiehl, F. F. Buechel, E. J. Northcut, and M. E. Hajner, "A determination of ankle kinematics using fluoroscopy," *Foot & Ankle International / American Orthopaedic Foot and Ankle Society [and] Swiss Foot and Ankle Society*, vol. 21, pp. 343–50, Apr. 2000. PMID: 10808976. 21, 49, 137

[47] D. A. Dennis, R. D. Komistek, E. J. Northcut, J. A. Ochoa, and A. Ritchie, ""In vivo" determination of hip joint separation and the forces generated due to impact loading conditions," *Journal of Biomechanics*, vol. 34, pp. 623–629, May 2001. 21, 37, 49

[48] R. D. Komistek, D. A. Dennis, J. A. Ochoa, B. D. Haas, and C. Hammill, "In vivo comparison of hip separation after Metal-on-Metal or Metal-on-Polyethylene total hip arthroplasty," *J Bone Joint Surg Am*, vol. 84, pp. 1836–1841, Oct. 2002. 21

[49] R. Stagni, S. Fantozzi, and A. Cappello, "Propagation of anatomical landmark misplacement to knee kinematics: Performance of single and double calibration," *Gait & Posture*, vol. 24, no. 2, pp. 137–141, 2006. 21, 137

[50] R. Stagni, S. Fantozzi, and A. Cappello, "Double calibration vs. global optimisation: Performance and effectiveness for clinical application," *Gait & Posture*, vol. 29, no. 1, pp. 119–122, 2009. 21, 137

[51] W. A. Hoff, R. D. Komistek, D. A. Dennis, S. M. Gabriel, and S. A. Walker, "Three-dimensional determination of femoral-tibial contact positions under in vivo conditions using fluoroscopy," *Clinical Biomechanics*, vol. 13, pp. 455–472, Oct. 1998. 22, 27, 59, 76

[52] D. Tomazevic, B. Likar, T. Slivnik, and F. Pernus, "3-D/2-D registration of CT and MR to x-ray images," *Medical Imaging, IEEE Transactions on*, vol. 22, no. 11, pp. 1407–1416, 2003. 22, 76

[53] D. Russakoff, T. Rohlfing, K. Mori, D. Rueckert, A. Ho, J. Adler, and C. Maurer, "Fast generation of digitally reconstructed radiographs using attenuation fields with application to 2D-3D image registration," *Medical Imaging, IEEE Transactions on*, vol. 24, no. 11, pp. 1441–1454, 2005. 22, 76

[54] P. de Bruin, B. Kaptein, B. Stoel, J. Reiber, P. Rozing, and E. Valstar, "Image-based RSA: roentgen stereophotogrammetric analysis based on 2D-3D image registration," *Journal of Biomechanics*, vol. 41, no. 1, pp. 155–164, 2008. 22, 76

[55] B. You, P. Siy, W. Anderst, and S. Tashman, "In vivo measurement of 3-D skeletal kinematics from sequences of biplane radiographs: Application to knee kinematics," *Medical Imaging, IEEE Transactions on*, vol. 20, no. 6, pp. 514–525, 2001. 22, 76

[56] W. Anderst, R. Zauel, J. Bishop, E. Demps, and S. Tashman, "Validation of three-dimensional model-based tibio-femoral tracking during running," *Medical Engineering & Physics*, vol. 31, no. 1, pp. 10–16, 2009. 22, 76

[57] B. Brown, E. Bolson, M. Frimer, and H. Dodge, "Quantitative coronary arteriography: estimation of dimensions, hemodynamic resistance, and atheroma mass of coronary artery lesions using the arteriogram and digital computation," *Circulation*, vol. 55, pp. 329–337, Feb. 1977. 24

[58] U. Solzabch, H. Wollschlager, A. Zeiher, and H. Just, "Optical distortion due to geomagnetism in quantitative angiography.," *COMPUTERS IN CARDIOLOGY., 1988,*, p. 128, 1988. 24

[59] J. Boone, J. Seibert, W. Barrett, and E. Blood, "Analysis and correction of imperfections in the image intensifier–TV–digitizer imaging chain," *Medical physics*, vol. 18, p. 236, 1991. 24

[60] E. Gronenschild, "The accuracy and reproducibility of a global method to correct for geometric image distortion in the x-ray imaging chain," *Medical Physics*, vol. 24, no. 12, pp. 1875–1888, 1997. 24, 42, 43, 45, 48, 52, 61, 79, 103, 118, 150

[61] S. Fantozzi, A. Cappello, and A. Leardini, "A global method based on thin-plate splines for correction of geometric distortion: An application to fluoroscopic images," *Medical Physics*, vol. 30, pp. 124–131, Feb. 2003. 24, 45, 61, 79

[62] E. Gronenschild, "Correction for geometric image distortion in the x-ray imaging chain: Local technique versus global technique," *Medical Physics*, vol. 26, no. 12, pp. 2602–2616, 1999. 24, 61, 78

[63] J. Chouteau, J. Lerat, R. Testa, B. Moyen, and S. Banks, "Effects of radiograph projection parameter uncertainty on TKA kinematics from model-image registration," *Journal of Biomechanics*, vol. 40, no. 16, pp. 3744–3747, 2007. 24, 52, 61, 78

[64] L. K. Wagner, P. J. Eifel, and R. A. Geise, "Potential biological effects following high x-ray dose interventional procedures," *Journal of Vascular and Interventional Radiology*, vol. 5, pp. 71–84, Jan. 1994. 25

[65] "D.Lgs. 230/95." http://www.aimn.it/lex/Lex_230.html. 25

[66] R. Fazel, H. M. Krumholz, Y. Wang, J. S. Ross, J. Chen, H. H. Ting, N. D. Shah, K. Nasir, A. J. Einstein, and B. K. Nallamothu, "Exposure to low-dose ionizing radiation from medical imaging procedures," *The New England Journal of Medicine*, vol. 361, pp. 849–857, Aug. 2009. PMID: 19710483. 25

[67] T. P. Wallace and P. A. Wintz, "An efficient three-dimensional aircraft recognition algorithm using normalized fourier descriptors," *Computer Graphics and Image Processing*, vol. 13, no. 2, pp. 99–126, 1980. 27

[68] S. Tashman and W. Anderst, "In-Vivo measurement of dynamic joint motion using high speed biplane radiography and CT: application to canine ACL deficiency," *Journal of Biomechanical Engineering*, vol. 125, pp. 238–245, Apr. 2003. 28, 37

[69] J. Bingham and G. Li, "An optimized image matching method for determining In-Vivo TKA kinematics with a Dual-Orthogonal fluoroscopic imaging system," *Journal of Biomechanical Engineering*, vol. 128, no. 4, pp. 588–595, 2006. 28, 37

[70] J. Canny, "A computational approach to edge detection," *Pattern Analysis and Machine Intelligence, IEEE Transactions on*, vol. PAMI-8, no. 6, pp. 679–698, 1986. 30, 45, 52, 116

[71] M. Yau and S. N. Srihari, "A hierarchical data structure for multidimensional digital images," *Commun. ACM*, vol. 26, no. 7, pp. 504–515, 1983. 31

[72] B. L. Kaptein, E. R. Valstar, B. C. Stoel, P. M. Rozing, and J. H. C. Reiber, "A new type of model-based roentgen stereophotogrammetric analysis for solving the occluded marker problem," *Journal of Biomechanics*, vol. 38, pp. 2330–2334, Nov. 2005. PMID: 16154422. 37, 101, 124

[73] D. W. Marquardt, "An algorithm for Least-Squares estimation of nonlinear parameters," *Journal of the Society for Industrial and Applied Mathematics*, vol. 11, pp. 431–441, June 1963. ArticleType: primary_article / Full publication date: Jun., 1963 / Copyright ©1963 Society for Industrial and Applied Mathematics. 37, 46, 51, 61, 76

[74] M. J. Bey, S. K. Kline, R. Zauel, P. A. Kolowich, and T. R. Lock, "In vivo measurement of glenohumeral joint contact patterns," 2010. 42, 116

[75] N. Nishinaka, H. Tsutsui, K. Mihara, K. Suzuki, D. Makiuchi, Y. Kon, T. W. Wright, M. W. Moser, K. Gamada, H. Sugimoto, and S. A. Banks, "Determination of in vivo glenohumeral translation using fluoroscopy and shape-matching techniques," *Journal of Shoulder and Elbow Surgery*, vol. 17, no. 2, pp. 319–322, 2008. 42, 49, 55

[76] R. Schmidt, C. Disselhorst-Klug, J. Silny, and G. Rau, "A marker-based measurement procedure for unconstrained wrist and elbow motions," *Journal of Biomechanics*, vol. 32, pp. 615–621, June 1999. 42, 49, 60

[77] "Virtual animation of the kinematics of the human for industrial, educational and research purposes." http://www.ulb.ac.be/project/vakhum/index.html. 44, 52, 62, 83

[78] G. Wu, F. C. van der Helm, H. D. Veeger, M. Makhsous, P. V. Roy, C. Anglin, J. Nagels, A. R. Karduna, K. McQuade, X. Wang, F. W. Werner, and B. Buchholz, "ISB recommendation on definitions of joint coordinate systems of various joints for the reporting of human joint motion–Part II: shoulder, elbow, wrist and hand," *Journal of Biomechanics*, vol. 38, pp. 981–992, May 2005. 44, 50, 52, 62, 83

[79] J. C. Lagarias, J. A. Reeds, M. H. Wright, and P. E. Wright, "Convergence properties of the Nelder-Mead simplex algorithm in low dimensions," *SIAM JOURNAL OF OPTIMIZATION*, vol. 9, pp. 112–147, 1996. 45

[80] A. Goto, H. Moritomo, T. Murase, K. Oka, K. Sugamoto, T. Arimura, Y. Nakajima, T. Yamazaki, Y. Sato, S. Tamura, H. Yoshikawa, and T. Ochi, "In vivo elbow biomechanical analysis during flexion: three-dimensional motion analysis using magnetic resonance imaging," *Journal of Shoulder and Elbow Surgery*, vol. 13, no. 4, pp. 441–447, 2004. 49, 60

[81] B. V. Duren, H. Pandit, D. Beard, D. Murray, and H. Gill, "Accuracy evaluation of fluoroscopy-based 2D and 3D pose reconstruction with unicompartmental knee arthroplasty," *Medical Engineering & Physics*, vol. 31, pp. 356–363, Apr. 2009. 49

[82] E. Fu, G. Li, J. S. Souer, S. Lozano-Calderon, J. H. Herndon, J. B. Jupiter, and N. C. Chen, "Elbow position affects distal radioulnar joint kinematics," *The Journal of Hand Surgery*, vol. 34, no. 7, pp. 1261–1268, 2009. 50, 56

[83] G. Li, S. K. V. de Velde, and J. T. Bingham, "Validation of a non-invasive fluoroscopic imaging technique for the measurement of dynamic knee joint motion," *Journal of Biomechanics*, vol. 41, no. 7, pp. 1616–1622, 2008. 50

[84] T. aki Moro-oka, S. Hamai, H. Miura, T. Shimoto, H. Higaki, B. J. Fregly, Y. Iwamoto, and S. A. Banks, "Can magnetic resonance imaging-derived bone models be used for accurate motion measurement with single-plane three-dimensional shape registration?," *Journal of Orthopaedic Research*, vol. 25, no. 7, pp. 867–872, 2007. 50

[85] M. R. Mahfouz, W. A. Hoff, R. D. Komistek, and D. A. Dennis, "Effect of segmentation errors on 3D-to-2D registration of implant models in x-ray images," *Journal of Biomechanics*, vol. 38, pp. 229–239, Feb. 2005. 50

[86] L. Tersi, R. Stagni, S. Fantozzi, and A. Cappello, "3D joints kinematics with fluoroscopy: algorithm optimization," in *Proceedings ICCB 2009*, (s.l), p. 1, s.n, 2009. 50, 51

[87] E. S. Grood and W. J. Suntay, "A joint coordinate system for the clinical description of three-dimensional motions: application to the knee," *Journal of Biomechanical Engineering*, vol. 105, pp. 136–44, May 1983. PMID: 6865355. 53

[88] C. R. Bragdon, H. Malchau, X. Yuan, R. Perinchief, J. Kärrholm, N. Börlin, D. M. Estok, and W. H. Harris, "Experimental assessment of precision and accuracy of radiostereometric analysis for the determination of polyethylene wear in a total hip replacement model," *Journal of Orthopaedic Research*, vol. 20, no. 4, pp. 688–695, 2002. 56, 100

[89] I. Önsten, A. Berzins, S. Shott, and D. R. Sumner, "Accuracy and precision of radiostereometric analysis in the measurement of THR femoral component translations: human and canine in vitro models," *Journal of Orthopaedic Research*, vol. 19, no. 6, pp. 1162–1167, 2001. 56, 100

[90] J. Ioppolo, N. Börlin, C. Bragdon, M. Li, R. Price, D. Wood, H. Malchau, and B. Nivbrant, "Validation of a low-dose hybrid RSA and fluoroscopy technique: Determination of accuracy, bias and precision," *Journal of Biomechanics*, vol. 40, no. 3, pp. 686–692, 2007. 56

[91] A. Ericson, A. Arndt, A. Stark, P. Wretenberg, and A. Lundberg, "Variation in the position and orientation of the elbow flexion axis," *J Bone Joint Surg Br*, vol. 85-B, pp. 538–544, May 2003. 60

[92] D. Eygendaal, E. R. Valstar, J. O. Sjöbjerg, and P. M. Rozing, "Biomechanical evaluation of the elbow using roentgen stereophotogrammetric analysis," 2002. 60

[93] F. Schuind, S. O'Driscoll, S. Korinek, K. An, and B. Morrey, "Loose-hinge total elbow arthroplasty: An experimental study of the effects of implant alignment on three-dimensional elbow kinematics," *The Journal of Arthroplasty*, vol. 10, pp. 670–678, Oct. 1995. 60

[94] "VXL - c++ libraries for computer vision." http://vxl.sourceforge.net/. 61, 82

[95] R. H. Gong, P. Abolmaesumi, and J. Stewart, "A robust technique for 2D-3D registration," in *Engineering in Medicine and Biology Society, 2006. EMBS '06. 28th Annual International Conference of the IEEE*, pp. 1433–1436, 2006. 74

[96] T. Lu, T. Tsai, M. Kuo, H. Hsu, and H. Chen, "In vivo three-dimensional kinematics of the normal knee during active extension under unloaded and loaded conditions using single-plane fluoroscopy," *Medical Engineering & Physics*, vol. 30, pp. 1004–1012, Oct. 2008. 76

[97] J. M. Scarvell, M. R. Pickering, and P. N. Smith, "New registration algorithm for determining 3D knee kinematics using CT and single-plane fluoroscopy with improved out-of-plane translation accuracy," *Journal of Orthopaedic Research*, pp. n/a–n/a, 2009. 76

[98] A. Prins, B. Kaptein, B. Stoel, J. Reiber, and E. Valstar, "Detecting femur-insert collisions to improve precision of fluoroscopic knee arthroplasty analysis," *Journal of Biomechanics*, vol. 43, pp. 694–700, Mar. 2010. 76

[99] T. Yamazaki, T. Watanabe, Y. Nakajima, K. Sugamoto, T. Tomita, H. Yoshikawa, and S. Tamura, "Improvement of depth position in 2-D/3-D registration of knee implants using single-plane fluoroscopy," *Medical Imaging, IEEE Transactions on*, vol. 23, no. 5, pp. 602–612, 2004. 76, 101

[100] T. Tsai, T. Lu, C. Chen, M. Kuo, and H. Hsu, "A volumetric model-based 2D to 3D registration method for measuring kinematics of natural knees with single-plane fluoroscopy," *Medical Physics*, vol. 37, pp. 1273–1284, Mar. 2010. 76

[101] J. S. Arora, M. W. Huang, and C. C. Hsieh, "Methods for optimization of nonlinear problems with discrete variables: A review," *Structural Optimization*, vol. 8, no. 2-3, pp. 69–85, 1994. 76

[102] J. H. Holland, *Adaptation in Natural and Artificial Systems: An Introductory Analysis with Applications to Biology, Control, and Artificial Intelligence*. The MIT Press, Apr. 1992. 76, 77

[103] T. A. El-mihoub, A. A. Hopgood, L. Nolle, and A. Battersby, "Hybrid genetic algorithms: A review," Dec. 2009. 77, 79

[104] P. Moscato, "On evolution, search, optimization, genetic algorithms and martial arts: Towards memetic algorithms," *Caltech Concurrent Computation Program, C3P Report*, vol. 826, p. 1989, 1989. 77

[105] C. R. Houck, J. A. Joines, M. G. Kay, and J. R. Wilson, "Empirical investigation of the benefits of partial lamarckianism," *Evolutionary Computation*, vol. 5, no. 1, pp. 31–60, 1997. PMID: 10021752. 79, 82

[106] A. Wright, "Genetic algorithms for real parameter optimization," *Foundations of genetic algorithms*, vol. 1, pp. 205–218, 1991. 79, 106

[107] R. L. Iman, J. M. Davenport, and D. K. Zeigler, *Latin hypercube sampling (program user's guide). [LHC, in FORTRAN]*. 1980. 85

[108] G. Selvik, "Roentgen stereophotogrammetry," *Acta Orthopaedica*, vol. 60, no. s232, pp. 1–51, 1989. 100

[109] N. Börlin, T. Thien, and J. Kärrholm, "The precision of radiostereometric measurements. manual vs. digital measurements," *Journal of Biomechanics*, vol. 35, pp. 69–79, Jan. 2002. 100

[110] K. Halldin, B. Zoëga, P. Nyberg, J. Kärrholm, and B. I. Lind, "The effect of standard lumbar discectomy on segmental motion: 5-year follow-up using radiostereometry," *International Orthopaedics*, vol. 29, pp. 83–87, Apr. 2005. PMID: 15739065. 100

[111] J. Kärrholm, L. I. Hansson, and G. Selvik, "Longitudinal growth rate of the distal tibia and fibula in children," *Clinical Orthopaedics and Related Research*, pp. 121–128, Dec. 1984. PMID: 6499303. 100

[112] P. Edixhoven, R. Huiskes, R. de Graaf, T. J. van Rens, and T. J. Slooff, "Accuracy and reproducibility of instrumented knee-drawer tests," *Journal of Orthopaedic Research: Official Publication of the Orthopaedic Research Society*, vol. 5, no. 3, pp. 378–387, 1987. PMID: 3625361. 100

[113] B. C. Fleming, G. D. Peura, J. A. Abate, and B. D. Beynnon, "Accuracy and repeatability of roentgen stereophotogrammetric analysis (RSA) for measuring knee laxity in longitudinal studies," *Journal of Biomechanics*, vol. 34, pp. 1355–1359, Oct. 2001. PMID: 11522316. 100

[114] G. Digas, J. Kärrholm, J. Thanner, H. Malchau, and P. Herberts, "Highly cross-linked polyethylene in cemented THA: randomized study of 61 hips," *Clinical Orthopaedics and Related Research*, pp. 126–138, Dec. 2003. PMID: 14646710. 100

[115] J. Kiss, D. W. Murray, A. R. Turner-Smith, and C. J. Bulstrode, "Roentgen stereophotogrammetric analysis for assessing migration of total hip replacement femoral components," *Proceedings of the Institution of Mechanical Engineers. Part H, Journal of Engineering in Medicine*, vol. 209, no. 3, pp. 169–175, 1995. PMID: 8519406. 100

[116] R. van Dijk, R. Huiskes, and G. Selvik, "Roentgen stereophotogrammetric methods for the evaluation of the three dimensional kinematic behaviour and cruciate ligament length patterns of the human knee joint," *Journal of Biomechanics*, vol. 12, no. 9, pp. 727–731, 1979. PMID: 489639. 100

[117] S. Brandsson, J. Karlsson, L. Swärd, J. Kartus, B. I. Eriksson, and J. Kärrholm, "Kinematics and laxity of the knee joint after anterior cruciate ligament reconstruction," *The American Journal of Sports Medicine*, vol. 30, pp. 361 –367, May 2002. 100

[118] H. Woltring, R. Huiskes, A. de Lange, and F. Veldpaus, "Finite centroid and helical axis estimation from noisy landmark measurements in the study of human joint kinematics," *Journal of Biomechanics*, vol. 18, no. 5, pp. 379–389, 1985. 101

[119] A. de Lange, R. Huiskes, and J. Kauer, "Measurement errors in roentgen-stereophotogrammetric joint-motion analysis," *Journal of Biomechanics*, vol. 23, no. 3, pp. 259–269, 1990. 101

[120] S. Acker, "High flexion kinematics and kinetics for the improvement of artificial knee joints," *Ph. D. Thesis*, 2010. 101

[121] "Sawbones." http://www.sawbones.com/. 103

[122] A. E. Kedgley and T. R. Jenkyn, "RSA calibration accuracy of a fluoroscopy-based system using nonorthogonal images for measuring functional kinematics," *Medical Physics*, vol. 36, no. 7, p. 3176, 2009. 103, 112

[123] G. Wu, S. Siegler, P. Allard, C. Kirtley, A. Leardini, D. Rosenbaum, M. Whittle, D. D. D'Lima, L. Cristofolini, H. Witte, O. Schmid, and I. Stokes, "ISB recommendation on definitions of joint coordinate system of various joints for the reporting of human joint motion–part i: ankle, hip, and spine," *Journal of Biomechanics*, vol. 35, pp. 543–548, Apr. 2002. 103

[124] G. Conti, L. Cristofolini, M. Juszczyk, A. Leardini, and M. Viceconti, "Comparison of three standard anatomical reference frames for the tibia-fibula complex," *Journal of Biomechanics*, vol. 41, pp. 3384–3389, Dec. 2008. 103

[125] J. Sethian, *Level Set Methods and Fast Marching Methods*. Cambridge University Press, 1999. 106, 119, 121

[126] J. Illingworth and J. Kittler, "A survey of the hough transform," *Computer Vision, Graphics, and Image Processing*, vol. 44, pp. 87–116, Oct. 1988. 106

[127] E. R. Valstar, R. G. H. H. Nelissen, J. H. C. Reiber, and P. M. Rozing, "The use of roentgen stereophotogrammetry to study micromotion of orthopaedic implants," *ISPRS Journal of Photogrammetry and Remote Sensing*, vol. 56, no. 5-6, pp. 376–389, 2002. 106

[128] R. J. Hanson and M. J. Norris, "Analysis of measurements based on the singular value decomposition," *SIAM Journal on Scientific and Statistical Computing*, vol. 2, no. 3, p. 363, 1981. 107

[129] I. Söderkvist and P. Wedin, "Determining the movements of the skeleton using well-configured markers," *Journal of Biomechanics*, vol. 26, pp. 1473–1477, Dec. 1993. 107

[130] K. S. Arun, T. S. Huang, and S. D. Blostein, "Least-Squares fitting of two 3-D point sets," *Pattern Analysis and Machine Intelligence, IEEE Transactions on*, vol. PAMI-9, no. 5, pp. 698–700, 1987. 108

[131] J. M. Bland and D. G. Altman, "Statistical methods for assessing agreement between two methods of clinical measurement," *International Journal of Nursing Studies*, vol. 47, pp. 931–936, Aug. 2010. 108, 124

[132] J. M. Bland and D. G. Altman, "Measuring agreement in method comparison studies," *Statistical Methods in Medical Research*, vol. 8, pp. 135 –160, Apr. 1999. 108, 124

[133] C. Hurschler, F. Seehaus, J. Emmerich, B. L. Kaptein, and H. Windhagen, "Comparison of the Model-Based and Marker-Based roentgen stereophotogrammetry methods in a typical clinical setting," *The Journal of Arthroplasty*, vol. 24, pp. 594–606, June 2009. 116

[134] A. Oprea and C. Vertan, "A quantitative evaluation of the hip prosthesis segmentation quality in X-Ray images," in *Signals, Circuits and Systems, 2007. ISSCS 2007. International Symposium on*, vol. 1, pp. 1–4, 2007. 116

[135] C. Domokos and Z. Kato, "Parametric estimation of affine deformations of planar shapes," *Pattern Recognition*, vol. 43, pp. 569–578, Mar. 2010. 117, 132

[136] K. Varshney, N. Paragios, J. Deux, A. Kulski, R. Raymond, P. Hernigou, and A. Rahmouni, "Postarthroplasty examination using X-Ray images," *Medical Imaging, IEEE Transactions on*, vol. 28, no. 3, pp. 469–474, 2009. 117

[137] G. Sapiro, *Geometric partial differential equations and image analysis*. Cambridge University Press, 2001. 118

[138] W. K. Pratt, *Digital Image Processing*. Hoboken, NJ, USA: John Wiley & Sons, Inc., 2007. 119, 120

[139] C. Chan, A. Katsaggelos, and A. Sahakian, "Image sequence filtering in quantum-limited noise with applications to low-dose fluoroscopy," *Medical Imaging, IEEE Transactions on*, vol. 12, no. 3, pp. 610–621, 1993. 119, 122

[140] D. Zhao, S. A. Banks, D. D. D'Lima, C. W. Colwell, and B. J. Fregly, "In vivo medial and lateral tibial loads during dynamic and high flexion activities," *Journal of Orthopaedic Research: Official Publication of the Orthopaedic Research Society*, vol. 25, pp. 593–602, May 2007. PMID: 17290383. 121

[141] R. T. Rockafellar and R. J. Wets, *Variational analysis*. Springer, 2004. 122

[142] P. Ghosh, M. Sargin, and B. Manjunath, "Robust dynamical model for simultaneous registration and segmentation in a variational framework: A bayesian approach," in *Computer Vision, 2009 IEEE 12th International Conference on*, pp. 709–716, 2009. 123

[143] R. B. Davis, S. Õunpuu, D. Tyburski, and J. R. Gage, "A gait analysis data collection and reduction technique," *Human Movement Science*, vol. 10, pp. 575–587, Oct. 1991. 136

[144] M. P. Kadaba, H. K. Ramakrishnan, M. E. Wootten, J. Gainey, G. Gorton, and G. V. B. Cochran, "Repeatability of kinematic, kinetic, and electromyographic data in normal adult gait," *Journal of Orthopaedic Research*, vol. 7, no. 6, pp. 849–860, 1989. 136

[145] M. P. Kadaba, H. K. Ramakrishnan, and M. E. Wootten, "Measurement of lower extremity kinematics during level walking," *Journal of Orthopaedic Research: Official Publication of the Orthopaedic Research Society*, vol. 8, pp. 383–392, May 1990. PMID: 2324857. 136

[146] A. Cappozzo, F. Catani, U. D. Croce, and A. Leardini, "Position and orientation in space of bones during movement: anatomical frame definition and determination," *Clinical Biomechanics*, vol. 10, no. 4, pp. 171–178, 1995. 136

[147] L. Rankine, J. Long, K. Canseco, and G. F. Harris, "Multisegmental foot modeling: a review," *Critical Reviews in Biomedical Engineering*, vol. 36, no. 2-3, pp. 127–181, 2008. PMID: 19740070. 136

[148] D. E. Turner, P. S. Helliwell, K. L. Siegel, and J. Woodburn, "Biomechanics of the foot in rheumatoid arthritis: identifying abnormal function and the factors associated with localised disease 'impact'," *Clinical Biomechanics (Bristol, Avon)*, vol. 23, pp. 93–100, Jan. 2008. PMID: 17904711. 136

[149] K. Canseco, J. Long, R. Marks, M. Khazzam, and G. Harris, "Quantitative characterization of gait kinematics in patients with hallux rigidus using the milwaukee foot model," *Journal of Orthopaedic Research*, vol. 26, no. 4, pp. 419–427, 2008. 136

[150] R. M. Marks, J. T. Long, M. E. Ness, M. Khazzam, and G. F. Harris, "Surgical reconstruction of posterior tibial tendon dysfunction: prospective comparison of flexor digitorum longus substitution combined with lateral column lengthening or medial displacement calcaneal osteotomy," *Gait & Posture*, vol. 29, pp. 17–22, Jan. 2009. PMID: 18603429. 136

[151] J. Simon, L. Doederlein, A. S. McIntosh, D. Metaxiotis, H. G. Bock, and S. I. Wolf, "The heidelberg foot measurement method: development, description and assessment," *Gait & Posture*, vol. 23, pp. 411–424, June 2006. PMID: 16157483. 136

[152] K. M. Brown, D. E. Bursey, L. J. Arneson, C. A. Andrews, P. M. Ludewig, and W. M. Glasoe, "Consideration of digitization precision when building local coordinate axes for a foot model," *Journal of Biomechanics*, vol. 42, pp. 1263–1269, June 2009. PMID: 19375706. 136

[153] E. Garling, B. Kaptein, B. Mertens, W. Barendregt, H. Veeger, R. Nelissen, and E. Valstar, "Soft-tissue artefact assessment during step-up using fluoroscopy and skin-mounted markers," *Journal of Biomechanics*, vol. 40, no. Supplement 1, pp. S18–S24, 2007. 137

[154] M. Akbarshahi, A. G. Schache, J. W. Fernandez, R. Baker, S. Banks, and M. G. Pandy, "Non-invasive assessment of soft-tissue artifact and its effect on knee joint kinematics during functional activity," *Journal of Biomechanics*, vol. 43, pp. 1292–1301, May 2010. PMID: 20206357. 137

[155] C. Ridola and A. Palma, "Functional anatomy and imaging of the foot," *Italian Journal of Anatomy and Embryology = Archivio Italiano Di Anatomia Ed Embriologia*, vol. 106, pp. 85–98, June 2001. PMID: 11504250. 138

[156] G. S. Lewis, T. L. Cohen, A. R. Seisler, K. A. Kirby, F. T. Sheehan, and S. J. Piazza, "In vivo tests of an improved method for functional location of the subtalar joint axis," *Journal of Biomechanics*, vol. 42, pp. 146–151, Jan. 2009. PMID: 19010472. 138

[157] R. Stagni, A. Leardini, J. J. O'Connor, and S. Giannini, "Role of passive structures in the mobility and stability of the human subtalar joint: a literature review," *Foot & Ankle International / American Orthopaedic Foot and Ankle Society [and] Swiss Foot and Ankle Society*, vol. 24, pp. 402–409, May 2003. PMID: 12801196. 138

[158] "3D images to RP, CAD, FE and CFD models with simpleware software." http://www.simpleware.com/. 140

[159] "Fast light toolkit (FLTK)." http://www.fltk.org/. 148

[160] "ITK - segmentation & registration toolkit." http://www.itk.org/. 148

[161] "VTK - the visualization toolkit." http://www.vtk.org/. 148

SCIENTIFIC WRITING

Journal articles

1. **L. Tersi**, S. Fantozzi, R. Stagni: 3D elbow kinematics with mono-planar fluoroscopy: in-silico evaluation: *EURASIP Journal on Advances in Signal Processing*. 2010. (10.1155/2010/142989).
2. **L. Tersi**, S. Fantozzi, R. Stagni, A. Cappello: In-vivo elbow kinematics using fluoroscopy: a feasibility study: Under review to *Computer Methods and Programs in Biomedicine*.
3. **L. Tersi**, S. Fantozzi, R. Stagni: A Memetic Algorithm for Joint Kinematic Estimation with 3D Fluoroscopy, submitted to *IEEE Transaction on Biomedical Engineering*.
4. G. Tarroni, **L. Tersi**, C. Corsi, R. Stagni: A Fast and Automated Method for the Segmentation of Prosthetic Components in 3D Fluoroscopy, to be submitted to *IEEE Transaction on Biomedical Engineering*.
5. **L. Tersi**, A. Barré, S. Fantozzi, R. Stagni,: *In-vitro* validation of monoplanar 3D fluoroscopy with RSA, submitted to *Journal of Biomechanics*.

Conference Papers

1. **L. Tersi**, R. Stagni, P. Masini, S. Fantozzi, A. Cappello: 3D fluoroscopy to analyse elbow kinematics. Proceeding of *ESBME 2008*, Crete.
2. **L. Tersi**, S. Fantozzi, R. Stagni, P. Masini, A. Cocchi, A.G. Cutti: Feasability study for the quantification of in-vivo elbow kinematics using 3D fluoroscopy. Proceeding of *GNB 2008*, Pisa.

3. **L. Tersi**, S. Fantozzi, R.Stagni, P. Masini,A. Cocchi, A.G. Cutti: In-vivo elbow kinematics using fluoroscopy: a feasability study. Proceeding of *ISG 2008*, Bologna.

4. **L. Tersi**, R. Stagni, S. Fantozzi, A. Cappello: 3D Joints kinematics with fluoroscopy: algorithm optimization. In: Proceedings *ICCB 2009*. Bertinoro (FC), 16-18 Settembre 2009, s.l: s.n, p. 1.

5. A. Ferrari, **L. Tersi**, M. Heijboer, M. Raggi, A.G. Cutti: Portable system for gait analysis of children with cerebral palsy. In: *2nd Summer School - Advanced technologies for neuro-motor assessment and rehabilitation*. Monte San Pietro, Bologna - Italy, 13-19/07/2008, p. 74-75, ISBN/ISSN: 88-900847-7-4.

6. P. Garofalo, S. Fantozzi, A.G. Cutti, **L. Tersi**, A. Ferrari, M. Raggi, R. Stagni, A. Cappello, A. Davalli:. Development of motion analysis protocols based on inertial sensors and fluoroscopy. In: *3D Analysis of Human Movement. Fusion Works!*. Santpoort/Amsterdam, The Netherlands, 28-31 Ottobre,2008, s.l: s.n.

7. Z. Sawacha, A. Guiotto, S. Fantozzi, R. Stagni, C. Fassina, **L. Tersi**, C. Cobelli: Advantages of multiple calibration in multisegment foot 3D kinematics. In: Proceedings *GCMAS 2010*, Miami, Florida USA. May 12-15 2010.

8. **L. Tersi**, R. Stagni, S. Fantozzi, A. Cappello: Total Knee Replacement kinematics: an in-silico reliability comparison between mono-planar and bi-planar 3D Fluoroscopy. In: Proceedings *XVII ESB Conference 2010*. Edinburgh, Scotland UK, 5-8 July 2010.

9. **L. Tersi**, R. Stagni, S. Fantozzi, A. Cappello: Genetic Algorithm as a robust method for the joint kinematics estimation with mono-planar 3D fluoroscopy. In: Proceedings *XVII ESB Conference 2010*. Edinburgh, Scotland UK, 5-8 July 2010.

10. A. Guiotto, Z.S. Sawacha, C. Fassina, **L. Tersi**, S. Fantozzi, R. Stagni, C. Cobelli: Use of multiple calibration in multisegment foot 3D kinematics. In: proceedings *GNB 2010*, Torino, 8-10 July 2010.

11. **L. Tersi**, G. Tarroni, C. Corsi, R. Stagni: Automatic prosthesis segmentation in 3D fluoroscopy. In: proceedings *International Computer Vision Summer School, ICVSS 2010*, Sicily, Italy, July 12-18, 2010

12. Z.S. Sawacha, A. Guiotto, C. Fassina, S. Fantozzi, R. Stagni, **L. Tersi**, C. Cobelli. Use of multiple calibration in multisegment 3D foot kinematics: In: proceedings *i-FAB 2010*, Seattle, September 16-18, 2010.

13. R. Stagni, **L.Tersi**, S. Fantozzi, Z. Sawacha, A. Guiotto, C. Cobelli: In-vivo foot kinematics: definition of a fluoroscopic gold standard for the evaluation of marker-based protocols. In: proceedings *i-Fab 2010*, Seattle, September 16-18, 2010.

14. **L.Tersi**, R. Stagni, S. Fantozzi, A. Cappello: Mono-planar vs Bi-planar 3D Fluoroscopy: in-silico Simulation of the Estimation of Total Knee Replacement kinematics. In: Proceedings *VPH 2010*, Brussels, Belgium, September 30 - October 1, 2010

15. **L. Tersi**, A. Barré, S. Fantozzi, K. Aminian, R. Stagni: Quantification of the performance of mono- and bi-planar 3D fluoroscopy compared to marker-based RSA. Submitted to *XXIII congress of ISB 2011*, Brussels, Belgium, July 3-7, 2011.

16. R. Stagni, **L. Tersi**, S. Fantozzi, Z. Sawacha, A. Guiotto, C. Cobelli: Definition of a fluoroscopic gold standard for the evaluation of marker-based protocols. Submitted to *XXIII congress of ISB 2011*, Brussels, Belgium, July 3-7, 2011.

17. R. Stagni, **L. Tersi**, S. Fantozzi, Z. Sawacha, A. Guiotto, C. Cobelli: In-vivo foot kinematics: definition of a fluoroscopic gold standard for the evaluation of marker-based protocols. Submitted to *2011 Gait and Clinical Movement Analysis Society - GCMAS*, Bethesda, MD, USA April 26-29, 2011.

Awards

1. ESB Travel Award Winner at XVII ESB Conference for the poster *Total Knee Replacement kinematics: an in-silico reliability comparison between mono-planar and bi-planar 3D Fluoroscopy.* **L. Tersi**, R. Stagni, S. Fantozzi, A. Cappello.